University of California
Los Angeles

The Evolution and Life Cycle of Valley Cold Pools

A dissertation submitted in partial satisfaction
of the requirements for the degree
Doctor of Philosophy in Atmospheric and Oceanic Sciences

by

Travis Harold Wilson

2015

Abstract of the Dissertation

The Evolution and Life Cycle of Valley Cold Pools

by

Travis Harold Wilson

Doctor of Philosophy in Atmospheric and Oceanic Sciences

University of California, Los Angeles, 2015

Professor Robert G. Fovell, Chair

Despite our increased understanding in the relevant physical processes, forecasting radiative cold pools and their associated meteorological phenomena (e.g. fog and freezing rain) remains a challenging problem in mesoscale models. In this thesis we recognize that our current modeling approach is flawed and incomplete, rendering us unable to forecast these high impact events. Using the Weather Research and Forecasting (WRF) model, fundamental deficiencies are exploited and new physical parameterizations are introduced to address these issues without degrading the model in other areas and time.

It was found that the default model diffusion, which is calculated on model sigma coordinates, in addition to the 6th order numerical filter, prevented the formation of cold pools. Furthermore, soil moisture in and around valleys from both natural and anthropogenic sources, the vertical resolution, and model physics were all found to be important and play at least some role in forecasting these events. Finally, key physical processes governing the evolution and life cycle of cold pools were missing and subsequently introduced to a boundary layer parameterization to substantially improve its forecasting ability. Through the knowledge presented here, this and other key modifications have accomplished a numerical weather model of more general use and applicability which will not only be of use to the modeling community but society at large.

The dissertation of Travis Harold Wilson is approved.

Kuo-Nan Liou

William Newman

Yongkang Xue

Robert G. Fovell, Committee Chair

University of California, Los Angeles

2015

Table of Contents

List of Figures

List of Tables

Vita

2008	A.A., General Education, Shasta Community College, Redding, CA.
2009–2011	Student Career Experience Program (SCEP), National Weather Service, Anchorage, AK.
2010	B.S., Atmospheric and Oceanic Sciences, University of California Los Angeles, Los Angeles, CA.
2010-2012	Teaching Associate, Department of Atmospheric and Oceanic Sciences, University of California Los Angeles, Los Angeles, CA. Received Morris Neiburger Award.
2012	M.S., Atmospheric and Oceanic Sciences, University of California Los Angeles, Los Angeles, CA.
2012-2013	Visitor, National Center for Atmospheric Research (NCAR) – National Oceanic Atmospheric Administration (NOAA) Developmental Testbed Center, Boulder, CO.
2013-2015	Graduate Student Researcher, Department of Atmospheric and Oceanic Sciences, University of California Los Angeles, Los Angeles, CA.

CHAPTER 1

Introduction

It was 1901, weather forecasting was a crude process and "quite elementary in character" (Abbe, 1901). There were very few observations, theoretical physics was almost entirely absent from forecasting, and the next days weather was grossly extrapolated from current conditions (Lynch, 2008). Predictions largely relied on local climatology, experience, and hand drawn maps that connected points of equal pressure, or isobars, to reveal atmospheric disturbances. Using this method, higher pressures were associated with fair weather while the opposite was indicative of a storm. By using the prevailing westerly flow in the mid latitudes, forecasters looked upstream for an approaching disturbance; however, using simple extrapolation is fundamentally flawed since advection is highly nonlinear.

A few years later, Bjerknes (1904) realized that if every atmospheric state develops from the preceding one, two things were required for weather forecasting: An accurate knowledge of the initial state and an adequate understanding of the laws which govern the flow. Bjerknes noted the lack of observing surface stations in foreign countries in addition to those missing over the oceans and upper atmosphere. He understood that these missing observations would have an "overwhelming influence" on weather forecasts and if obtained, would put forecasting on a rational basis. He hoped that, "either as a daily routine, or for certain designated days, a complete diagnosis of the state of the atmosphere [would] be available". Little did he know, it wouldn't be long for this dream to be realized.

For the prognostic step, Bjerknes assembled a system of equations, specifically seven, one for each variable describing the atmosphere. These included density, pressure, temperature, humidity, and the velocity vector, given by three scalar components. Bjerknes proposed a graphical or graphical/numerical hybrid method derived from the equations or physical

principals for weather prediction. Of course, a numerical prediction of atmospheric flows would be extremely tedious and perhaps impossible to do in a timely manner with the given technology. On the other hand, an analytical solution was simply out of the question without oversimplifying the problem.

In 1913, a man by the name of Lewis Fry Richardson took Bjerknes's ideas a step further. By taking the system of mathematical equations already established by Abbe and Bjerknes and applying finite differencing, Richardson would create the world's first numerical forecast all by hand. Without the aid of modern day technology, he diligently worked for 6 weeks on what would be a 6 hour forecast. His calculations concluded that the surface pressure should have risen an astronomical 145 hPa in 6 hours whereas observations showed the barometer nearly steady (Richardson, 1922).

While this may appear as a complete failure, it was actually "a fairly correct deduction from a somewhat unnatural initial distribution" (Richardson, 1922). He hypothesized that if the initial data were smoothed, results would be closer to those desired. Using modern day technology, Lynch (2006) tested this hypothesis by creating a numerical model nearly identical to the one used in Richardson's calculation. Surprisingly, the 6 hour pressure change was found to be 145.4 hPa, nearly identical to Richardson's findings. Taking this a step further, Lynch remove the initial pressure and wind imbalance found in Richardson's dataset by using a Dolph-Chebyshev filter and recomputed results. Now, a pressure change of only 1 hPa was observed by Lynch, clearly indicating that Richardson's failures were a result of an imbalance in the initial data.

In addition to this 'failed' forecast, Richardson had remarkable insight on what the future of weather forecasting would bring. Below is an excerpt from Richardson (1922), Ch. 11.2, where his fantasy of weather prediction closely describes what numerical models are today. However, the only exception is that his 'computers' are actually humans.

> Imagine a large hall like a theatre, except that the circles and galleries go right round through the space usually occupied by the stage. The walls of this chamber are painted to form a map of the globe. The ceiling represents the north polar

> regions, England is in the gallery, the tropics in the upper circle, Australia on the dress circle and the antarctic in the pit. A myriad computers are at work upon the weather of the part of the map where each sits, but each computer attends only to one equation or part of an equation. The work of each region is coordinated by an official of higher rank. Numerous little "night signs" display the instantaneous values so that neighboring computers can read them. Each number is thus displayed in three adjacent zones so as to maintain communication to the North and South on the map. From the floor of the pit a tall pillar rises to half the height of the hall. It carries a large pulpit on its top. In this sits the man in charge of the whole theatre; he is surrounded by several assistants and messengers. One of his duties is to maintain a uniform speed of progress in all parts of the globe. In this respect he is like the conductor of an orchestra in which the instruments are slide-rules and calculating machines. But instead of waving a baton he turns a beam of rosy light upon any region that is running ahead of the rest, and a beam of blue light upon those who are behindhand.

Richardson estimated it would take an astronomical 64,000 people to forecast weather for the entire globe.

While his *human* factory never saw the light of day, advancements in technology over the next few decades allowed Richardson's dream to become a reality. This included developments and advances in atmospheric dynamics, numerical methods, and the radiosonde, which allowed for observations to be taken over the depth of the atmosphere rather than just at the surface. However, the largest milestone was the invention of the computer which created an unprecedented amount of processing power available to one's fingertips.

At this point, there were sufficient observations to create an atmospheric initialization that could then be integrated forward using the primitive equations. However, the existence of high-speed gravity wave solutions would require a timestep so small that the computational power needed may exceed what was currently available. Fortunately, a man by the name of Jule Charney analyzed the primitive equations using a technique called scale analysis.

From this, he was able to deduce which terms were significant and remove those which were not. The resulting equations completely eliminated gravity wave solutions and increased the minimum time step needed for a numerically stable model. These are known today as the quasi-geostrophic equations.

By early 1950, the first programmed numerical weather model was to be run on the Electronic Numerical Integrator and Computer (ENIAC[1]) in Aberdeen, Maryland. Here, each 24 hour forecast took approximately 24 hours to complete, just able to keep up with the realtime weather. Results showed that large scale features of the mid-tropospheric flow reasonably resemble that of reality, an unprecedented accomplishment. Upon hearing of this success of the ENIAC, Richardson, the man who intrigued the world with the first numerical forecast, responded saying that the results were "an enormous scientific advance".

Over the next few decades our advancements in technology continued to improve weather forecasting. The launch of the weather satellite proved beneficial not only for observational use, but for more accurate initialization via data assimilation as well. This is also the case for weather radar which has developed dramatically since its discovery in World War II when operators noticed that weather was interfering with radar signals. In addition, computers have become exponentially more powerful, allowing simulations to be longer and of higher resolution. This eventually led to the development of limited area models which ingest data from global models for the purpose of running a higher resolution and often more sophisticated simulation.

Today, numerical models are being integrated for extended periods to tackle long term climate problems which may substantially impact us by the end of this century. Contrary to weather forecasts, climate studies embrace the fact that small scale flow features produce large scale changes in the extended period by averaging over long time scales. With this, scientists are able to provide insight on future climate. Of course, if the amount of energy absorbed and released by earth, in addition to the way it was distributed remained unchanged, the long numerical integration should reveal a climate that is identical to our current state. However, this is not the case; anthropogenic alterations in land use (forest

[1]For a complete list of acronyms see appendix A.

to city) and atmospheric composition have already started altering the climate and may have undesirable feedbacks within our land/ocean/atmosphere system. While much is still unknown, a great deal of effort is being put forth to understand these complex interactions and their implications to our planet.

In addition to climate, the use of numerical models is seen throughout many other facets of life and their importance is unprecedented. Travel decisions – whether it be by air, sea, or land, or by private, public, or commercial means – are all dependent on the output of these mathematical models. Additionally, protecting and insuring property now, and even the long term future, is again influenced by numerical output. Finally, one should acknowledge all the lives saved since the inception of the numerical weather model. Unfortunately, estimating lives, time, or money saved by the use of these models is a daunting and perhaps impossible task. However, Lazo et al. (2011) estimated the economic loss due to weather could be roughly 3.4% of the gross domestic product, or 485 billion/yr. in 2008 monetary values. Of course, while this percentage will never become 0, it is hoped that if models continue to advance as they have in the last 65 years, the societal impact of weather variability can be dramatically lessened.

1.1 Model Physics

Since the inception of the numerical weather model, including model physics and physical parameterizations, often going hang-in-hand, have been critical. For example, the solar radiation that shines down on a planet drives the atmospheric motions. This is due to the fact that energy is not distributed evenly but rather favors areas that are perpendicular (the equator) to the incoming radiation. This causes temperature differences, which creates pressure differences that drive the motions of the atmosphere. If this was not considered in a numerical model, one could see how it would severely impede on its forecasting ability.

Calculating how much energy a water droplet absorbs/reflects from a photon of light is a problem of physics. However, the typical resolution of a regional model even today is around 10 km. At this resolution a cloud, let alone the cloud droplet, cannot be explicitly resolved.

This is where things must be parameterized. For the case of radiation, we often use the modeled cloud water and ice on multiple levels that extend the depth of the atmosphere to approximate cloud properties through mathematical formulations. From this, we are able to obtain the average effects of absorption, emission, reflection, and transmission. This physical parameterization will be known as the radiation scheme.

Parameterizations replace processes on scales too small to represent at a given resolution with a more simplified and cost effective solution. As one could imagine, parameterizations are anything but perfect and have large implications on weather forecasts. Because of this, parameterizations are growing ever increasingly complex with much of the work found here – and throughout literature – being devoted to it.

The microphysics parameterization in a numerical model is responsible for handling the conversion of water vapor, to that of cloud water, rain, and every possible combination in between. The more sophisticated schemes introduce cloud ice, snow, graupel, and hail. Additionally, some schemes predict (rather than diagnose) the number concentration of a variable in addition to the mass; this is what we call a double-moment scheme. The advantage here is that for a given mass, the double-moment scheme can have a different number of cloud droplets depending on conditions. One condition might permit a large number of droplets, discouraging precipitation, while another scenario may have a smaller number of larger droplets that would encourage precipitation. The disadvantage of the double-moment schemes is that they can be computationally intensive, which is notable especially since these calculations are normally performed every time step.

For the reasons discussed above and various others, the choice of microphysics has been known to create sizable differences when simulating thunderstorms (Rajeevan et al., 2010). Perhaps more surprisingly is the ability for microphysical processes to have a sizable influence on hurricane tracks (Fovell and Su, 2007). It was later shown that these differences may have arisen due to cloud-radiative feedbacks indicating that the distribution of microphysics mass variables (water, ice, etc) may be important for things other than precipitation (Fovell et al., 2010). Unsurprisingly, the work done in subsequent chapters of this thesis found even non-precipitating clouds/fog sensitive to this parameterization.

While the microphysics and radiation schemes directly interact with all atmospheric model levels, the lower boundary of a numerical model is controlled by the Land Surface Model (LSM), sometimes referred to as the surface scheme. Here, energy obtained via the radiation scheme is either absorbed or reflected depending on the assigned land use[2] albedo. Of the energy that is absorbed, some of it is stored in the ground which may be released later that night, or in a subsequent season. How efficiently the heat moves through the ground is often parameterized by the soil properties and moisture, though simpler methods are still used today.

Depending on the conditions, a vast majority of the energy that hits the earth and is absorbed does not go into the ground for storage. In fact, much of it is whisked away into the atmosphere either by direct conduction, which we call the sensible heat, or by evaporation/sublimation, called latent heat. Of course, the heat transfer can exist in either direction with the opposite coinciding with condensation/deposition.

When water evaporates from the earth's surface it requires energy, leaving the ground cooler. However, this energy transferred to the atmosphere in what would now be water vapor would not be observable using a thermometer, it is in a sense, hidden. In fact, the energy only produces a rise in temperature during the phase transition back to a liquid or solid. This is in contrast to the sensible heat flux which could cool the earth's surface at the expense of instantaneously warming the atmosphere. As one will come to appreciate, how the LSM partitions the incoming energy into the ground, sensible, and latent heat flux is important to accurately capture future weather conditions.

A simplified version of the sensible heat flux can be presented as

$$H = -\rho c_p C_H(\theta_1 - \theta_s) \tag{1.1}$$

$$C_H = \frac{k u_*}{ln(\frac{z_1}{z_{0T}}) - \psi_H} \tag{1.2}$$

$$u_* = \frac{k U_1}{ln(\frac{z_1}{z_{0M}}) - \psi_M} \tag{1.3}$$

[2]Typically, there are 20-30 land use categories in a numerical model that attempt to parameterize every type of land surface on the globe.

where H is the sensible heat flux, ρ is density, c_p is the specific heat at constant pressure, and θ_1, θ_s are the potential temperatures at sigma level one[3] and the surface, respectively (Shin et al., 2012). One can see that the sensible heat flux is not only dependent on the temperature gradient, but also on a function called the exchange coefficient, C_H (Eq. 1.2).

The calculation of this important variable (C_H) is performed within the surface layer parameterization. This physics package couples the land to that of the atmosphere and modulates the exchange through the exchange coefficient. This calculation is dependent on many other variables including: the von Kármán constant (k), the height of sigma level one (z_1), the surface roughness length for heat (z_{0T}) which increases for uneven surfaces, and ψ_H, the stability function for heat which varies among parameterizations.

Finally, the exchange coefficient is dependent on the friction velocity (u_*) which again is calculated in the surface layer and can be thought of as a shear stress rewritten in terms of velocity. Here, U_1 is the wind speed at the lowest sigma level and the subscript 'M' in the stability function and roughness length represents momentum. While these equations can be formulated a number of ways depending on the chosen surface layer parameterization, one can still get a general insight into how the exchange of energy is modulated. For example, an increase in wind speed would act to increase the friction velocity. In turn, this would increase the exchange coefficient along with the sensible heat flux. Essentially, the faster the wind, the more heat we can exchange with the surrounding atmosphere.

As energy is exchanged between the land surface model and atmosphere via the surface layer parameterization, thermally induced motions begin to develop. Since numerical models are often run at relatively coarse horizontal resolutions (1-50km), they are unable to resolve the turbulent eddies that exist in the atmospheric boundary layer[4]. A way to solve this problem is to introduce a scheme that can parameterize the average effects of these eddies. In a numerical model this is called the Planetary Boundary Layer (PBL) scheme.

While the PBL may appear to be a glorified atmospheric mixer, its presence in a numerical

[3]Sigma level one refers to the first model layer above the surface

[4]The atmospheric boundary layer is the portion of atmosphere that is directly influenced by the earth's friction and surface fluxes.

model should not be overlooked. For example, in a wind forecasting application one may be interested in the exact timing and strength of transient features. To a very large degree, the surface wind speed is dependent on the amount of momentum that gets mixed down to the earth surface. If momentum is not being mixed down, you often see a lull in the wind speeds as friction from the earth's surface begins to dominate. Because these thermally induced motions are more active during the day, it is also the time we observe higher wind speeds on average. Of course, all of this will be controlled by the boundary layer parameterization.

Additionally, one could imagine that an overmixed and undermixed PBL could have important consequences that feedback throughout all the physics packages within the model. Say for example there is a conditionally unstable environment in which if a certain surface temperature is achieved, a large amount of potential energy will be released creating widespread thunderstorms. An undermixed PBL may have a larger superadiabatic lapse rate near the earth's surface, which equates to a warmer surface temperature and the triggering of thunderstorms. The opposite may be true for a PBL that was overmixed, perhaps inhibiting the formation of all storms. As explained here, one would expect to see the timing and strength of thunderstorms to very amongst PBL parameterizations.

Finally, another important process that takes place in the PBL – other than vertical diffusion – is entrainment. Often times an energetic thermal will overshoot its equilibrium point, which in this case we will use as the PBL top. An overshooting thermal is equivalent to a pendulum swinging past its point of equilibrium due to the inherit momentum. Beyond this point, the thermal will become colder than its surrounding environment and will want to sink back down to the PBL top. However, in the process of overshooting, air from the free atmosphere and that of the PBL mix and acquire properties from each other. While the mixing can seem subtle, it can be important when air between the boundary layer and free atmosphere have stark differences in temperature and/or absolute humidity.

While there are other physical parameterizations in numerical models, the planetary boundary layer, land surface model, surface layer, microphysics, and radiation are the major components. Although each of these schemes work independently, they influence one another either directly or indirectly. The majority of this thesis will focus on the planetary boundary

layer and land surface model parameterization and their influence on forecasting the evolution and life-cycle of cold pools.

1.2 Cold Pools

Whiteman et al. (2001) defined a cold pool as a topographically confined, stagnant layer of air overlaid by warmer air aloft. A dramatic and well known example is the Tule fog of California's heavily populated Central Valley (CV), which can persist for several days. If a cold pool lasts longer than one diurnal cycle it is classified as a persistent, whereas diurnal cold pools form at sunset and decay at sunrise (Whiteman et al., 2001). While the Central Valley is a common example, cold pools are most prevalent in mountain valleys during periods of high atmospheric pressure, light winds, and low solar insolation (Daly et al., 2009). Due to their characteristic inversions, cold pools are also conducive to freezing rain which creates a hazard to transportation and safety (Whiteman et al., 2001).

Advancements in modeling cold pools need to be made not only for forecasting fog and precipitation type, but also for air quality as it is of great concern to the U.S. Environmental Protection Agency (EPA) Office of Air Quality Planning and Standards (Baker et al., 2011). The meteorological conditions associated with cold pools create stagnant air that cannot mix out vertically due to capping inversions. This increases ozone or PM2.5 (Particulate Matter with a diameter <2.5 μm) concentrations that can exceed the National Ambient Air Quality Standard (NAAQS) in many parts of the Western United States including, but not limited to, the Pacific Northwest, the Central Valley of California, and Great Basin (Gillies et al., 2010). Of course, elevated ozone and PM2.5 levels pose a large health risk to many Americans. Despite the impact they impose on air pollution and weather, persistent cold pools have received relatively little research attention (Zhong et al., 2001).

In this thesis, an attempt to properly fix the cold pool modeling problem in California's CV will be undertaken, specifically those events involving radiation fog. Most recently, Ryerson (2012) noted the Weather Research and Forecasting (WRF) model's (Skamarock et al., 2001) inability to produce fog in and around the CV, which was largely attributed to an

overnight warm bias. In order to fix this, he applied post-processing corrections which added significant overnight skill; however, due to the non-linear evolution of fog and its interactions with model physics, only modest skill increases were seen after sunrise. This thesis is not an attempt to amend the cold pool modeling problem via post processing techniques, but rather, by way of model physics improvements.

The WRF model, along with the Fifth-Generation National Center for Atmospheric Research (NCAR)/Penn State Mesoscale Model (MM5), have failed to reproduce the intensity and persistence of cold pools despite systematic improvements to both model physical parameterizations as well as horizontal and vertical resolution (Baker et al., 2011). Data assimilation and surface nudging have also been explored, both failing to add value to the already poor representation of cold pools (Avery, 2011). Of the cold pools that are resolved, they often mix out too early, leading to erroneous surface temperatures, ozone, and PM2.5 concentrations (Avery, 2011). It is becoming increasingly clear that a cold pool-aware surface and/or boundary layer schemes are needed in WRF to accurately reproduce these stagnant air quality episodes (Baker et al., 2011; Avery, 2011).

The process of cold air pooling can be enhanced by sheltering from valleys and nearby trees that effectively reduce the vertical mixing that would otherwise bring warmer air down to the surface (Gustavsson et al., 1998). In addition to this, Whiteman (2000) has demonstrated that further cooling in valleys is possible simply because of their shape; a cross-sectional column of air over a valley is always less than that of flat terrain. That said, Whiteman et al. (2004) showed the cooling effect is counteracted by the the downward longwave radiation originating not only from the atmosphere, but also from the valley walls. While the influence of these effects is most certainly dependent on valley size, an exact relation is unclear.

1.2.1 Drainage Flows

The usual conceptual model concerning the formation of valley cold pools involves cold air drainage. Just after sunset, winds diminish and a shallow, stable, boundary layer forms due

to the strong radiative flux divergence. Negatively buoyant air originating on the side slopes of the valley descends to the stable layer, detaches from the side wall, and flows out over the center of the basin (Clements et al., 2003). Essentially, the air above the valley center is efficiently cooled by the basin walls before becoming detached; this acts to enhance the cooling *above the surface* due to the sensible heat flux divergence (Whiteman et al., 1996).

Nevertheless, Whiteman et al. (1996) found the sensible heat flux at the valley floor to be near zero. Neff and King (1989) produced similar results in their research showing that drainage flows along the Colorado River basin overlay a stronger surface based inversion of lighter winds. This suggests that the cooling above the surface can be due to advective effects while the cooling at the valley bottom occurs *in situ*. It should be noted that cooling aloft by drainage flows indirectly assist the *in situ* cooling at the surface by reducing the downward longwave radiation. Though this effect is suspected to be insignificant, it is currently unclear how important it may be.

Drainage flows do not always become detached from the basin walls and have been well observed flowing in valley locations (Hootman and Blumen, 1983; Gudiksen et al., 1992; Bodine et al., 2009). Yet, their role in the production of cold pools remains controversial. In the 1997 Cooperative Atmospheric Surface Exchange Study (CASES-97) at the Walnut River watershed in Kansas, LeMone et al. (2003) attributed cold temperatures at the low elevation sites to cold air drainage and radiative cooling. However, the fast drainage flows observed at higher elevations were extremely weak lower down, causing the authors to suggest that the flows were elevated over a more dense cold pool. Mahrt et al. (2001) examined the CASES-99 observations in south-central Kansas and found that while the drainage flows do exist, their influence on the surface fluxes was undetectable because the shallow flows decoupled the observations (located at 3-10 m) from the surface. This result stems from the limitations of the eddy correlation flux measurements on surface flux estimation. It is worth noting that of the surface fluxes measured, the sensible heat remained downward-directed; that is, the air acted as a heat source throughout the night.

In contrast, earlier research performed by Thompson (1986) suggests that cold pool formation in open and closed valleys is a direct result of sheltering and *not* cold air drainage;

the latest research agrees. In the gently sloping terrain of Oklahoma, Hunt et al. (2007) concluded that the cooling observed in cold pools occurred *in situ* which counters the results of LeMone et al. (2003). More recently, Bodine et al. (2009) found that cold pools were suppressed by the katabatic winds in the Lake Thunderbird Micronet, a dense collection of surface stations (28 stations) in the gently sloping terrain of Lake Thunderbird, Oklahoma. In fact, they went as far as stating that, "pooling of cold air as a result of drainage flow can clearly be excluded as a factor causing the CP [cold pool] development at the micronet". Instead, cold pool formation was likely caused by the cooling that occurred *in situ* due to the radiative heat loss and diminishing turbulent heat transfer in sheltered regions.

Sometimes, drainage flows are not even observed, as Clements et al. (2003) has shown. When inspecting the closed 1 km Peters Sinks basin in Utah, the winds ceased in the entire basin roughly 2 hours after sunset when they became "too weak to measure accurately". This led to their conclusion that downslope flows in the Peters Sinks basin play only a minor role in the formation of cold pools. These weak flows were somewhat expected as Katurji and Zhong (2012) have shown that weaker drainage flows do correspond to smaller basins with larger slope angles in two-dimensional idealized simulations. Additionally, they found the main cooling process near the basin floor (<200 m) to be the longwave radiative flux divergence, while vertical advection dominated the cooling process in the upper basin area.

Although the production of cold pools may be slightly controversial, the latest research (as previously discussed) agrees that *surface* temperatures are not further reduced due to the direct effects of cold air drainage. To further reinforce this point let us consider the following thought experiment: Imagine there is a V-shaped valley and for the sake of this experiment, the size does not matter. It is midafternoon, the atmosphere is well mixed and adiabatic up to the rim of the valley. Additionally, the valley bottom and adjacent sidewalls are identical, meaning vegetation and soil properties are the same.

After sunset the atmosphere begins to cool and any sort of mixing ceases to exist. Since surface properties are homogeneous along with the potential temperature, the sidewalls cool at exactly the same rate as the valley bottom. Looking at a horizontal cross section part way up the valley one would notice that the air near the sidewalls becomes cooler than the

open air. This makes sense because the air closest to the sidewalls is cooling via conduction. Because of this horizontal temperature gradient, the air near the sidewalls begins to flow downslope.

As the air descends it continues to cool at the same rate as the air at the valley bottom and does not entrain any warmer air that exists just above. Of course, this lack of entrainment from downsloping air is clearly unphysical but for the sake of creating the coldest possible temperatures, there is no entrainment. Because the cooling rates are identical, the downsloping air still has the same potential temperature as the valley bottom. This process will continue until this air finally reaches the lowest possible point. At this time one will discover that the descending air is not cooler nor warmer than the preexisting valley bottom air; in fact, they have the exact same temperature.

Even with this best case scenario there are a couple of issues. As previously mentioned, the lack of entrainment from downsloping air is physically unrealistic. Because of its movement, it would likely entrain more than the valley bottom which would impede on its ability to descend to the basin floor. Secondly, assuming that the sidewalls could cool the drainage flows as efficiently as the valley bottom is a stretch since there would likely be less sheltering here. Finally, cooler air would begin to pool at the valley bottom which would subsequently reduce the downward long wave radiation (Zängl, 2005) and increase the static stability which would further reduce temperatures. This would allow the air at the valley bottom, which now has cooler overlying air, to cool faster than the air near the valley walls.

In most cases, the sensible heat flux is already negligible (Whiteman et al., 1996) so further reduction may result in trivial changes. However, as previously discussed, it is unclear how important the pooling of cold air and subsequent reduction in long wave cooling is on the formation of cold pools. Although, with increasing valley bottom width, the depth of the cold air pooled will become shallower since there is a larger volume to fill.

Finally, it was assumed that the cooling rates and hence the net radiation would be identical along the slope and in the valley. It will be shown later that in a dry adiabatic atmosphere, this is certainly not the case. Moreover, the addition of water vapor, which is

concentrated in the lower atmosphere, further complicates the picture.

For now, one can appreciate that drainage flows directly cool the basin atmosphere (aloft) with diminishing effects near the surface. At the bottom, indirect cooling effects likely dominate but in the case of the thought experiment, would be hindered by turbulent exchanges induced by the drainage flows. This is perhaps why research says that drainage flows can both help and hurt the formation of valley cold pools, because it is all a matter of perspective. Determining what valley size these direct and indirect effects become negligible in addition to their sensitivity to resolution will impact the results of this thesis and will be addressed in Ch. 2.3.

1.2.2 Radiation Fog

Given a sufficient amount of low level moisture, some cold pools can cool (via radiation) to the point of saturation. Considering the ground and the debris that lays upon it emits radiation most efficiently, it is the coldest surface and is where condensation begins. The liquid (frozen) water that collects here is called dew (frost). However, given enough cooling, water vapor will condense in the atmosphere on a cloud condensation nuclei and produce a fog droplet.

Since water is very good at emitting radiation, the fog droplet can still continue to cool and grow while settling to the earth's surface. Here, the fall speed is proportional to the radius squared since Stokes' law explains the drag force is proportional to the radius while the opposing gravitational force scales with the mass and thus radius cubed. Including gravitational settling is important since the absence of such a process has been shown to increase liquid water paths by a factor of two or more (Bergot et al., 2007).

As the surface and droplets above continue to emit radiation, the depth of the fog layer grows. This essentially increases the liquid water path radiation must travel through in order to reach space. Since water is very good (relative to the gases in the atmosphere) at emitting radiation, it is also equally good at absorbing it. Thus, the radiation emitted from the surface it easily absorbed and emitted back down to the surface. This means that as the

fog gets thicker, the surface radiational cooling effectively shuts off. From this point forward, fog top cooling dominates and is the main cooling mechanism for continued fog growth.

As one could imagine, cooling the top of a fog layer while not subsequently altering temperatures below would allow the profile, if given enough time, to become unstable. This is exactly what Holets and Swanson (1981) observed during a 5 day fog episode in California's Central Valley where lapse rates [in the fog layer] were between moist and dry adiabatic. Above this fog layer, they noted an average stability of 2.9 K 100 m^{-1} (though extreme values of 6.1 K 100 m^{-1} were observed) that varied in thickness from 200-1000 m.

This is perplexing because cold pools are always thought of as stable conditions. Additionally, radiation fog will almost always start with a stable profile. It is not until the fog layer is deep enough to shut off surface radiational cooling can it transition to an unstable layer often capped by a stable layer.

These meteorological conditions are not atypical and are found throughout cases studied in this thesis. Because cold pools can exist in two entirely different regimes, that is stable and unstable capped by stable, differentiation between the two is important for discussions and modeling purposes. For this reason, we will be referring to these unstable fog layers as *adiabatic cold pools*, with reference to the temperature profile they subsequently create.

Fog top cooling in adiabatic cold pools can have important consequences on the structure and longevity of fog. For example, the fog top cooling continuously creates unstable conditions in adiabatic cold pools and subsequently drives turbulence in this region. This particular area is the boundary between cooler, saturated air and warmer, drier air. Thus, any sort of turbulence and hence mixing can create entrainment which would increase temperatures in the adiabatic cold pool while simultaneously drying out the layer.

Unfortunately, there has been relatively little research attention on this particular fog top entrainment mechanism. Of the research that has been done almost all (if not all) pertains to the marine boundary layer. After all, low level clouds/fog frequently occur over oceans making them ideal for studies of such processes despite the fact that they are not topographically confined. In Ch. 4 the importance of such entrainment and its impact on

the longevity and life cycle of fog will be discussed.

A well-known process that degrades adiabatic cold pools is vertical wind shear at the fog top. Perhaps the most famous relation of turbulence to wind shear is the Richardson number:

$$Ri(z) = \frac{\frac{g}{\overline{\theta}}\frac{\delta\theta}{\delta z}}{\left(\frac{\delta U}{\delta z}\right)^2} \tag{1.4}$$

where g is the gravitational acceleration due to the earth's mass, θ is the potential temperature, z is height, and U is the wind speed. As Lyons et al. (1964) pointed out, there is an inverse relation between turbulence and a Richardson number less than 1. While they showed no definitive critical Richardson number, a value where turbulence would spontaneously begin, it was hypothesized that if one did exist, it must lie between 0.25 and 0.5 (Lyons et al., 1964).

Further exploiting this relation, one can clearly see that it is not only dependent on shear, but the stability of the atmosphere. As previously mentioned, Holets and Swanson (1981) observed an adiabatic fog layer of approximately 500 m in depth with a mean temperature near freezing and a moderate stability (2.9 K 100 m^{-1}) above. Now, if one considers that the inversion is approximately located at 950 hPa and an additional 100 m is roughly 10 hPa, the change in potential temperature over the inversion is approximately 3.8 K 100 m^{-1}. Inputting these variables into Eq. 1.4 results in a shear to Richardson number relation plotted in Fig. 1.1. Here, the dependence is inversely proportional to the shear squared where a Richardson value of 1 is approximately equal to a 100 m layer shear of 3.7 m/s. Certainly, not a small value. Perhaps a more appropriate Richardson number to use would be 0.25 which equates to a layer shear of 7.4 m/s. As one can observe, shear can certainly influence the longevity of a cold pool by creating turbulence and subsequently entrainment, however, with the protection of the thermal inversion it severely limits its influence.

Another well known process that encourages the break up of fog is the absorption of solar radiation, whether it be by the droplets or the ground. The radiation absorbed here destroys the cold pool in two different ways. The most obvious is the warming of the air mass

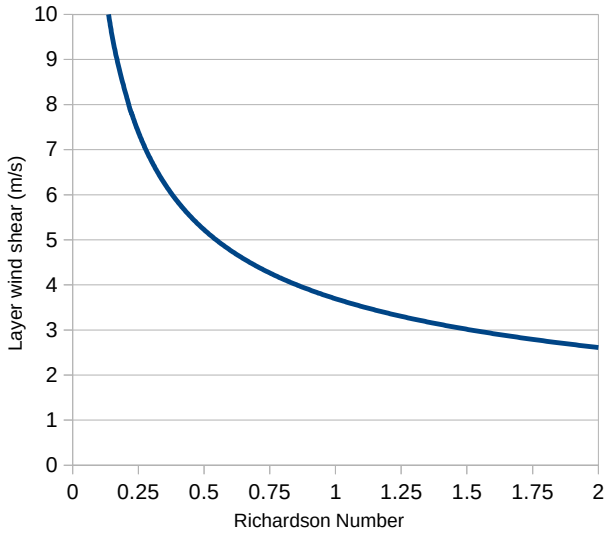

Figure 1.1: The resulting shear to Richardson number relation over a depth (z) of 100 m using an ambient temperature of 273 K and a lapse rate of 3.8 K.

which subsequently increases the amount of water vapor it can hold. This will evaporate some of the cloud water which will reduce the liquid water path and increase the amount of radiation absorbed at the surface. This is a positive feedback, a process that feedbacks to further amplify itself.

The second, less obvious, process occurs when thermals originating near the earth's surface rise to the top of the boundary layer and overshoot the level of neutral buoyancy. This level is often the fog top, which means that any overshooting that does occur will result in entrainment of warmer and drier air. This process, though not obvious, is parameterized in the model physics that is used in this thesis.

This is in contrast to thermals which originate near the cloud top and are negatively buoyant (due to the previously mentioned cloud top cooling) . These sinking thermals are currently not parameterized in the physics used throughout this thesis which is an enormous problem due to the turbulence and entrainment they create. In fact, these negatively buoyant thermals are so important that all of Ch. 4 will be devoted to capturing their effects in a numerical model while understanding their significance on the evolution and life cycle of cold pools.

Other factors controlling the life cycle of fog include soil moisture, soil type, aerosols, and most certainly, synoptic conditions. As one can imagine, soil moisture directly controls the Bowen ratio which is the ratio of latent to sensible heat. Here, the latent heat helps to maintain a foggy boundary layer while the sensible heat acts to destroy the cold pool by adding more energy to the layer. It is hypothesized that soil moisture may be instrumental in our ability to properly model the evolution and life cycle of fog and will be discussed in-depth in subsequent chapters.

Additionally, soil types can control variables such as the thermal inertia, the ability of an object to resist temperature change. A surface with a lower thermal inertia would cool faster than one with a higher thermal inertia. A colder surface would allow fog to form earlier and more frequently. However, soils with low thermal inertia indicate a lack of moisture. This is due to the fact that water has a very large heat capacity and thermal conductivity which can dramatically alter soil properties. So, given the fact that a sufficient amount of moisture must be present for the formation of fog, it seems unlikely that a low thermal inertia would also exist.

It is well known that aerosols can change the active number of cloud condensation nuclei and subsequently cloud droplets. Since the volume of a droplet scales with the radius cubed and the surface area relates to the radius squared, a larger number of small droplets would be more optically thick. This would change not only the microphysics but also how the radiation and microphysics interact which would have consequences on the surface energy balance. While these important effects are not covered in this thesis, a lot of work has been focused on aerosols and their role in microphysics.

The interactions between radiation fog and the local environment are without a doubt numerous, yet largely controlled by synoptic conditions. Shear created by an approaching front can create turbulence and drive entrainment. Additionally, cold air advection aloft can destabilize the atmosphere, increase the boundary layer depth, and subsequently mix out the fog. Furthermore, moisture provided by a front can help reestablish ideal conditions for fog formation. Finally, a building ridge can create the clear skies and stagnant conditions which are ultimately needed for the formation of radiation fog. While all these processes

cannot be studied in detail, a handful of them will be in subsequent chapters.

1.3 Model Setup

Using WRF version 3.5 and 3.5.1, radiation fog and the processes which govern it will be investigated in detail in both the real and idealized setting. Real data simulations include a triply nested design with horizontal resolutions of 36, 12, and 4 km; however, not all simulations will employ domain 3. The area encompassed by the 36 km domain can be seen in Fig. 1.2 with the 12 and 4 km nest outlined by the white rectangles. Experiments will use a variety of vertical grid arrangements with specific details outlined in each chapter. Additionally, model physics will vary and be specified in the appropriate sections but is also outlined in appendix B for convenience.

Validations of weather reconstructions have been performed principally with the Model Evaluation Tools (MET) software, maintained by the Developmental Testbed Center at NCAR. This package was used to compare observations to model reconstructions that were spatially interpolated to the observation point. Observational data were collected from several different sources and outlined in each chapter. Locations of surface Automated Weather Observing System (ASOS) and Automated Surface Observing System (AWOS) stations used in statistics throughout the thesis are highlighted in red dots (Fig. 1.2).

The Central Valley (CV) verification region, known as the CV subset from this point forward, is outlined by the white polygon and encompasses the entire valley. In the middle of the polygon is a white line transecting the valley which divides the CV subset into two smaller regions. The northern and southern portions will be referred to as the Sacramento and San Joaquin subsets, respectively. While most of the methodology is chapter specific, these are the similarities which will be shared throughout the entire thesis.

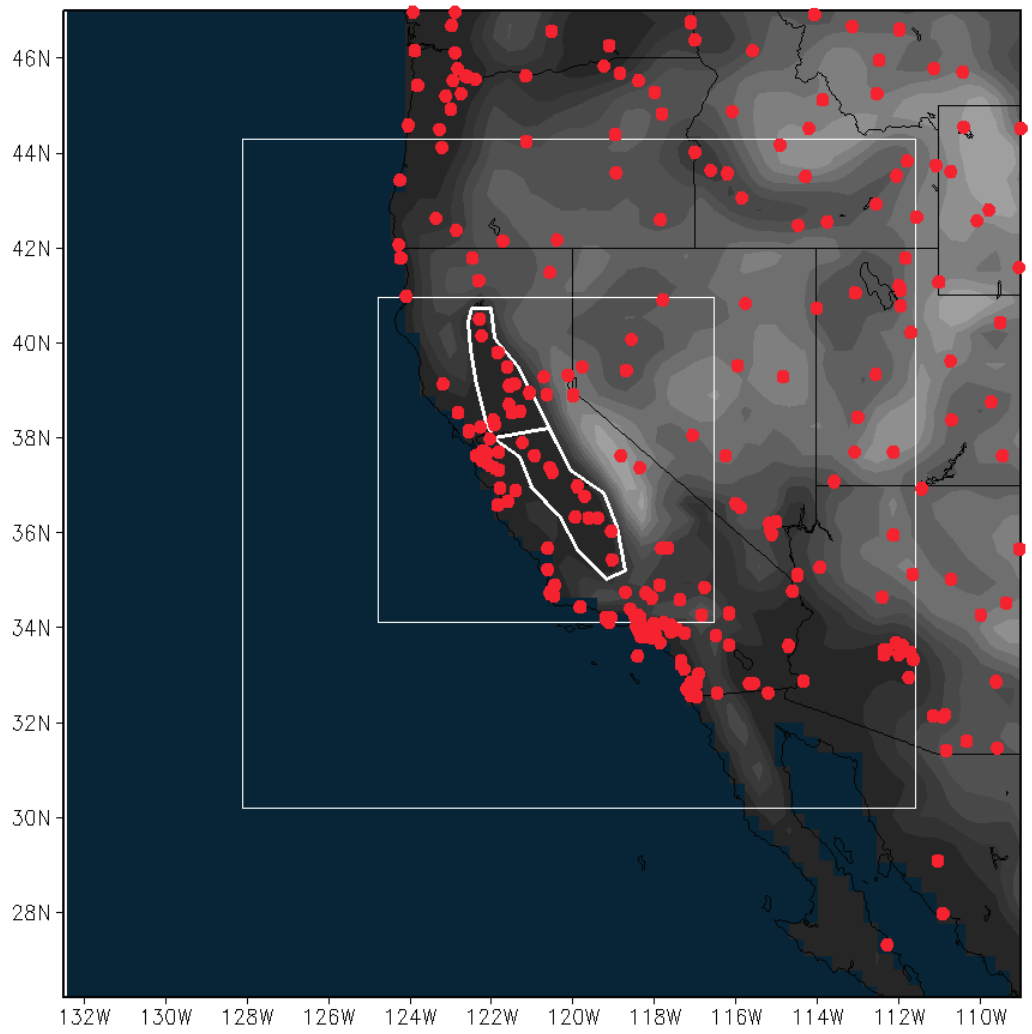

Figure 1.2: The 36 and 12 km domains used throughout all real data simulations is shown along with terrain shading from the 36 km domain. Some experiments will employ the third and innermost domain which uses a horizontal resolution of 4 km and is centered over California's Central Valley. The red dots represent surface ASOS or AWOS stations used to verify the model while the white polygon encloses stations used in the CV subset (full valley). The white line transecting the polygon separates the Sacramento subset (northern half) from the San Joaquin subset (southern half).

CHAPTER 2

Stable Cold Pools

2.1 Methodology

Using WRF version 3.5, stable cold pools in California's Central Valley will be modeled with and without several modifications to the default WRF. The cold pools that are referred to here are indeed stable (with ice-liquid water potential temperature[1] increasing with height) and not adiabatic. It is important to note that the success of modeling adiabatic cold pools is dependent on the ability to properly capture their stable counterparts which often precede. Thus, this chapter will focus exclusively on our understanding and ability to forecast stable cold pools.

To begin, different atmospheric initializations were tested and their influence on cold pool formation was deemed relatively unimportant; because of this, all atmospheric variables will be initialized from the North American Regional Reanalysis (NARR). In contrast, simulations were sensitive to the soil initialization. Consequently, we have chosen to extract these surface fields from a variety of sources including the NARR, North American Mesoscale model (NAM), the European Reanalysis (ERA) Interim, and from offline simulations spun using NCAR's High Resolution Land Data Assimilation System (HRLDAS). Forcing for the HRLDAS system was made available via phase 2 of the National Aeronautics and Space Administration's (NASA's) North American Land Data Assimilation System (NLDAS).

Spun soil, or spun surface fields, pertain to the fact that initial soil variables were created from an offline LSM that started before the time period of interest. Here, offline simply refers to the fact that the LSM model was forced using a previously created dataset and

[1]The ice-liquid water potential temperature is the potential temperature minus the heat created from condensing all water and ice within a parcel.

not a full-fledged numerical weather model. Since soil moisture has a memory footprint of months to years, the past must be know in order to initialize a numerical model with correct present day values. In this sense, it would be impossible to get credible results without spun soils and is the reason why all soil datasets are. However, all datasets are done so with different LSMs (or different version) creating inconsistencies.

The simulation period of interest is December 4-16, 2005, a mostly dry and stagnant period conducive to cold pool formation. During this time, minimal precipitation fell from a weak front that made its way through the CV on December 8 and 9. Model reconstructions will combined a sequence of shorter, overlapping simulations, in which a new run is initialized (as a cold start) every other day. This means the first 24 hours is overlapped by the previous simulation and is subsequently removed. Offline HRLDAS simulations were initialized from the NAM model January 1, 2004 and integrated until our time of interest, December 2005.

The model setup includes a doubly nested design with a horizontal resolution of 36 and 12 km in addition to 51 vertical levels (Fig. 1.2). The standard model physics includes Lin microphysics, the Rapid Radiative Transfer Model (RRTM) and Dudhia radiation, Yonsei University (YSU) PBL scheme, and the Kain-Fritsch cumulus parameterization. In this chapter, this setup will be referred to as the default WRF.

Observational data were collected from the Meteorological Assimilation Data Ingest System (MADIS) which consists of surface ASOS and AWOS stations. The exact locations of these data used to verify the model are shown in Fig. 1.2 (red dots). Since we are modeling cold pools in California's CV, results will focus on statistics averaged over all CV stations, the CV subset.

2.2 Results

Observed and modeled relative humidity (RH) from December 5-8 for the CV subset can be seen in Fig. 2.1 with error bars representing plus or minus one standard deviation. Here, overnight relative humidity values are extremely moist – upwards of 90% – and the variation among observations is quite small. In contrast, the default WRF using atmospheric and

soil initializations from the NARR – abbreviated Noah/YSU NARR – is several standard deviations away from reality. Only slightly better, despite it being our best reconstruction, is the Noah/YSU NARRera; abbreviated this way because the atmosphere is still initialized from the NARR, but uses soil information from the ERA-Interim. Furthermore, simulations with soil information from the HRLDAS and NAM – labeled NARRspun and NARRnam, respectively – are quite comparable.

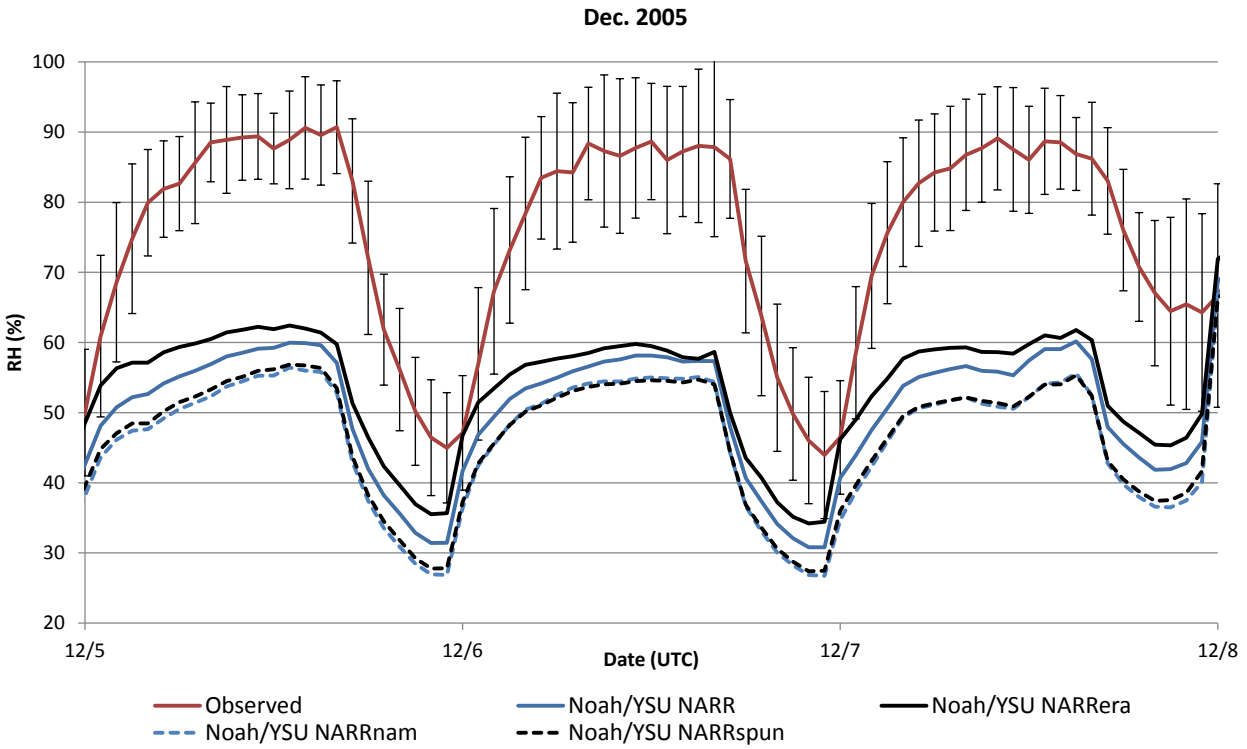

Figure 2.1: Observed and modeled RH for the CV subset (Fig. 1.2) during December 2005. Plus or minus one standard deviation for observed RH is shown.

It should be noted that the large errors seen during this time period are by no means unique, but rather quite typical. If one inspected the entire simulation period, December 4-16 (shown later), results look very similar. Furthermore, reconstructions from different years yield the same answer and employing the higher resolution 4 km nest (in the absence of horizontal diffusion on model levels) does not add much value. Finally, this bias in relative humidity is a result of both warm overnight temperatures and low dew points.

2.2.1 Areas of Improvement

The default WRF is by no means capable of forecasting cold pools as shown in Fig 2.1. In fact, it will be demonstrated that due to the models inherent problems and deficiencies, WRF actually prevents the formation of cold pools. Because of this, a number of modifications will be performed to properly forecast cold pools in the Central Valley.

Horizontal Diffusion

By default, the WRF model accounts for subgrid scale mixing in the vertical via the PBL scheme and in the horizontal by an option called `diff_opt` (diffusion option). Here, diffusion option 2 performs calculations in physical space which is desirable. Unfortunately, option 2 requires extremely high resolution that is not used in this thesis. Trying to employ this option at a lower resolution creates instabilities due to the sharp terrain gradients and subsequently crashes the model within a few timesteps.

The alternative is diffusion option 1, the model default. This option performs the subgrid scale mixing not in physical space but on model levels. This is a problem since it has been shown that horizontal diffusion operating along sigma coordinates can have an impact on forecasting topographically confined cold pools (Billings et al., 2006; Zängl, 2005). This is due to the fact that adjacent grid points can differ dramatically in height, which in terms of cold pools, means stark differences in temperature, condensate, and water vapor. These apparent horizontal gradients – which are an illusion from the model coordinate – allow diffusion to be erroneously active.

Looking back to the Dec. 2005 cold pools, particularly Dec. 5-8, one can find the average overnight (12Z) relative humidity in the Central Valley is around 87% (Fig. 2.1). This is compared to our NARR and HRLDAS initialized soils which had a relative humidity of 58 and 54%, respectively (Fig. 2.1). As it will be shown, deactivating diffusion and rerunning simulations results in an 11% increase in overnight relative humidity. Certainly a large improvement, but values still several standard deviations away from the observed mean. Thus, additional options need to be explored.

Coupling Strength

The coupling strength is the amount of interaction between the atmosphere/land and is controlled by the exchange coefficient, C_h, among other factors. Chen and Zhang (2009) found that the Noah LSM underestimated values of C_h in forested regions while simultaneously overestimating it in more barren landscapes. In order to account for the changes in coupling strength due to vegetation heights, they made modifications to the thermal roughness length that resulted in long-term improvements when compared to AmeriFlux data; a compilation of sites with automated and handmade measurements of ecosystem carbon, water, and energy fluxes. Simulations presented in this chapter also benefited from this option and will be discussed in depth momentarily. We will refer to this option as 'IZ0TLND', or more simply 'IZ0'

Shifted Levels

Our last area of improvement focuses on the height of the lowest model level. By default, this level is set to 0.993 which is approximately 27 m above the surface and is independent of the number of vertical levels specified. In some experiments the lowest sigma value was manually set to 0.997 which is approximately 13 m above the surface. Among other things, this causes a change in the energy balance. Additionally, the next 4 model levels are also shifted downwards so there is no large jump in resolution. This acts to increase the resolution at the surface while decreasing it – though slightly – aloft since no additional levels were added. The exact values of each level, relative to the default, can be seen in Table 2.1. This modification will sometimes be referred to as 'levels' or 'shifted levels'

Default	0.993	0.983	0.970	0.954	0.934	0.909	nz=51
Shifted	0.997	0.986	0.972	0.955	0.935	0.909	nz=51

Table 2.1: Default and shifted sigma levels used in WRF simulations. Both use a total of 51 vertical levels (nz).

2.2.2 Results with improvements

The results with (sometimes referred to as the cold pool configuration) and without (the default WRF) the 3 areas of improvement are presented in Fig. 2.2 from December 6-8. Here, the observed temperature (at top) and dew point (at bottom) are plotted against the default simulation (black) for the CV subset. The previously discussed warm bias in temperature and dry bias in dew point – a common occurrence throughout our entire simulation period – can be observed. Now, by turning off diffusion (Noah/YSU diffopt0) acting on model levels, an improvement in both temperatures and dew points can be seen. It should be noted that the spike in modeled dew points seen around sunset (Dec. 7) is a diagnostics problem and is not visible in sigma level one dew points. The exact reasoning for this is unknown.

Implementing all improvements, which is labeled as Noah/YSUlevels IZ0 diffopt0 (gray line), one can see another incremental decrease in temperature and increase in dew point. Here, dew points are improved but are still too dry in the latter parts of the simulation. In contrast, this configuration has virtually no overnight minimum temperature (15Z) bias when averaged over the entire simulation period (only 0.1 K), December 4-16. This is a substantial improvement over the default WRF which had overnight minimums that were, on average, 2.4 K too warm.

While the IZ0TLND option helps to increase dew points in the Central Valley, an increase in evaporation is not seen in this area. However, changes in the surrounding terrain do appear. Figure 2.3a illustrates this by showing the average (December 6-8, 2005) latent heat flux difference between a run utilizing IZ0TLND to one that does not. The areas with the largest differences arise from the United States Geological Survey (USGS) landuse categories that have the largest roughness lengths, landuse 11-15 (forested regions). Additionally, just by shifting the levels, evaporation further increases (Figure 2.3b), though by a substantially smaller amount. During this 48 hour period one can see that the increase in evaporation from the run utilizing the IZ0TLND option is roughly 5-25 W/m^2 more in the surrounding terrain while the shifted levels help to further amplify the flux by approximately 5 W/m^2. It should be noted that while the simulations presented in Fig. 2.3 are initialized using NARR

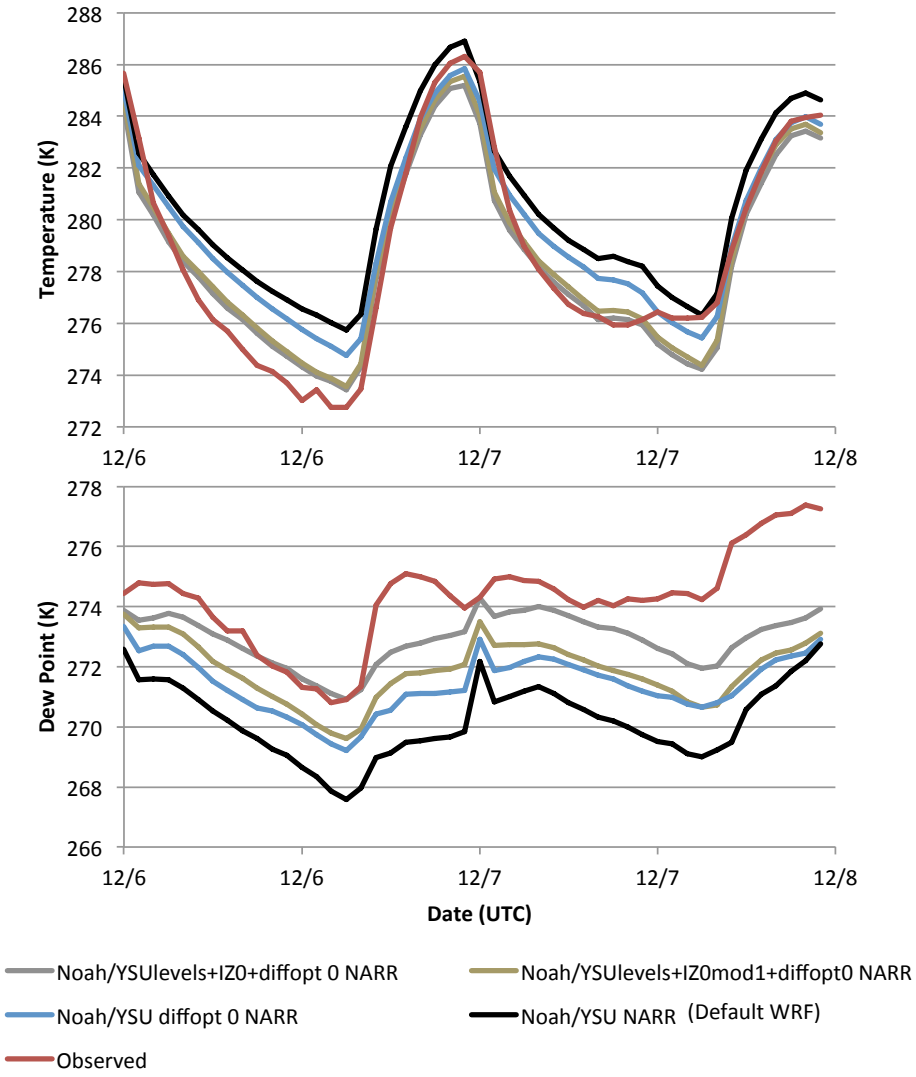

Figure 2.2: Observed and simulated temperatures (at top) and dew points (bottom) from December 6-8 for the CV subset.

soils, these results are independent of the initialization.

It was hypothesized that the increase in dew points seen throughout the Central Valley was a direct result of the increased evaporation in the surrounding terrain. In order to test this, a modified version of the IZ0TLND option, called IZ0mod1, was created which activated IZ0TLND everywhere except landuse 11-14 (the forested terrain that surrounds the CV). If the enhanced evaporation in forested regions is indeed important, it will be reflected in the Central Valley dew points.

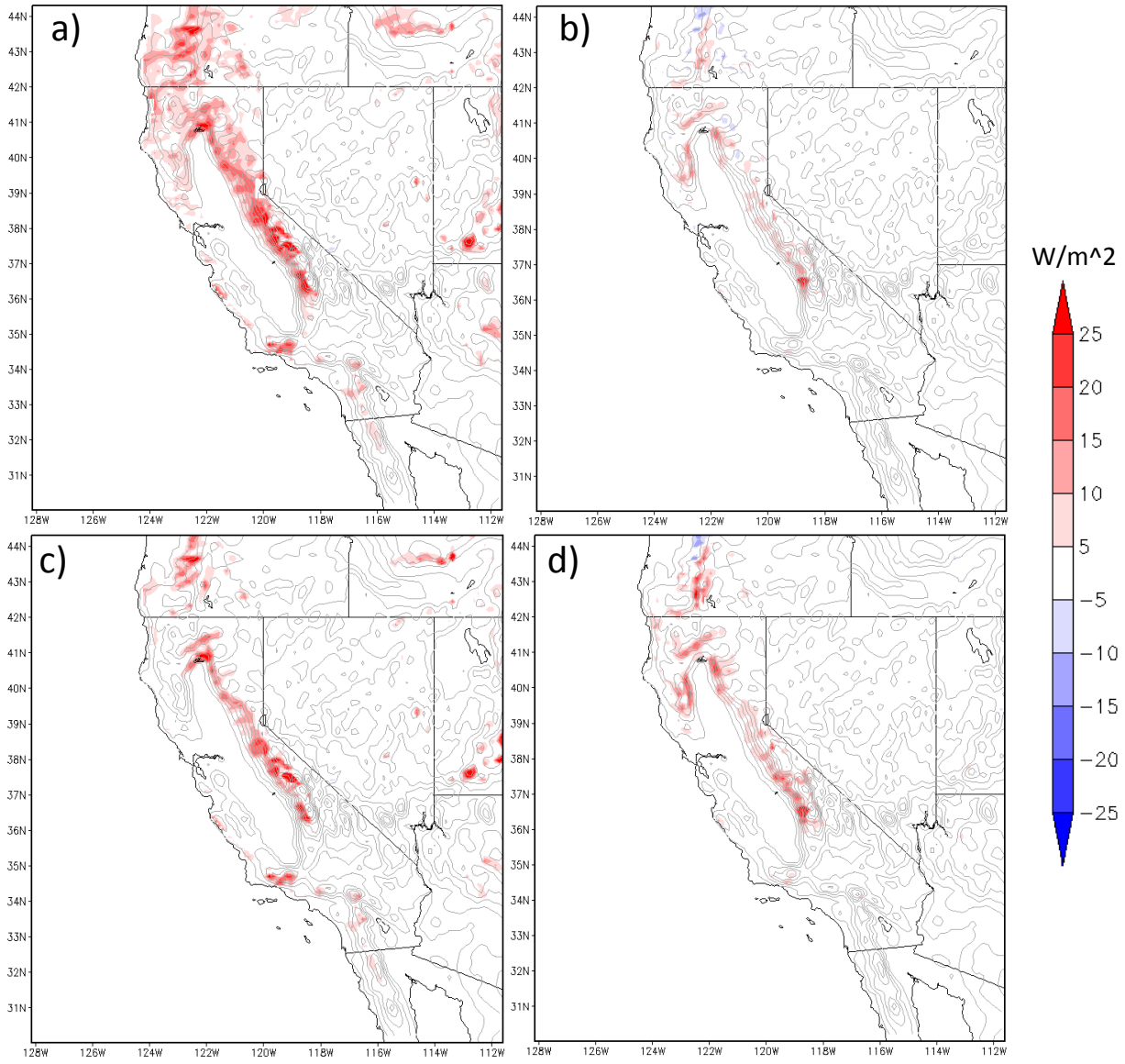

Figure 2.3: The average latent heat flux (W/m^2) difference (shaded) from December 6-8 for the Noah/YSU+IZ0+diffopt0 NARR minus Noah/YSU+diffopt0 NARR (a), and Noah/YSUlevels+IZ0+diffopt0 NARR minus Noah/YSU+IZ0+diffopt0 NARR (b). Figures c and d correspond to figures a and b, respectively, but illustrates the difference for only overnight (00Z-12Z) hours. Terrain is contoured every 300 m.

The results from this modification are presented in Fig. 2.2 as Noah/YSUlevels IZ0mod1 diffopt0 NARR. Here, one can see that the dew point from the modified version looks strikingly similar to the member that does not have the IZ0TLND option activated. This

means that the CV dew points are heavily influenced by the increased evaporation from the surrounding forests. For surface temperatures (Fig. 2.2 top), the modified version of the IZ0TLND option resembles the member utilizing all improvements. This means the increase in dew points is a non-local effect while the decrease in temperature is local.

Configuration	Dew point Bias (K)
Default	-4.07
Diffopt0	-2.86
IZ0+Diffopt0	-1.96
Levels+IZ0+Diffopt0	-1.35
Levels+IZ0mod1+Diffopt0	-2.40
Levels+IZ0mod2+Diffopt0	-2.27

Table 2.2: Dew point biases for the CV subset using different WRF configurations during December 6-8. Simulations were initialized with the NARR.

Presented in Table 2.2 is a summary of how each modification changes the dew point in California's CV from December 6-8. Starting from the top, one can see that turning off diffusion decreases the dry bias by about 1.2 K. Now, if one were to activate IZ0TLND (IZ0 + Diffopt0) it would further improve the dry bias to -1.96K, a 0.9K change. However, it is when the levels are shifted (Levels + IZ0 + Diffopt0) do things become interesting. This is because you do not just see the small improvement suggested by Fig. 2.3b, but a rather large (0.61 K) reduction in the dry bias.

In order to explain why such a small increase in the latent heat flux caused by shifted levels (Fig. 2.3b) can bring a large increase to dew points relative to IZ0TLND (Fig. 2.3a), one needs to inspect different hours of the day. Fig. 2.3c,d are subsets of Fig. 2.3a,b, respectively, but restricted to showing the latent heat flux change during the overnight hours only. When viewed this way, the differences between the IZ0TLND option and shifted levels are much smaller. Because of this, it was hypothesized that not only was evaporation from landuse 14 – the evergreen needleleaf forest – making a difference, but more specifically, the *nighttime*

evaporation had the largest influence.

To test this theory, another modified version (IZ0mod2) of IZ0TLND was created that was activated everywhere except landuse 14 at nighttime (00Z-12Z). This means the evaporation enhancement in landuse 14 is restricted to daylight hours only, while at night the original formulation was employed. This version is compared to mod1 (Table 2.2) which had IZ0TLND implemented everywhere but landuse 14. Here, one can observe that by allowing more evaporation during the daytime but not at night, the dry dew point bias was reduced by a mere 0.13K to -2.27K. If the daytime evaporation made the difference, one would expect to see a dew point bias of -1.35K (Levels + IZ0 + Diffopt0) or of similar magnitude.

By shifting the lowest model levels down, the evaporation in the surrounding terrain increases, albeit, mostly at night. This helps drainage flows become more moist and subsequently mitigate the Central Valley dew point bias. However, why is evaporation sensitive to the height of the lowest model level in the first place? And why is it favored during the overnight hours? These are important questions that will be discussed in depth in Sec. 2.3. For now, one should appreciate the sensitivity to vertical resolution.

While evaporation has increased in online[2] simulations due to IZ0TLND and shifted levels, it is important to see how this compares to the more controlled offline runs. To demonstrate the consistency between each, Fig. 2.4 shows the average latent heat flux difference at 12Z from December 4-16 between the online (Noah/YSUlevel+IZ0+diffopt0 NARR) and offline (HRLDAS with IZ0 activated) simulations. Here, cooler colors represent less evaporation from the online simulation while warmer colors represent more. One can observe that the majority of places surrounding the CV have too little evaporation relative to the offline model. This means that every time the model is reinitialized, soils in areas shaded in blue end up losing water that should have evaporated into the atmosphere during the previous run. Of course, the offline model is not necessarily correct, but it is concerning to see such large inconsistencies between the online/offline simulations.

The results presented in Fig. 2.4 are an average at 12Z because the nighttime evaporation

[2]Here, online refers to the fully coupled land surface and atmospheric model.

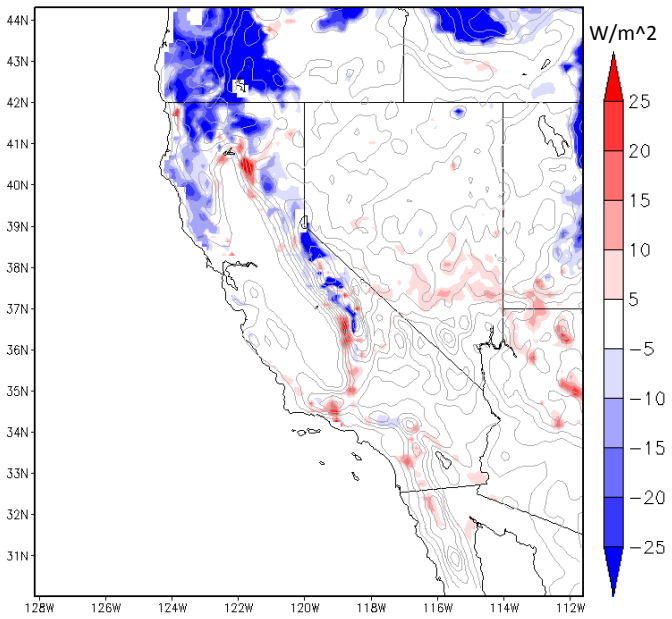

Figure 2.4: The average latent heat flux difference between the Noah/YSUlevels + IZ0 + diffopt0 NARR and offline HRLDAS (with IZ0TLND activated) at 12Z from December 4-16.

was found to be of large importance. However, if one inspects the 24 hour average, not much difference is observed (not shown). Additionally, this figure compares the NARR to the HRLDAS; this was done because the NARR had the largest overnight evaporation rates in landuse 14 owing to its high soil moisture content in the area. This means the ERA, NAM, and spun soils underestimated the evaporation rates even more.

When the IZ0TLND option is activated in the WRF model one should technically re-spin the soils offline to account for the changes in the exchange coefficient. However, this has been deemed not necessary and can be explained with the following example. Two simulations were made using the same physics (Noah/YSUlevels IZ0 diffopt0) but with different soil initializations. Both of these soils were spun offline using the HRLDAS but one activated the IZ0TLND option. Because IZ0TLND was activated offline, the December 6-8 dew point bias shifted by only 0.23 K in the full domain and 0.17 K in the CV subset. Certainly, this difference is trivial for our application and is why the IZ0TLND option has been activated online without re-spinning the soils offline.

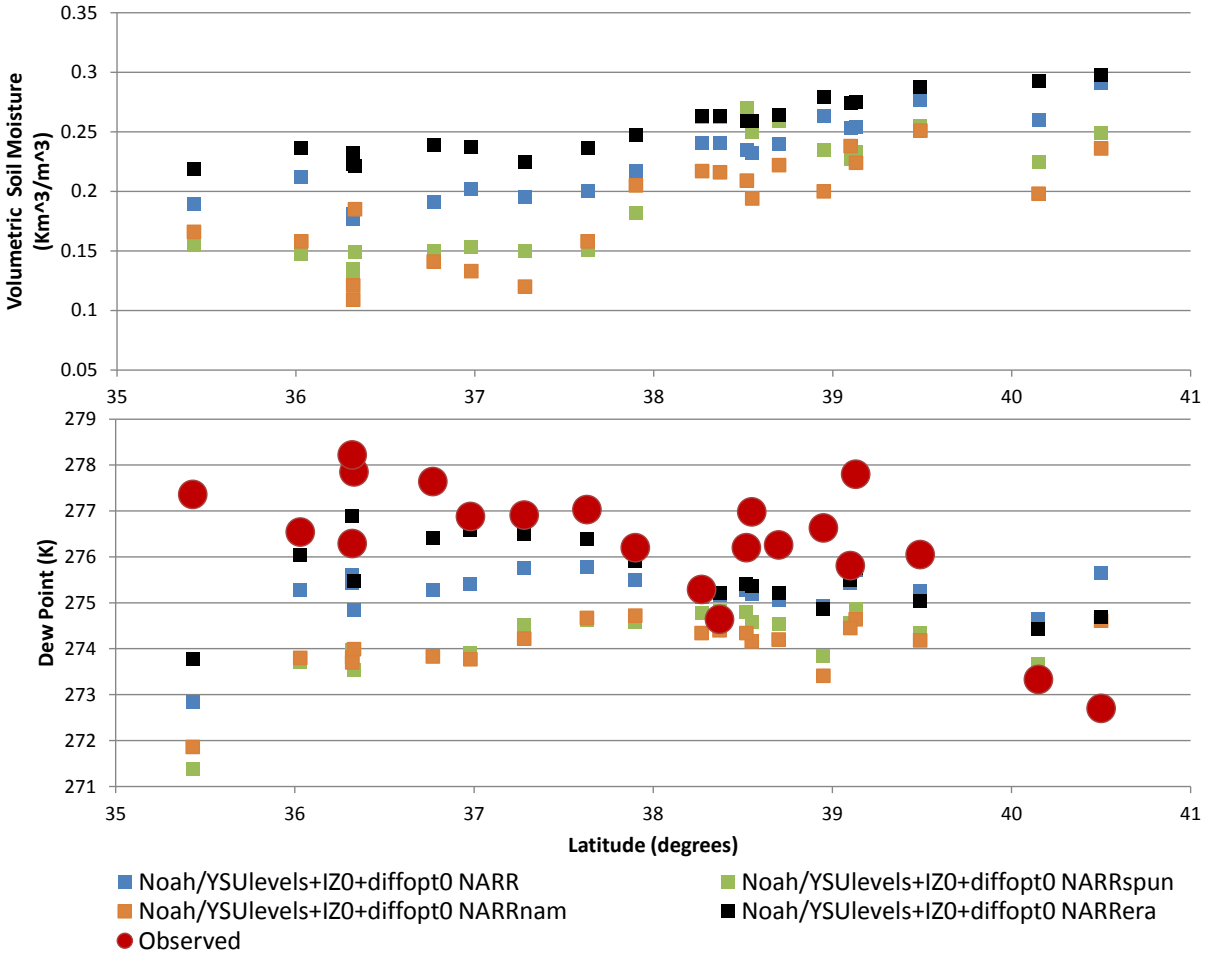

Figure 2.5: Average dew points (bottom) and soil moisture values (top) from December 4-16 for the 21 surface stations in the Central Valley shown by latitude.

The different soil initializations used in this chapter have a dramatic range in moisture values, unfortunately. This is illustrated in Fig. 2.5 (top) which shows the average modeled soil moisture from December 4-16 for the 21 surface stations in the Central Valley by latitude. Here, one can observe that the NAM initialized soils (NARRnam) are nearly identical to those spun offline in the HRLDAS. The previously discussed dry bias is certainly evident (Fig. 2.5 bottom) and is maximized in the San Joaquin Valley. Of course, the bias would be much worse (Fig. 2.2) if the cold pool configurations were not utilized.

Even higher moisture content can be seen in the NARR initialized soils. Consequently, the average dew points are also higher, although still too dry. This is the case for all

locations except the two northern most stations (KRDD & KRBL) where simulations had trouble mixing out a shallow moist layer. At KRDD and KRBL, modeled dew points were similar to the rest of the valley, although, observations show that they are on average, drier.

Finally, the simulations initialized with ERA-Interim soils provide even more soil moisture for the San Joaquin Valley while values in the Sacramento Valley are comparable to the other datasets. As expected, this increases San Joaquin Valley dew points while the low level moisture in the Sacramento Valley remains relatively unchanged. It is interesting to note that with the ERA soil initialization the bias between the two valleys is roughly the same magnitude (-1.1K) and does not increase (in the negative sense) with decreasing latitude. This latitude bias is most apparent with the NAM and HRLDAS initialization.

Because the ERA-Interim soils have the highest water content, they also have the highest latent heat flux in the online simulations. In order to judge whether these larger fluxes are within reason, we can compare modeled fluxes to the Vaira and Tonzi Ranch AmeriFlux sites located south and east of Sacramento. This is shown in Fig. 2.6 (bottom) for December 4-15. Notice that both Tonzi and Vaira Ranch are represented by the same model grid point, owing to their close proximity.

Here, one can observe that the two observations do not agree necessarily well for afternoon values, with Vaira Ranch having larger evaporation rates. Nevertheless, the simulations initialized with ERA-Interim appear to lie between the observations on most days. Finally, one can observe that shifting the levels and activating IZ0TLND hardly affects the latent heat flux (except late on the 8th) in the CV. This is consistent with Fig. 2.3.

As shown earlier, this option has the most dramatic impact on forested regions and is again demonstrated in Fig. 2.6 (top). Here, the simulation with shifted levels and IZ0TLND produces larger fluxes throughout the majority of the day. When compared to observations it does appear that these values are too large, although both simulations overestimate observed values during the December 4-8 time period. Focusing on the later half of the period (Dec. 9-15), there appears to be more agreement with observations; however, shifted levels and IZ0TLND still slightly over predicts evaporation on most days.

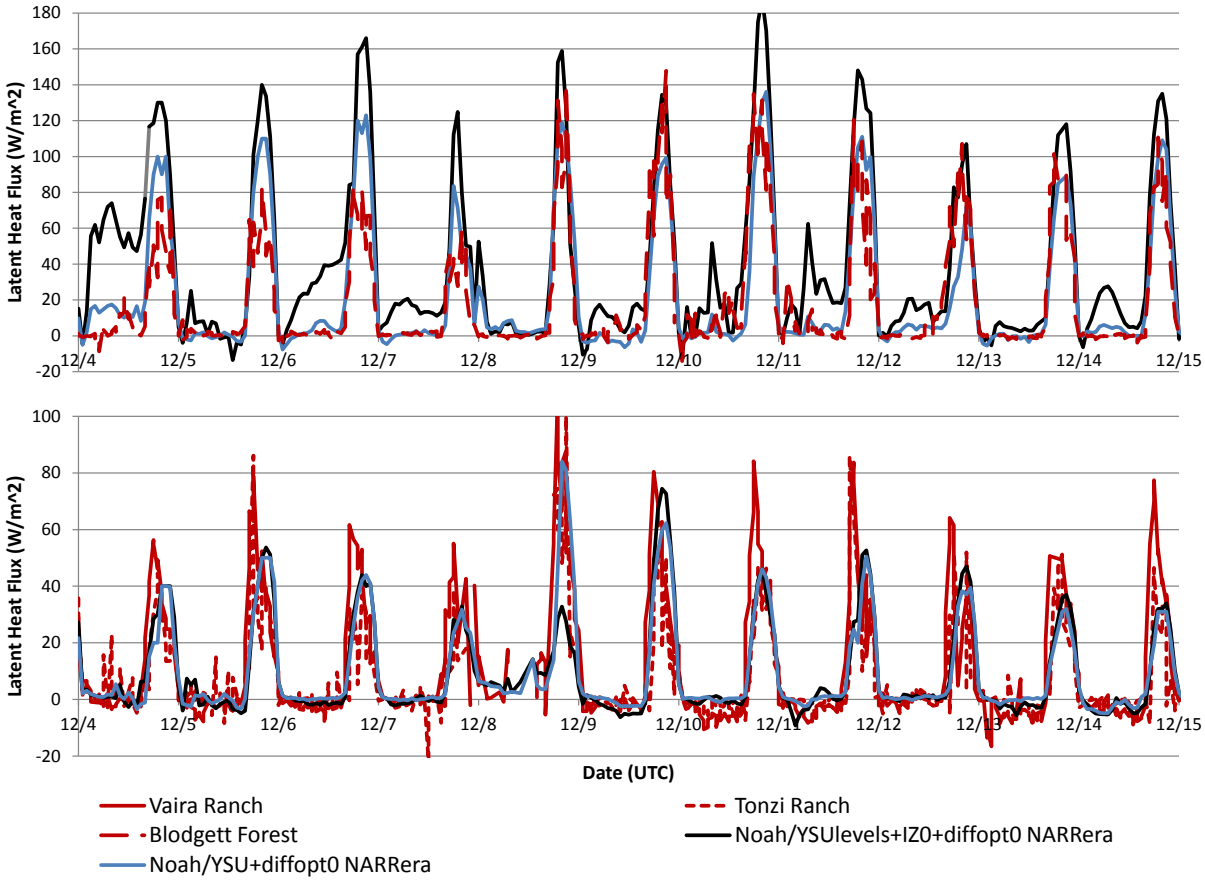

Figure 2.6: Observed and modeled latent heat fluxes from December 4-15 for three AmeriFlux sites. Vaira and Tonzi Ranch (bottom) are located on the eastern edge of the CV and are approximately 3 km apart. The Blodgett Forest site (top) is located farther east in the Sierra Nevada mountain range and is in the evergreen needleleaf forest.

One should keep in mind that the Blodgett Forest is the only AmeriFlux site surrounding the CV with publicly available data. Because of this, nothing can be concluded, although, these disagreements should be noted. Additionally, one can observe somewhat large variations just between the closely sited Vaira and Tonzi Ranch flux sites (Fig. 2.6 bottom). This demonstrates that large spatial variations and/or difficulties in estimating fluxes can arise.

To get a better understanding as to whether or not this increased evaporation is in fact realistic, the average dew points for each station is shown for the Noah/YSU+diffopt0 NARRera (Fig. 2.7a,c) and Noah/YSUlevels+IZ0+diffopt0 NARRera (Fig. 2.7b,d). Here,

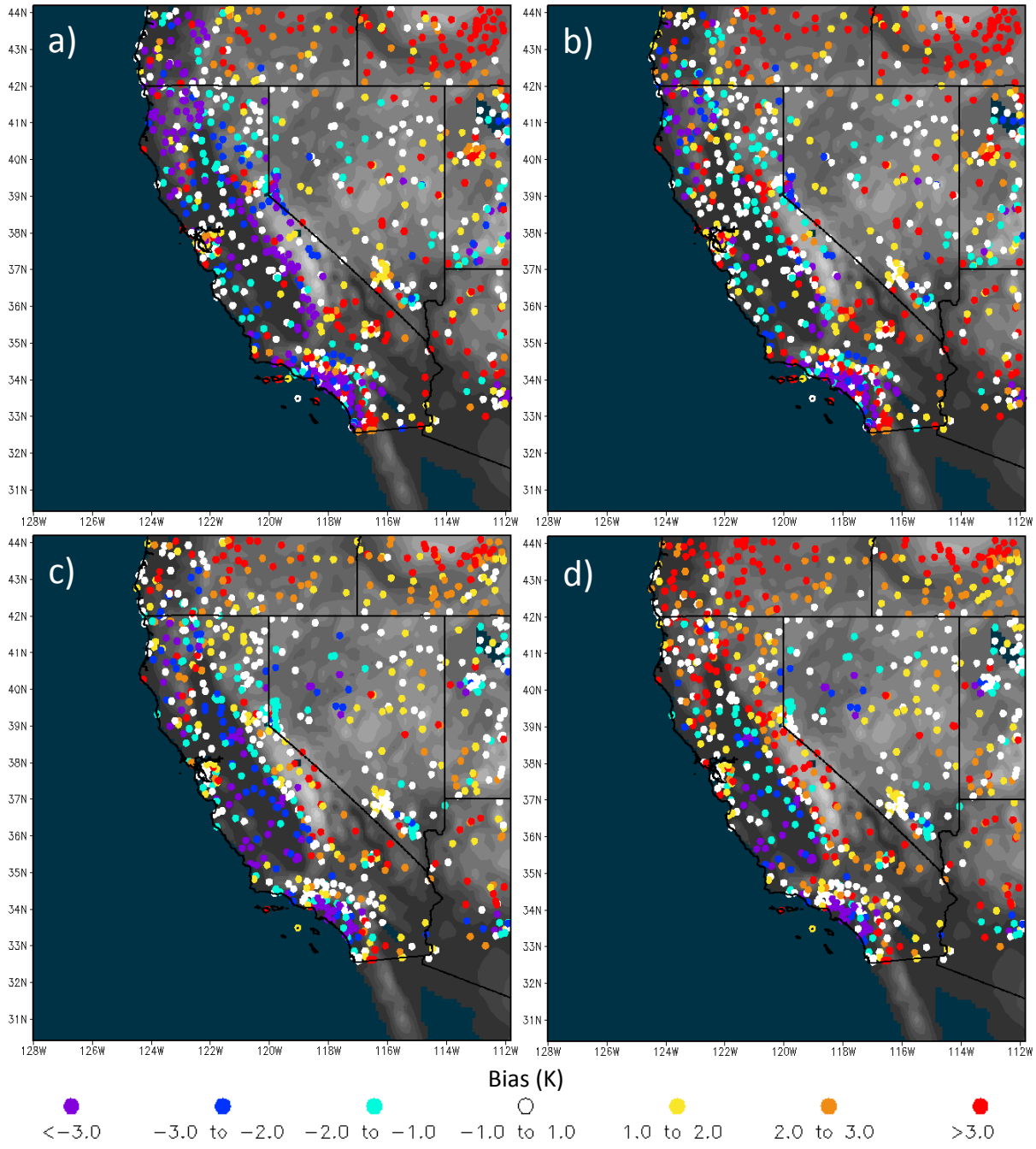

Figure 2.7: Dew point bias (K) by station is shown for the Noah/YSU+diffopt0 NARRera (a,c) and Noah/YSUlevels+IZ0+diffopt0 NARRera (b,d) averaged over December 4-16, 2005 at 14 UTC (a,b) and 22 UTC (c,d). Both RAWS and ASOS stations (reporting at least 10 of the 12 days) are shown for this figure only.

Fig. 2.7a,b shows the nighttime (14 UTC) average (December 4-16, 2005) dew points for both ASOS and Remote Automatic Weather Stations (RAWS) networks to increase observation density (Fig. 1.2). In this figure one can observe the overnight dry bias for the Noah/YSU+diffopt0 NARRera (Fig. 2.7a) is prevalent not only in the CV, but also the surrounding terrain. This is in contrast to the Noah/YSUlevels+IZ0+diffopt0 NARRera (Fig. 2.7b) which has little bias across the CV and surrounding terrain. This suggests that the inflated evaporation rates may be more realistic.

However, this point is contradicted by looking at the daytime (22 UTC) dew point bias (Fig. 2.7c,d). One can observed that the terrain surrounding the CV is nearly unbiased for the Noah/YSU+diffopt0 NARRera (Fig. 2.7c) while the Noah/YSUlevels+IZ0+diffopt0 NARRera (Fig. 2.7d) has a strong warm bias. This could indicate that the daytime evaporation rates are unrealistically large in the simulations using all improvements. However, as previously shown, the nighttime evaporation rates are what truly matter for CV dew points and again, evidence is lacking as to weather or not the inflated evaporation rates are indeed realistic.

A final look at the observed and modeled relative humidity in the CV is presented in Fig. 2.8 for December 4-16. Here, the default WRF using ERA soils (Noah/YSU NARRera) is compared to simulations using all cold pool configurations, also with ERA soils (Noah/YSUlevels + IZ0 + diffopt0 NARRera). One can see that on almost all nights, the prevalent dry bias is completely removed. It is important to note that on nights such as the 13th and 14th, where the modeled relative humidity from the default WRF is relatively close to reality, cold pool configurations do not overpredict the low level moisture.

Since the degradation of simulations using diffusion is non trivial and its implementation unphysical, all real data experiments in following chapters, unless otherwise noted, will be made without horizontal diffusion. Additionally, because the enhanced evaporation brought about by shifted levels and IZ0TLND could not be properly verified in forested regions, these options will not be used in additional experiments (unless otherwise noted).

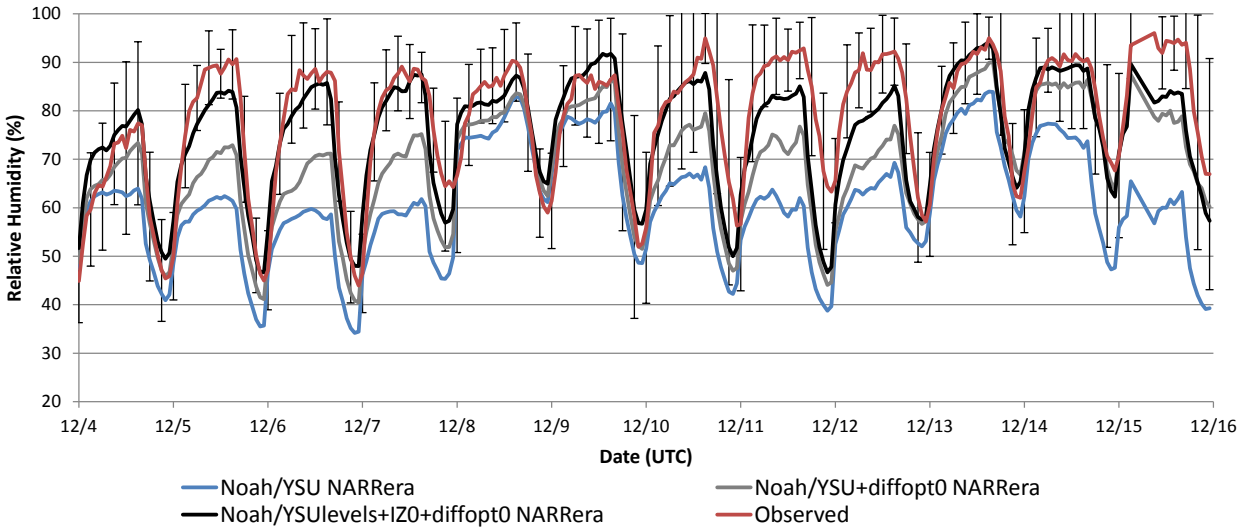

Figure 2.8: Observed and modeled relative humidity for the CV subset from December 4-16, 2005. Error bars depict plus or minus one standard deviation for observed RH every third hour.

2.3 Drainage Flows

Drainage flows are most certainly influential to the evolution and life cycle of cold pools. In order to fully appreciate their influence and dependence on horizontal and vertical resolution, 2D idealized simulations are made. Using a 168 km wide domain (Fig. 2.9), 1 km mountains located at either end slope down to the valley floor (0 km) over a horizontal distance of 36 km. Slopes of this magnitude are commonly seen around the Central Valley while the 96 km model basin approaches the maximum observed width. This setup will demonstrate the influence of drainage flows even at the widest locations of California's Central Valley.

To initialize the idealized WRF model, a typical wintertime sounding was obtained and forced to dry adiabatic in the lowest kilometer. This was done in order to maximize drainage flows along the entire slope. Additionally, model integrations start at sunset (00 UTC) to avoid complications with the convective boundary layer and all initial flow was removed. To further simplify the problem, the microphysics scheme was deactivated and the Thermal-Diffusion (TD) LSM was utilized with a soil moisture and thermal inertia of 10% and

1.2552E5 J m^{-2} K^{-1} $s^{-0.5}$, respectively. However, an additional experiment utilizing soil moisture values of 50% will be discussed towards the end of this section.

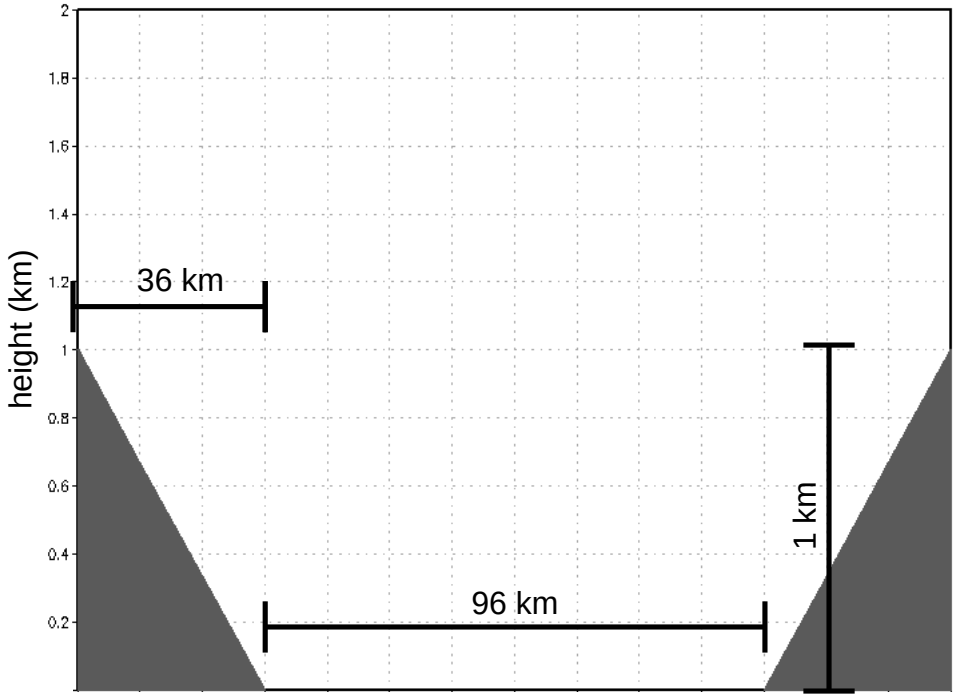

Figure 2.9: The idealized domain includes 1 km tall mountains (gray shading) sloping down to the valley floor (0 km) over a horizontal distance of 36 km. Simulations employ a valley width of 96 km unless otherwise noted.

As previously mentioned, the nighttime evaporation in the terrain surrounding the Central Valley is heavily influenced by the height of the lowest sigma level. To understand why this might be, Fig. 2.10a shows the along slope 10 m wind speeds averaged over the middle third of the slope for various vertical resolutions. Here, one can observe that the default WRF levels (nz51) produce drainage flows around 2 m/s while the 'levels' experiment has winds that are roughly 1 m/s stronger.

Interestingly, the impact of horizontal resolution on drainage flows is rather insignificant. This is demonstrated in Fig. 2.10b which shows the along slope 10 m wind for various horizontal but constant vertical resolutions. As one can observe, virtually no difference is seen between simulations suggesting that the horizontal temperature gradients which drive

the downslope winds are similar for each case.

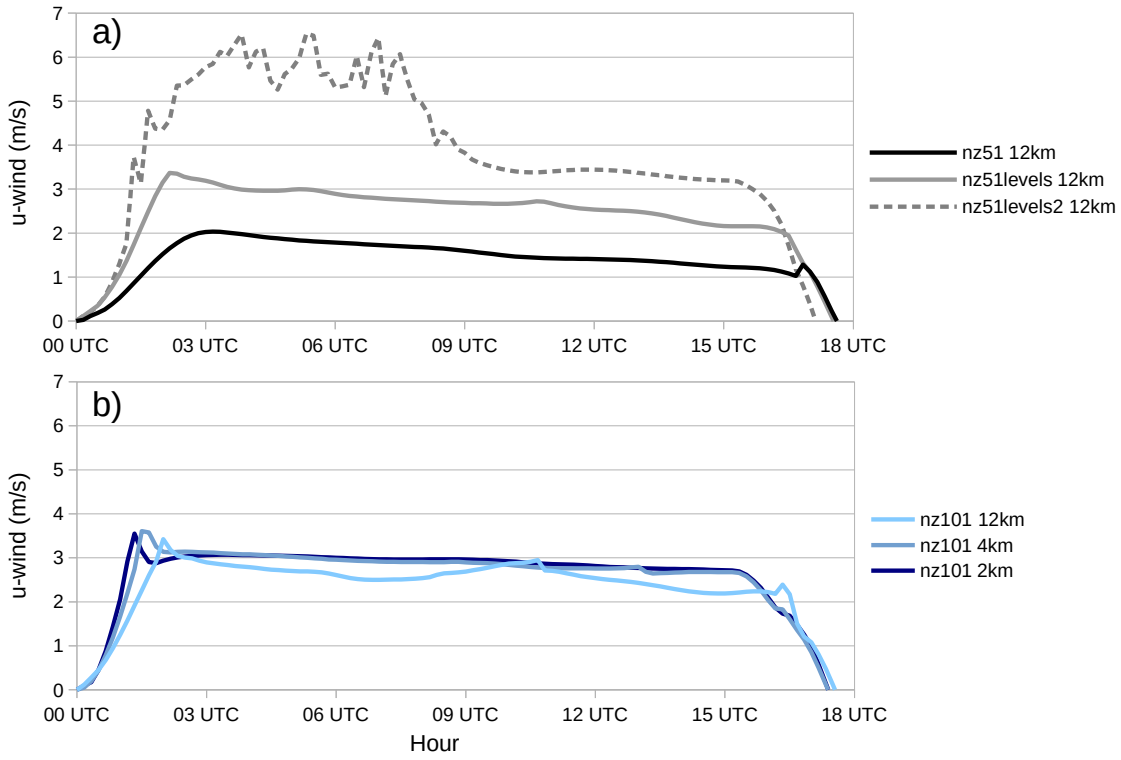

Figure 2.10: The along slope 10 m wind speeds averaged over the middle third of the mountain slope for various vertical (a) but constant (12 km) horizontal resolutions. Panel b depicts the changes from various horizontal resolutions while using a constant number of vertical levels (101).

Turning back to Fig. 2.10a, shifting the height of the lowest sigma level down even further (to 0.999, see Tb. 2.3) results in another increase in 10 m wind speeds (levels2). This time, the change is much more pronounced with gust-like oscillations reaching 6 m/s. However, Fig. 2.10a is actually quite deceiving since the *resolved* model winds for the 'levels2' experiment never approach 6 m/s near the surface, nor anywhere in the atmosphere. In fact, resolved winds only reach 3 m/s at this location. Although, since the first model level is approximately 3.3 m above the surface and the 10 m wind is diagnosed from this level, a higher value is achieved.

Surprisingly, other than the diagnostics shown in Fig. 2.10a, the average drainage flows

over the domain do not differ all that much between vertical resolution tests. This is demonstrated in Fig. 2.11 which shows the average (forecast hour 0-15) difference in the resolve u-wind for the 'levels2' and default experiment. As one can see, the resolved along slope drainage flows do not favor a particular resolution test. In fact, changing the height of the lowest sigma level may result in both a stronger and weaker along slope wind, depending on the location. In the valley the 'levels2' experiment clearly has a slightly stronger surface flow in addition to a marginally faster return flow. Since the stronger along slope wind speeds in Fig. 2.10a are not observed in Fig. 2.11, this suggests that changes are happening in the surface layer (where the 10 m wind is computed).

Default	0.993	0.983	0.970	0.954	0.934	0.909	nz=51
levels	0.997	0.986	0.972	0.955	0.935	0.909	nz=51
levels2	0.999	0.990	0.972	0.955	0.935	0.909	nz=51
nz101	0.9977	0.9954	0.993	0.991	0.988	0.986	nz=101

Table 2.3: The first 6 sigma levels used in idealized simulations with the total number of model levels (nz) listed in the rightmost column.

It is worth noting that Shin et al. (2012) has performed experiments that vary the height of the lowest model level. Just as with our results, it was found that the 10 m winds in the stable boundary layer increased with decreasing model level height. They attributed the increased wind speeds to the stability function within the surface layer. It was shown that as the lowest model level decreased, the resolved shear increased, which subsequently lowered the Richardson number (Ri). This acted to change the surface layer regime from 'stable' ($\text{Ri} \geq 0.2$), to 'damped mechanical turbulence' ($0 < \text{Ri} < 0.2$) which changed the stability function and diagnosed 10 m winds.

Further inspecting the simulations found in this section, one will notice that the default experiment employs the 'stable' regime for almost all locations and times (Fig. 2.12 left). This is in contrast with the 'levels2' experiment (Fig. 2.12 right) which has the 'damped mechanical turbulence' regime active for a large portion of the surrounding slopes. Here,

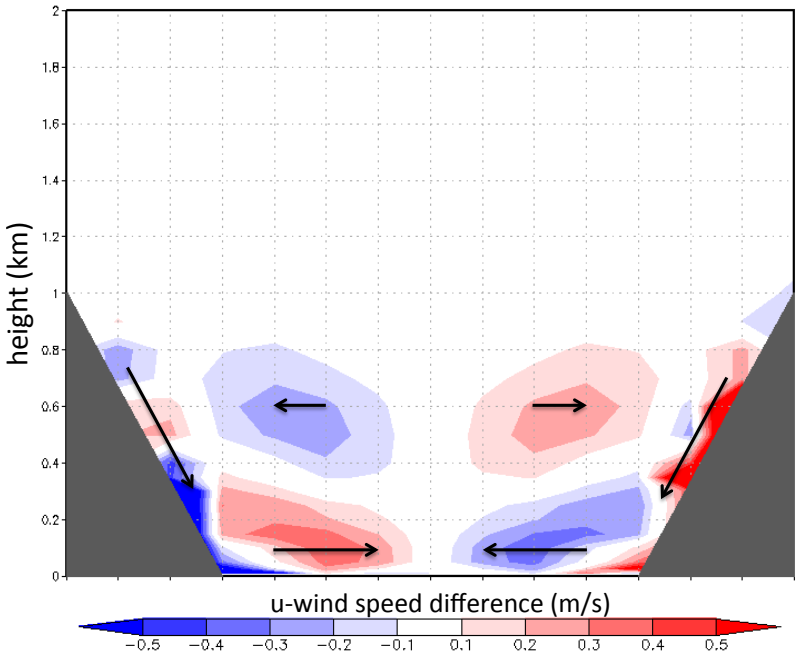

Figure 2.11: Average (forecast hour 0-15) u-wind difference between the 12 km horizontal resolution 'levels2' and default experiments. Arrows indicate the general flow direction.

the first model level is much thinner and the resolved drainage flows are closer to the earth's surface. This acts to increase the resolved shear, decrease the Richardson number, change the regime, and finally alter the stability function.

As one could imagine, the change to a less stable regime (by shifted levels) acts to enhance evaporation (and all surface fluxes) along the slopes. Fig. 2.13c demonstrates this by showing the dew point difference between the 'levels2' experiment and the default vertical grid. As previously mentioned, the enhanced evaporation is also seen in our real data simulations. In fact, additional tests reveal (not shown) that the increase in CV moisture done by the shifted levels is entirely absent if the 'damped mechanical turbulence' regime is ignored. This confirms that shifted levels act only to change the surface layer regime and increase the surface fluxes in both idealized and real data cases.

While the higher along slope dew points via shifted levels seen in Fig. 2.13c are congruent with real data cases, the lower values near the valley center are not. An explanation for this is quite simple. To begin, one should inspect Fig. 2.14a which shows the total dew point

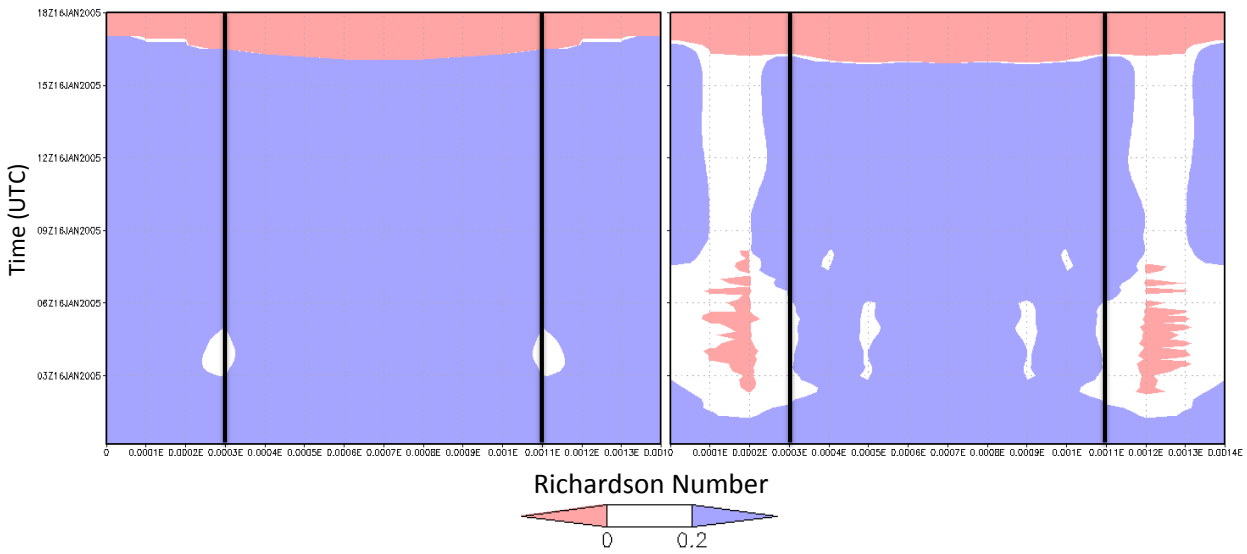

Figure 2.12: Hovmöller diagrams for the Richardson number is shown for the 12 km horizontal resolution default (left) and 'levels2' (right) experiments. The x-axis spans the width of the domain and has vertical black bars to indicate the edges of the valley.

difference between the 'levels2' experiment with and without terrain. It can clearly be observed that drainage flows, in this situation, act to decrease moisture near the valley floor. One should note that the drying is maximized near the edge of the valley floor and is less important as one moves towards the center. Now, how far this dry tongue protrudes into the valley (Fig. 2.14a) is directly influenced by the speed of the drainage flows. While they do not differ much between the experiments, the 'levels2' simulations have drainage flows at the valley bottom that are roughly 0.35 m/s faster than the default grid (Fig. 2.11). This may not seem like much, however, drainage flows are only around 1 m/s at the valley bottom and over 15 hours, the 0.35 m/s change can account for the differences seen in Fig. 2.13c. This is why the 'levels' (Fig. 2.13a) and 'levels2' (Fig. 2.13c) experiments appear to have relatively lower dew points toward the valley center when compared to the original vertical grid. However, it was hypothesized that if these idealized simulations ran for multiple nights and were allowed to come into equilibrium, the relative dry bias in the valley center (Fig. 2.13a,c) would not exist. This was tested and is indeed the case.

Looking at temperatures, one can observe that differences between the 'levels2' experi-

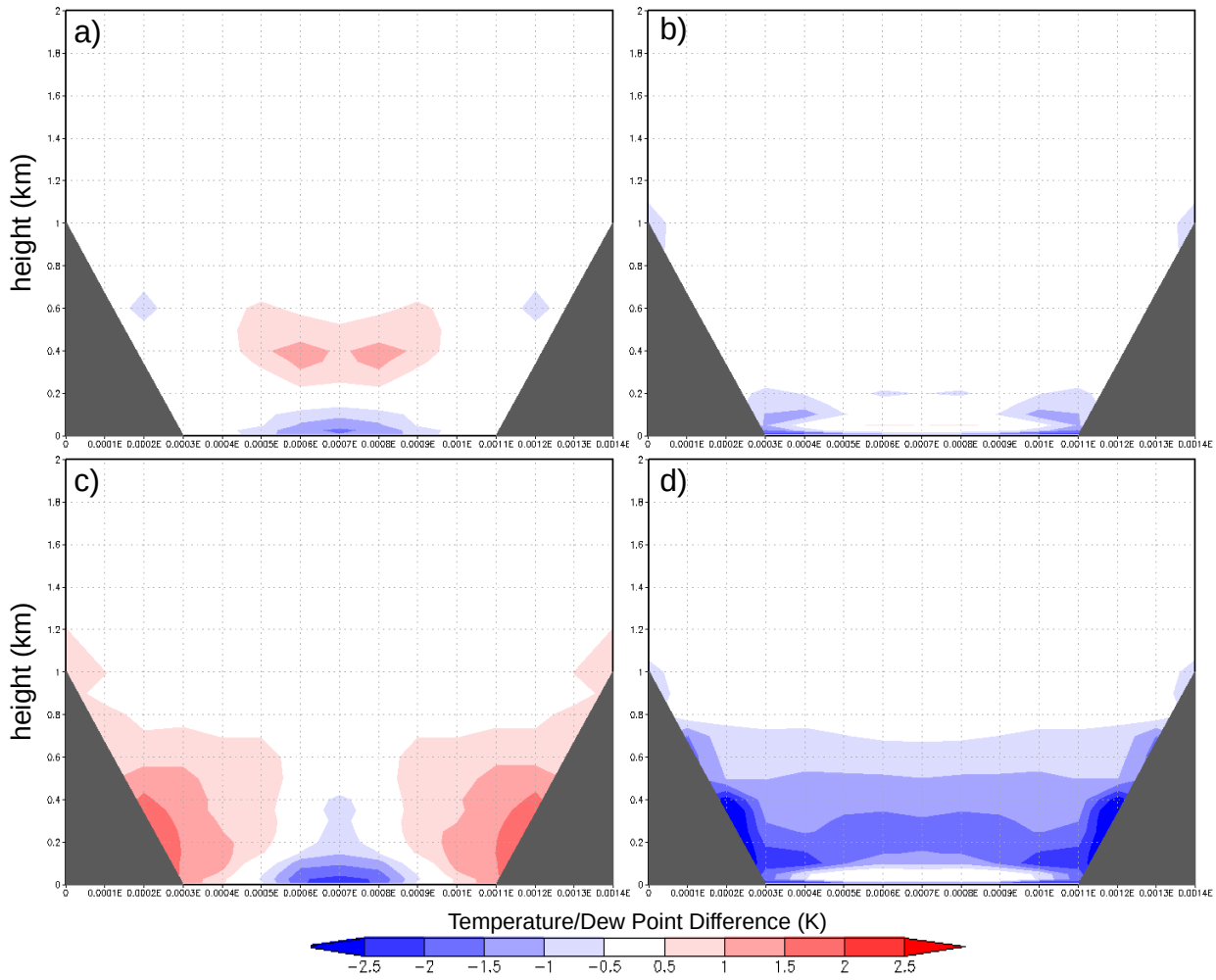

Figure 2.13: Dew point (a,c) and temperature (b,d) differences between the 12 km horizontal resolution simulations using 'levels' and default levels (a,b) at forecast hour 15. Differences between the 'levels2' and default levels experiments are shown in panels c and d.

ment and the default grid is anything but negligible (Fig. 2.13d). Here, temperatures above the valley floor are on the order of 1.5-2 K cooler with even higher values near the sidewalls. Again, this is related to the change in the stability function which increases (in the negative sense) the sensible heat flux and ultimately cools the atmosphere. This difference is also evident in the 'levels' experiment but of much smaller magnitude (Fig. 2.13b). Finally, one should take note that shifting the levels relative to the default grid changes temperatures by less than 0.5 K between the surface and 0.1 km.

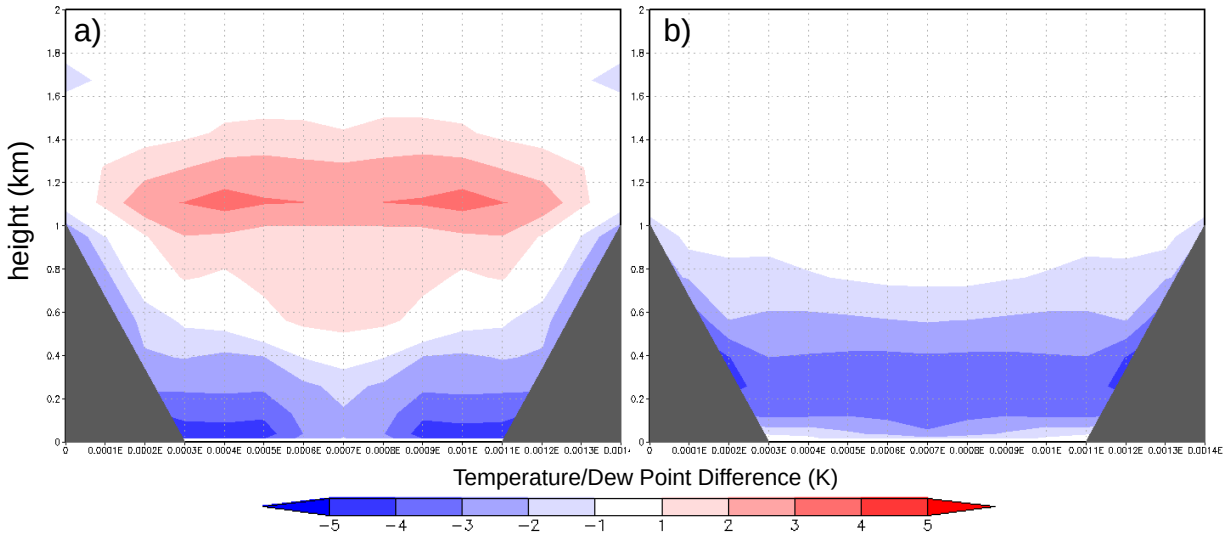

Figure 2.14: Dew point (a) and temperature (b) differences for the 12 km levels2 experiment with and without mountains at forecast hour 15. Terrain is shaded in gray for reference.

Turning back to the total dew point difference (mountain vs flat terrain) for the 'levels2' experiment (Fig. 2.14a), one will notice that while conditions are drier near the surface, they are actually more moist aloft. The reasoning here is due to the fact that the drainage flows undercut the preexisting valley air and lift it vertically. Furthermore, since the dew points decrease with height, vertical motions act to increase moisture aloft. As for temperatures, differences caused by terrain (Fig. 2.14b) approach -3 to -4 K in magnitude. This cooling is centered above and below the dew point dry and moist maximums, respectively, and is located roughly 0.1 to 0.4 km above the valley floor.

Up to this point, all simulations have been initialized with a 10% soil moisture content. Rerunning these cases with higher values can impact the overall drying/cooling that is observed. This is demonstrated in Fig. 2.15 which is identical to 2.14 but with 50% soil moisture. Unsurprisingly, the drying created from drainage flows is much less than what occurred with the 10% soil moisture case. Furthermore, the temperatures appear to be, on average, 1 K cooler. This is due to the fact that a higher latent heat flux causes a cooler surface. This cooler surface creates a larger temperature gradient between the ground and first sigma level which increases (in the negative sense) the sensible heat flux and decreases

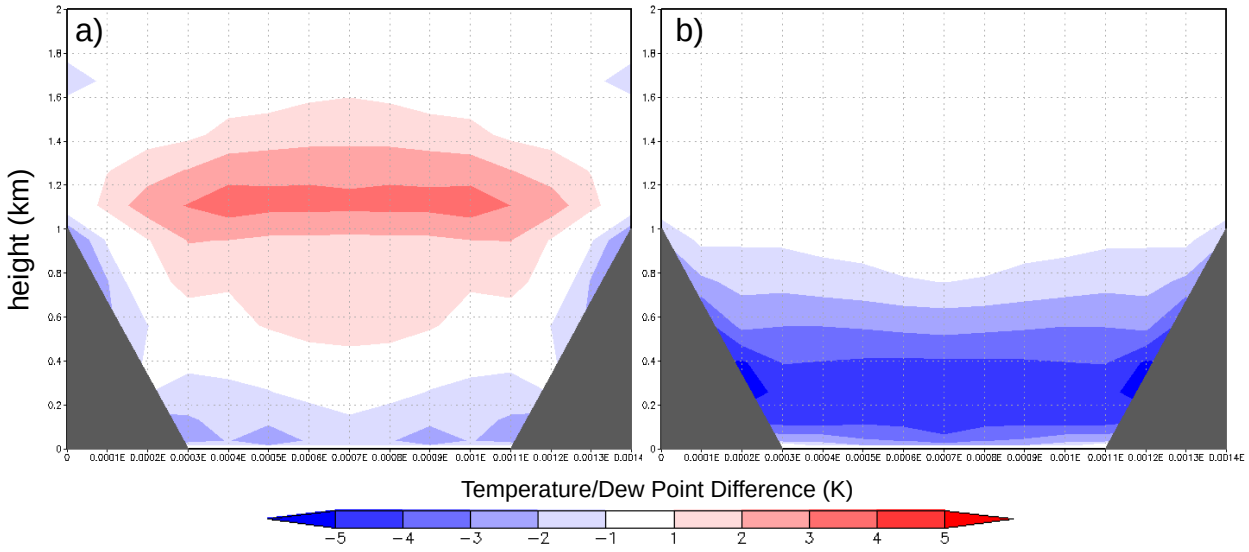

Figure 2.15: Same as Fig. 2.14 but with 50% soil moisture.

the temperature of the drainage flows.

As mentioned in Sec. 1.2.1, it is important to discuss drainage flows and how they modify surface temperatures in valleys. Through a thought experiment it was concluded that the cooling above the valley floor was a direct result of drainage flows, while on the other hand, additional cooling that occurred at the surface happened through indirect effects (i.e. a reduction in downward long wave radiation). In order to investigate this further the surface cooling rates, expressed as the net radiation normalized by the density and specific heat of air at constant pressure, are shown for the 'levels2' experiment (black line) 1 minute after initialization for the valley and surrounding terrain.

Here, the contribution of net radiation to the surface energy balance determines the *potential* cooling. As one can observe, cooling is on the order of -0.07 K m/s, or if normalized over a depth of 1 m, -0.07 K/s. On closer inspection, it can be seen that the surrounding terrain actually has cooling rates that are slightly larger than the valley. Given the dry adiabatic initialization, this sets up the possibility for drainage flows to be superadiabatic and cool the valley bottom directly rather than indirectly. Before we get to whether or not this is the case, an additional experiment was made in which all moisture was removed

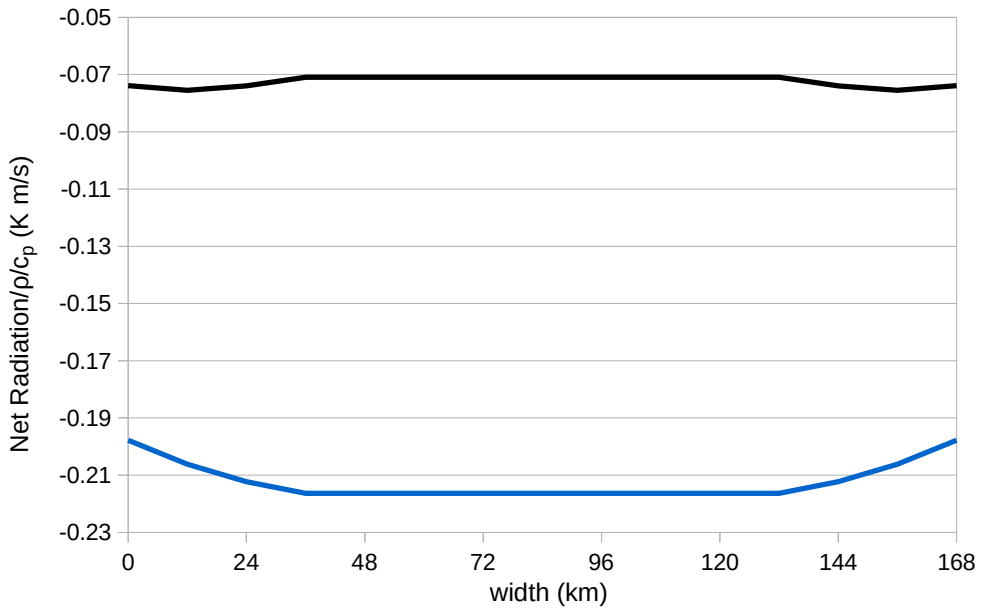

Figure 2.16: Surface cooling rates (K m/s) verses model domain are shown for the 12 km 'levels2' experiment (black contour) 1 minute after initialization. Surface cooling is expressed as the net radiation normalized by the density (ρ) and specific heat of air at constant pressure (c_p). A dry sounding experiment, in which all the moisture was removed, is shown in blue.

(Fig. 2.16). In the blue contour, one can first observe that the cooling is much larger in magnitude due to the absence of a powerful greenhouse gas (water vapor). However, what is interesting here is that the cooling gradient is reversed, meaning the valley is cooling faster than the surrounding terrain. This demonstrates that moisture alone can substantially influence the cooling rates between the mountains and valleys in addition to completely reversing the gradient.

To determine whether the 'levels2' cooling rate could produce drainage flows that are superadiabatic, potential temperature on the first sigma coordinate vs model domain is plotted in Fig. 2.17. Here, one can observe that at initialization the along slope potential temperature is identical at all locations. However, 10 minutes beyond this the valley has a cooler potential temperature than the surrounding terrain. As one can observe, this trend continues and amplifies itself over the next hour.

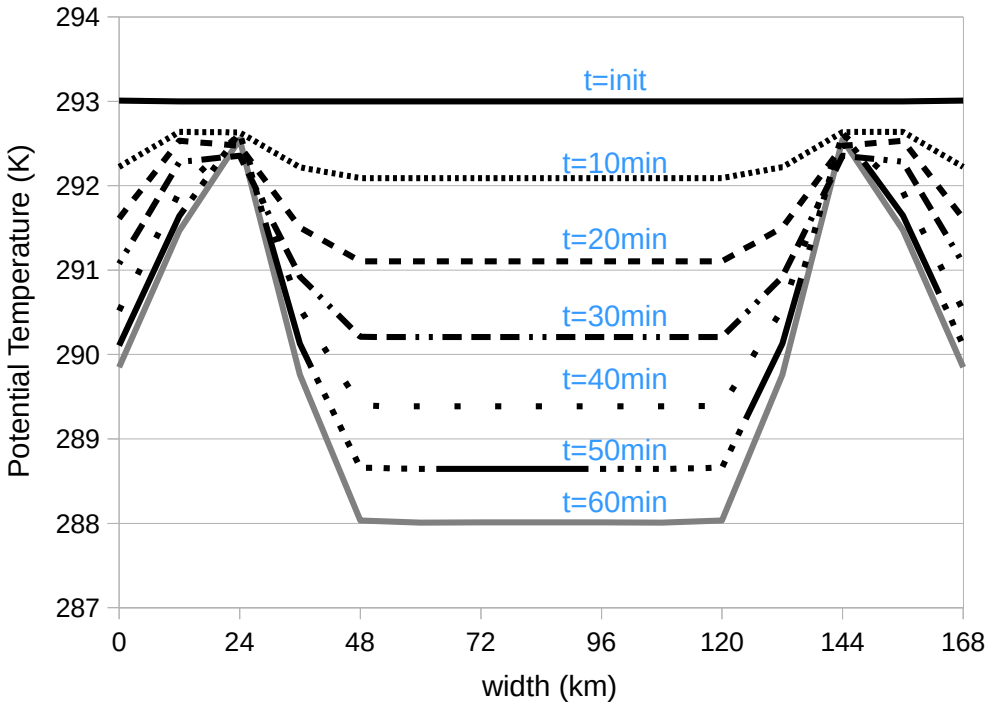

Figure 2.17: Sigma 1 potential temperature verses model domain for the 12 km 'levels2' experiment during the first hour.

This tells us that even in an environment where the along slope cooling is larger, the valley bottom will not be cooled directly. The reason being is that turbulence is generated by drainage flows which subsequently entrains warmer air. It is no coincidence that the temperature maximums in Fig. 2.17 are located two-thirds the way down slope and coincide with, or just downwind of, the strongest drainage flows.

With enough time, air begins to pool above the valley bottom which subsequently reduces the temperature and moisture there. This acts to decrease the downward longwave radiation and enhance surface cooling, further preventing superadiabatic drainage flows. To demonstrate this indirect effect, several experiments were made with various valley widths while keeping the mountain heights/slopes constant. If indirect effects are indeed present, then the surface temperature should become colder as the valley gets smaller. This is exactly the case for the valley center skin (not shown) and 2-m temperatures for both 12 (dotted) and 2 km (solid) horizontal resolution experiments (Fig. 2.18). Furthermore, one can ob-

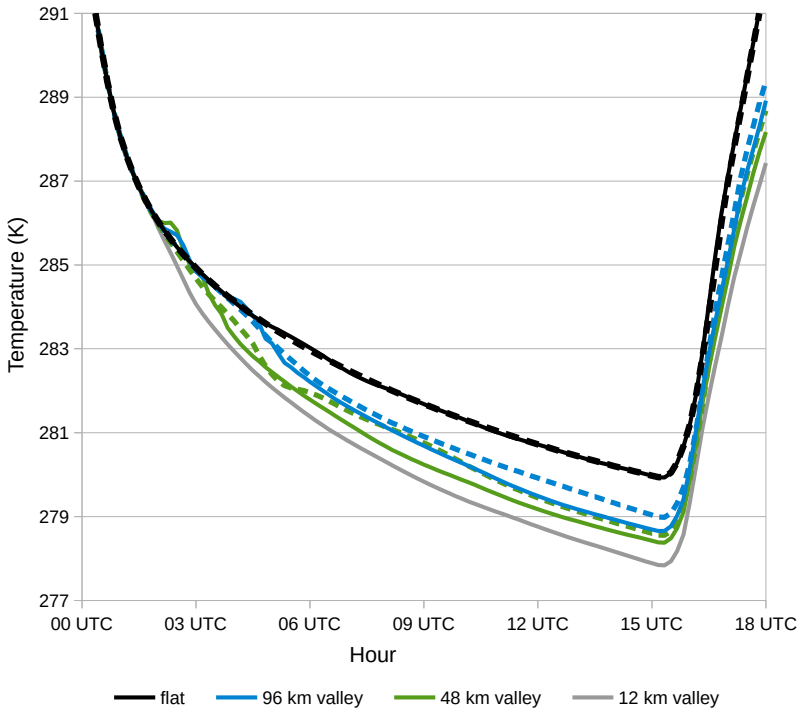

Figure 2.18: The valley center 2-meter temperatures verses time for various valley widths. Solid lines employ a 2 km horizontal resolution while dashed lines have a resolution of 12 km. Simulations use 'levels2' model levels.

serve that the 12 km resolution experiments nearly replicate, albeit slightly warmer, the 2 km experiments demonstrating that there is little dependence on horizontal resolution.

Finally, the differences in surface temperatures are not alarmingly huge (Fig. 2.18). However, further aloft (0.2-0.8 km), the 12 km wide basin temperatures are on the order of 2-5 K colder than the 96 km wide valley (not shown). It was hypothesized that these colder temperatures aloft would limit afternoon warming and give the smaller valley a head start on cooling the following evening. This would allow the subsequent night to be even colder and create an even larger difference in surface temperatures between the wide and narrow valleys. This hypothesis was tested and confirmed all the previous statements; however, the differences were only slightly larger on the second night. Nonetheless, one can appreciate that under certain conditions this multiday cooling effect may be more or less important.

CHAPTER 3

The Influence of Anthropogenic Moisture

While there are many factors to consider when dealing with the evolution and life cycle of cold pools, one area that cannot go overlooked is soil moisture. Shown in the previous chapter, soil moisture from different initializations can yield wildly different values that directly effect surface dew points by several degrees Kelvin (Fig. 2.5). With this in mind, one must consider that the Central Valley of California is largely comprised of irrigated croplands which overwhelmingly influences the soil moisture. Thus, for a complete picture on CV cold pools, irrigation cannot and will not be ignored.

Crops are grown year around in California's Central Valley but the main growing season and subsequent irrigation happens in summer. However, while wintertime irrigation is much less, it is important to understand the impact it plays on wintertime fogs. Since the WRF model does not include irrigation of any sort, an attempt to build a model from the ground up is executed in this chapter. If correctly implemented, one will be able to determine the impacts of irrigation on cold pools.

While the focus thus far has been exclusively in winter, owing to the fact that it is the period in which cold pools are most prevalent, the analysis will be extended into summer. This is done for a few distinct reasons: first, it is important to test an irrigation model in summertime conditions – a period in which soil moisture would be most heavily altered – to determine the model's validity. Secondly, fogs do occur in the summertime, though not in the Central Valley, and could be influenced by an additional moisture source. Finally, applications beyond the scope of this thesis could utilize such a model for summertime conditions if indeed reliable and accurate. For these reasons, a much broader approach is taken towards irrigation with a driving force to understand its implications on cold pools in

California's Central Valley.

3.1 Background

Of the approximate 100 million acres of land in California, 9 million has been set aside for irrigated croplands (Thompson, 1986). While crops are grown in various places throughout the state, the majority resides in one location, California's Central Valley. In this naturally arid region, irrigation is provided via surface water diversion and ground water pumping (Reilly et al., 2008). When this is coupled with the world's largest patch of Class 1 soils[1] it results is one of the most productive agriculture regions on earth.

In terms of numerical weather prediction, irrigation causes a dramatic shift in the surface energy balance. Realistic simulations of these lower boundary conditions are critical for local variations in temperature and moisture which can have important effects on mesoscale weather (Pleim and Xiu, 2003). For example, the timing, strength, and precipitation from shallow cumulus clouds has been shown to be highly sensitive to the land surface characteristics and variability (Chen and Avissar, 1994; Wetzel et al., 1996). More directly, it has been shown that irrigation can have significant localized impacts on precipitation (Harding and Snyder, 2012). This is partially tied to the fact that the PBL development is heavily influenced by the partitioning of surface fluxes (Pleim and Xiu, 1995). Lastly, a properly resolved PBL is critical for accurate air quality modeling (Lui and Carroll, 1996).

Several papers have attempted to introduce irrigation by manipulating the soil moisture (Marcella and Eltahir, expeced 2013; Adegoke et al., 2003; Kueppers et al., 2007; Kanamaru and Kanamitsu, 2008). All of these techniques involve increasing the soil water content to a value between half field capacity and field capacity that in essence mimics real world practices. While this is the simplest and most direct approach to irrigation, the various soil moisture values among these papers reflect uncertainty.

The ambiguity derives from the fact that within a model grid cell, the fractional area of

[1]For agricultural purposes the land is ranked in capability classes from 1-7, with 1 having the fewest to no limitations.

active farms[2] is almost always less than one and varies by season. That said, if one can accurately recreate irrigation effects in a particular area by adjusting the soil moisture between field capacity and half field capacity, they have effectively accounted for idle croplands and other landuse categories within the grid cell. Simply put, if a crop requires soil moisture to be irrigated to field capacity daily, but the croplands only occupy 50% of a grid cell, what soil moisture value should one use? Applying only 50% of the water cannot be done because evapotranspiration as a function of soil moisture is highly nonlinear. So in reality, soil moisture is used as a tuning parameter based on the fractional area of active farms and one must acknowledge that what may work for one model or initialization, might not work for another. Essentially, you could be getting the right answer for the wrong reason.

For a more quantitative method on irrigation, Coleman et al. (2010) devised a scheme that operates on the annual water consumption as determined by the USGS. These data were said to be the most comprehensive source of annual water use sorted by activity (including irrigation) for all counties in the United States. In order to estimate the monthly water use for crops, the annual water consumption was normalized by the climatological monthly reference evapotranspiration[3] amounts provided by the California Irrigation Management Information System (CIMIS). However, there was no way to determine how much water was used daily, which led to the assumption that each day would have equal allocations of the monthly values. As one can see, this would create problems in days and months that do not have average conditions.

Recently, Ozdogan et al. (2010) has produced a scheme that reasonably reproduces the geographic patterns of the USGS annual irrigation water use. This irrigation model is based on a new dataset that characterizes the distribution of per-pixel fractional irrigated land. This dataset was created using gridded climate data and remotely sensed observations from the Moderate Resolution Imaging Spectroradiometer (MODIS) instrument; details are outlined in Ozdogan and Gutman (2008). Using 19 different crop types they triggered irrigation when the soil moisture dropped below 50% of field capacity and scaled the irrigation require-

[2]For the sake of this thesis, active farms are those that are in use for the respective time period. Croplands that go idle in winter are not considered active during that time.

[3]Grass that is 0.12 m in height and is well-watered is often used as the reference evapotranspiration.

ments by the fractional irrigated land to total crop land. With that said, irrigation is only applied when the relative greenness fraction[4] within a grid cell exceeds the 40% threshold.

Since our focus is on California crops and the California Department of Food and Agriculture (CDFA) report a number of them are grown throughout the winter (CDFA, 2013), problems arise. First, the 40% relative greenness threshold for irrigation will not be met in parts of fall, spring, and all of winter since the *relative* activity is less. Even if this threshold was removed, it would be wrong to assume the same amount of fractional irrigated land year around. Additionally, the plant maturity (programmed as rooting depth) is linked to greenness, which in places that have short growing seasons, may be reasonable. However, since crops are grown and harvested year around in California, greenness in a given grid cell may be more related to activity and not plant maturity, thus giving inaccurate latent heat fluxes.

While there are several options for irrigation in a numerical model, none seem appropriate for the year around crops grown in California. It is our goal to create a robust scheme that can be implemented on top of current land/atmosphere datasets and can be used throughout all seasons in California's Central Valley. These next sections will focus on the development, design, and impacts of an irrigation scheme while finally comparing it to traditional methods found in literature.

3.2 Model Description

The purpose of irrigation is to avoid vegetation stress caused by insufficient soil moisture. With this in mind, the first objective is to identify which crops are grown where. Ozdogan et al. (2010) has noted that using an average crop type in an irrigation scheme could result in large evaporation biases, both positive and negative. To avoid this, the United States Department of Agriculture (USDA), National Agriculture Statistics Service's (NASS) 2012 Cropland Data Layer (CDL), which shows the location of every crop type, was utilized.

[4]Here, the relative greenness fraction for a given grid cell is the current greenness, minus the minimum greenness, divided by the annual range of greenness.

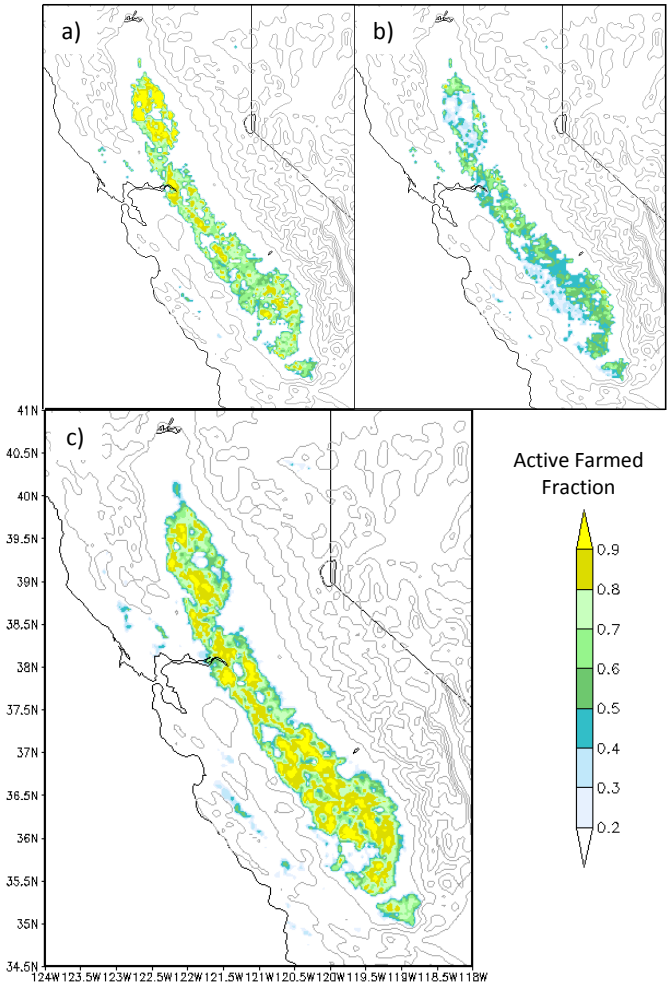

Figure 3.1: Panels a and b estimate the actively farmed areas for July and December, respectively. Panel c shows the actual farmed fraction based on the 2012 California CDL. For graphical purposes, images are presented at 4km resolution with terrain height contoured every 500 m.

The 2012 California CDL has an overall accuracy of roughly 84% with a 30 meter spatial resolution (USDA, 2012). From this, the sum of all crop types divided by the total area will produce the fractional area of active farms per grid cell (Fig. 3.1c). It is assumed that when the actively farmed area exceeds 50% in a grid cell, it behaves as either an active crop, or a combination of active and idle crops. If it does not exceed this threshold, the grid cell reverts to the usual land surface model, which in this case is the Noah LSM. This is also

indicated in the first tier of the flow chart in Fig. 3.2.

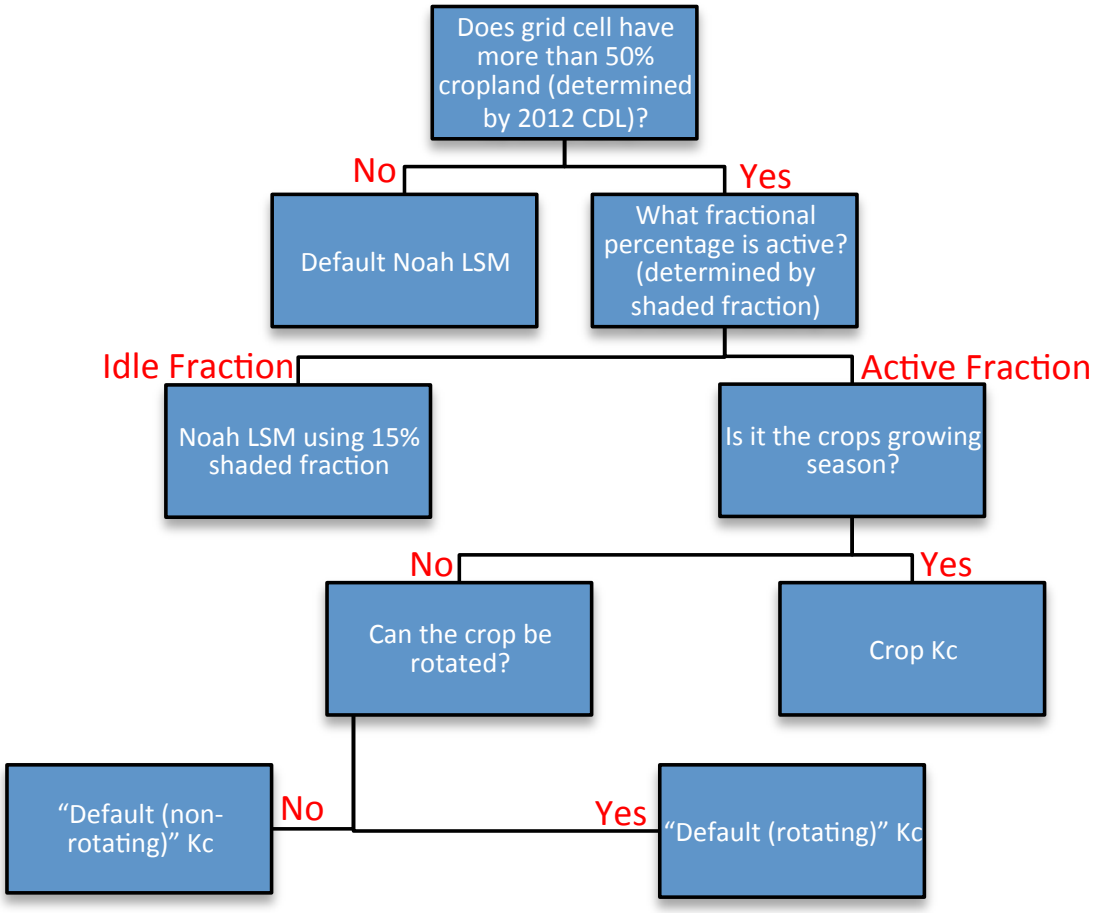

Figure 3.2: Programming logic for the irrigation scheme implemented on top of the Noah LSM (named NoahAG).

Unfortunately, the actively farmed area calculated from the 2012 California CDL focuses on large area summer crops. To determine how much area is farmed in the cool season, a wintertime equivalent will be needed. However, to the extent of the author's knowledge no such dataset exists, particularly for the Central Valley, therefore, one will have to be created.

In order to estimate the fractional area of active farms in winter we start by correlating the July shaded fraction[5] from MODIS to NASS's CDL active farm fraction in the San Joaquin Valley (Fig. 3.3). As one can see, the regression is not 1:1 but rather the active farm

[5]Provided by WRF's Preprocessing System (WPS) this is sometimes referred to as the Green Fraction.

fraction increases much faster than the MODIS shaded fraction. We believe this is because the farms are likely in an average state of growth for the Central Valley, therefore, having green crops cover the entire grid cell (hence a 100% shaded fraction) would be improbable.

To enforce a zero intercept, the actual regression line used in this thesis was redefined and is outlined in red (Fig. 3.3). Now, if one was to recalculate the summertime active farmed fraction via the shaded fraction and regression line, it would look quite similar to the actual dataset (Fig. 3.1a vs. Fig. 3.1c). In fact, the results of this thesis do not change whether the estimated or actual values are used for the summer. However, since winter time values are estimated (Fig. 3.1b), summertime values will be also.

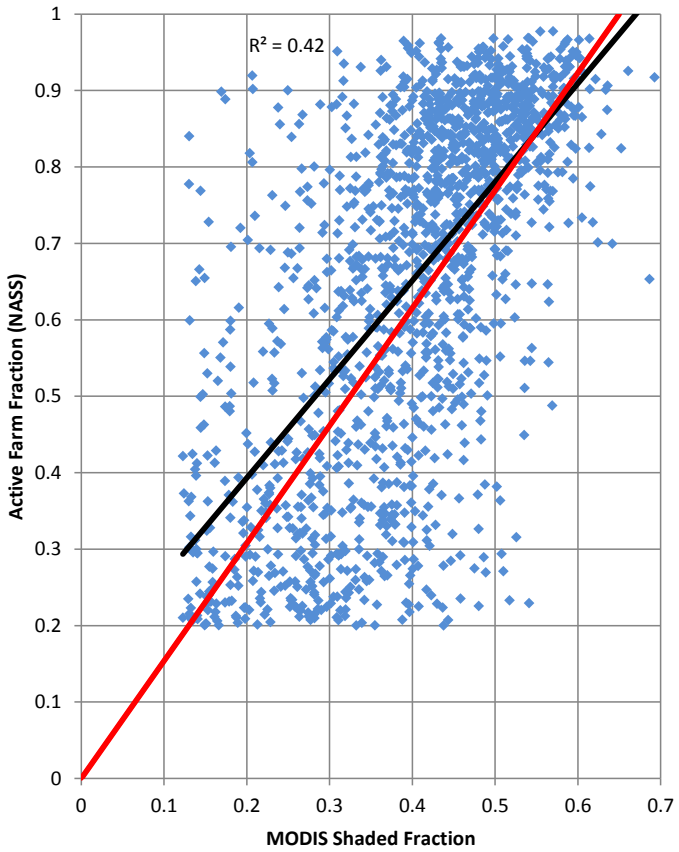

Figure 3.3: The active farm fraction based on the 2012 National Agriculture Statistic Service (NASS) Cropland Data Layer (CDL) is plotted against the July average (2001-2010) MODIS shaded fraction for points in the San Joaquin Valley. The least squares regression line is plotted in black while the actual formulation used in this thesis is plotted in red.

As previously stated, 50% of a grid cell (determined by the 2012 CDL) must be covered by croplands in order for the irrigation scheme to become active. Once the irrigation scheme is called, the active/idle farmland in both winter and summer is determined by the previously mentioned regression line (Fig. 3.3) and the seasonal MODIS shaded fraction within a grid cell (tier 2, Fig. 3.2). At this point, the fractional percent of idle land is treated via the Noah LSM with a 15% shaded fraction (tier 3, Fig. 3.2). This value was chosen because the shaded fraction provided by MODIS in the WRF model has a minimum threshold of 10-15% in areas with little to no vegetation (e.g. deserts).

For the fractional percent of active croplands, evapotranspiration values are based on the Food and Agriculture Organization (FAO) guidelines (FAO, 1998). First, a reference crop evapotranspiration (ETo) value is computed based on the Penman–Monteith equation. The reference crop is defined as a well-watered grass that is 0.12 m in height and has an albedo of 0.23. Next, the reference crop evapotranspiration is multiplied by a crop coefficient (Kc) to get the actual evapotranspiration. An appropriate crop coefficient is needed here since it adequately accounts for evapotranspiration differences between the actual and reference crop.

As one could imagine, Kc also varies by the stage of growth. As discussed earlier, Ozdogan et al. (2010) based the plant maturity on the relative greenness, although, in our area of interest crops are planted year around. Because of this, we relate greenness to activity and not plant maturity. Consequently, it was decided to use an average crop coefficient for each crop type. Of course, for some crops which are grown yearlong, such as alfalfa, an average crop coefficient may be most suitable.

The exact Kc values used in this thesis are seen in Table 3.1. Here, corn has a Kc value of 0.94 and is only active between calendar days 121 and 349. Outside of this date range that particular Kc value is considered invalid. However, if there is activity in a grid cell occupied by corn (or some other crop) outside of the growing days, it is assume that it has been replaced by a wintertime crop. The default wintertime Kc is 0.8 since we are unable to determine which crops are grown where during that season. In contrast, activity in grid cells outside the growing days for non-rotating crops, like fruit or nut trees, have Kc values that

are much lower (0.2). Finally, since the CDL is offered at 30 m resolution, a crop coefficient weighted by the fractional crop type can be computed. For example, a grid cell can contain 50% alfalfa, 25% cotton, 25% rice, and the crop coefficient would reflect that in a weighted average.

Crop	Growing Kc	Day Start	Day End
Corn	0.94	121	349
Cotton	0.78	0	365
Rice	1.11	0	365
Small Grain	0.85	0	365
Alfalfa	0.93	0	365
Tomatoes	0.92	60	258
Apples/Cherries/Walnuts	0.85	43	307
Peaches/Apricots/etc.	0.80	43	307
Grapes	0.60	71	305
Orange	0.75	0	365
Default (rotating)	0.8		
Default (non-rotating)	0.2		

Table 3.1: Crop Coefficients (Kc) relative to the reference crop. 'Growing Kc' values are used between 'Day Start' and 'Day End'. Outside of these days, crops able to rotate will use the 'Default (rotating)' Kc while non-rotating crops (fruit/nut trees) use the 'Default (non-rotating)' value.

While computing evapotranspiration in a numerical weather model by the FAO guidelines is fairly nontraditional, it has successfully simulated crop water consumption in other areas (Haddeland et al., 2006). The distinct advantage of this method is that a soil moisture value is not required, eliminating the need to guess an appropriate value for a grid cell that has an active farmed fraction less than one. With that said, the following sections will demonstrate the success of an irrigation scheme using FAO's evapotranspiration guidelines in California's

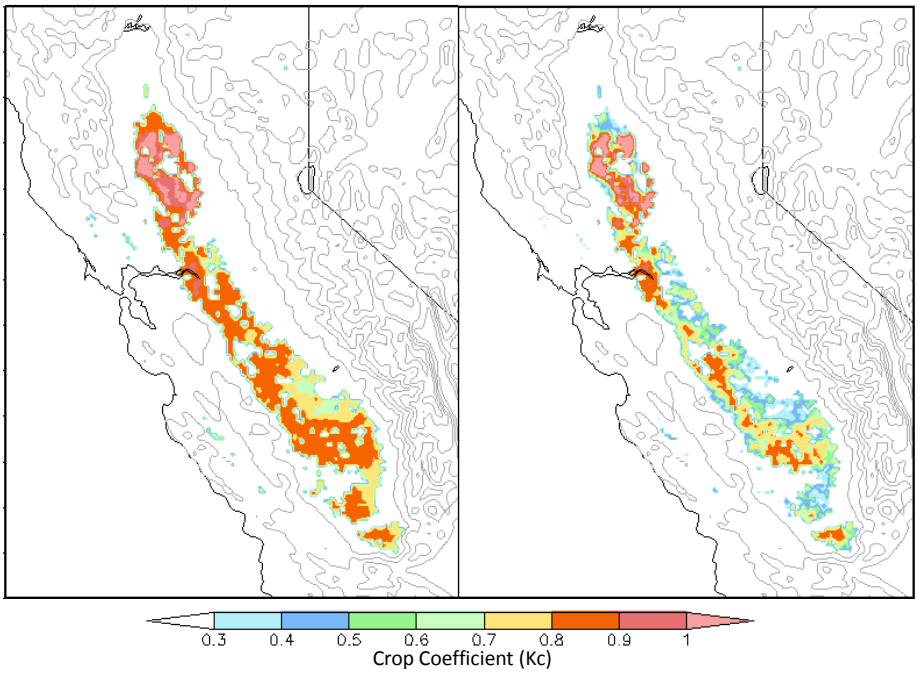

Figure 3.4: The average Crop Coefficient (Kc) shown for both summer (left) and winter (right). For graphical purposes, images are presented at 4 km resolution with terrain contoured every 500 m (gray contours)

Central Valley.

3.3 Methodology

Using the WRF model version 3.5, both summer and winter periods will be modeled over California's Central Valley to assess the impacts of agriculture. July 7-23, 2005 was chosen as the summertime period of interest since the weather was quite typical: hot, dry, and dominated by an upper level ridge. December 6-16, 2005 were the wintertime dates used owing to the relatively dry and stagnant conditions. As discussed in the last chapter, a weak frontal passage brought minimal precipitation to the CV on December 8 and 9.

The model setup includes doubly nested domains with a horizontal resolution of 36 and 12 km in addition to 51 vertical levels. The area encompassed by the 36 km domain can be seen in the shaded field of Fig. 1.2 with the 12 km nest outline by the white rectangle. The

standard model physics includes Lin microphysics, RRTM and Dudhia radiation, the YSU PBL, and the Kain-Fritsch cumulus parameterization.

In order to cover the long simulation periods, model reconstructions combined a sequence of shorter, overlapping simulations, in which a new run is initialized (as a cold start) every other day. This means the first 24 hours is overlapped by the previous simulation and is subsequently removed. Model initializations will come exclusively from the NARR though others have been tested and will be discussed briefly in this chapter.

Surface observational data were collected from NCAR's Research Data Archive (RDA) which consists of both ASOS and AWOS stations. The exact locations of these data used to verify the model are shown in Fig. 1.2 (red dots). Since we are modeling irrigation effects in California's CV, results will focus on statistics computed from the CV subset (Fig. 1.2).

3.4 Results

3.4.1 Summer

The modeled dew points in California's Central Valley increase in each season as a result of the irrigation scheme, however, the change in summertime moisture is particularly dramatic. On average, the summertime afternoon/evening dew points for the Noah LSM with irrigation, named NoahAG for this chapter, are 4 to 5+ Kelvin warmer than the original Noah LSM for a large portion of the Sacramento and San Joaquin valleys (Fig. 3.5 left). In the Sacramento Valley and delta regions, most stations are not located around croplands and experience little if any change in dew points. This is important because future statistics that aggregate all CV stations (the CV subset) will appear to have smaller differences. In contrast, most stations in the San Joaquin Valley, especially ones further south, are under a rather large influence from irrigation. There are even a few stations (Hanford, Lemoore, and Visalia) that have, on average, afternoon/evening dew points that are more than 5 Kelvin warmer than the regular Noah model. The impact of the additional moisture has also lowered summertime PBL heights quite substantially in some cases (Fig. 3.5 right). Most notably, a large swath

of the Sacramento and San Joaquin valleys PBLs decreased by over 5 hectometers (hm). As previously mentioned, this can have rather large implications on air quality models.

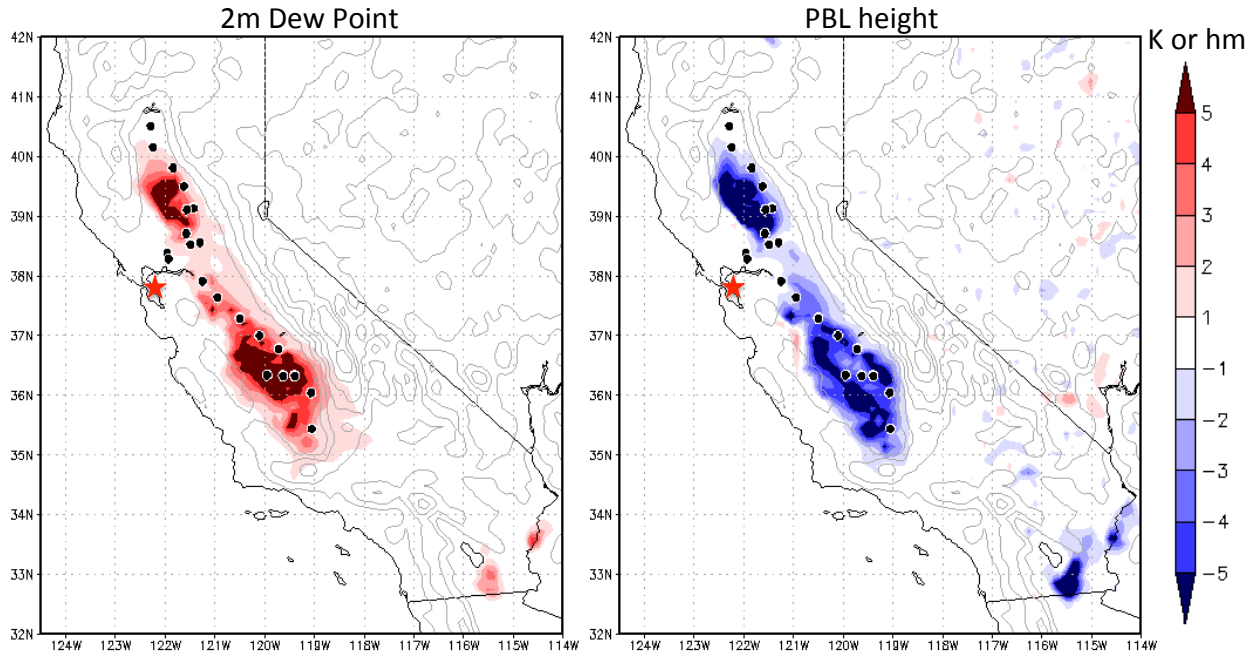

Figure 3.5: The change in average (July 7-23) dew points (K, at 03Z) and PBL heights (hm, at 00Z) between the NoahAG and Noah models at the time of maximum difference. The black dots represent stations included in the CV subset while the red star indicates the location of the Oakland upper air station.

A time series of observed summertime CV dew points verses those predicted by the Noah LSM reveals a large dry bias (Fig. 3.6 top). As mentioned, this combines multiple forecasts, disregarding the first 24 hours, to create a continuous time series. The aggregate of CV stations shows that the NoahAG model, on average, increases summertime dew points between 2-3 K on most days. However, smaller differences can be seen earlier in the month (July 7-12). One should keep in mind the relatively large number of stations that reside outside the croplands main influence (Fig. 3.5) which mitigates the differences seen here between the Noah and NoahAG models. Lastly, it should be noted that the author has performed sensitivity tests (not shown) with different soil initializations (ERA interim, NAM, and HRLDAS spun soils) revealing that the large dew point bias is a pervasive feature.

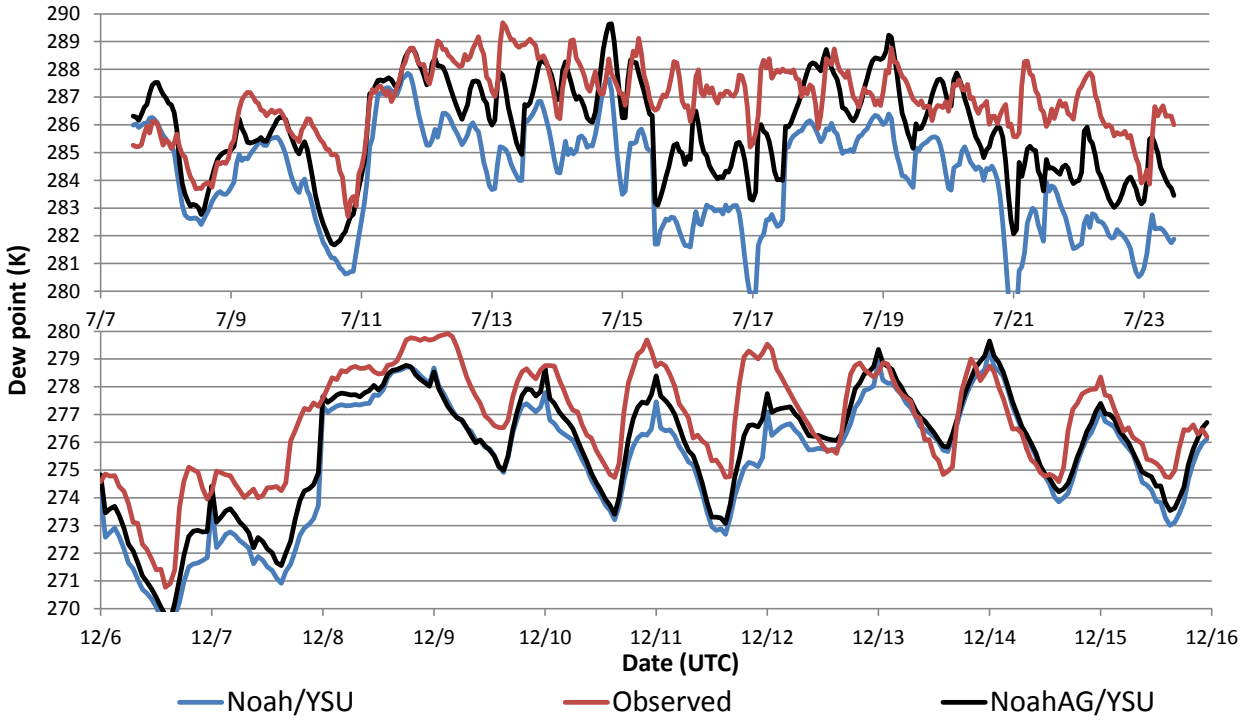

Figure 3.6: Modeled and Observed dew points averaged over the CV subset for both July and December 2005.

From this figure, it appears that the NoahAG model only fixes about half the dew point bias, unfortunately. To understand the remaining error one must know the unusual summertime flow patterns that exists in the Central Valley. During this time of year, cool, moist, Pacific air continually collides with the warm and dry continental air mass which in and of itself is quite typical for coastal locations. However, the flow patterns are not horizontal as in the typical sea breeze model, in fact, there is sizable downsloping making the origins of the CV air mass quite unique.

When looking at a cross section averaged at 01 UTC over July 7-23 (Fig. 3.7), the theta contours (solid black) produced by the WRF model resemble something more of a downslope wind storm rather than a gentle sea breeze. Since the coastal range separates almost the entire CV from the Pacific, lower potential temperature (marine) air is not readily able to penetrate into the valley. Because of this, the Central Valley is able to become much warmer which further increases the temperature/pressure gradients. Finally, because the mountains

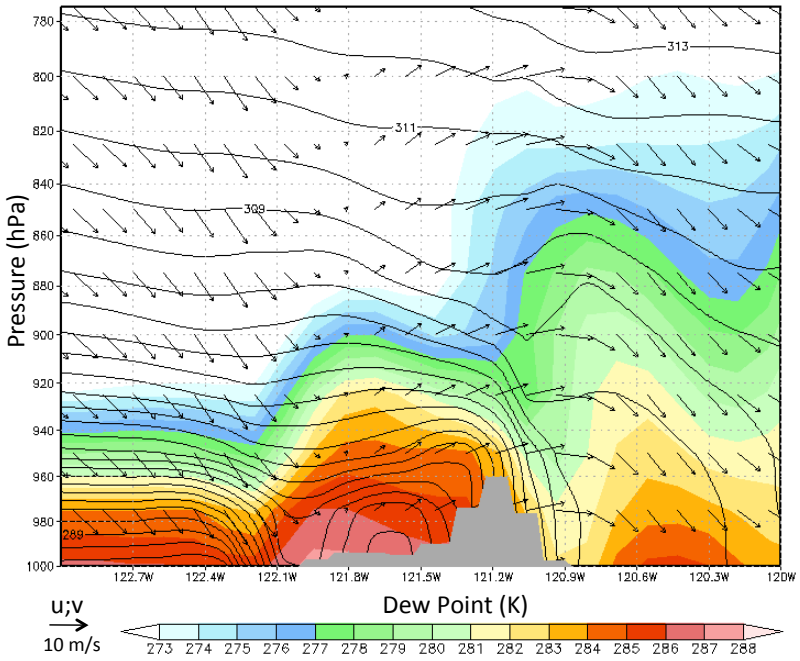

Figure 3.7: Average (July 7-23) winds (u;v vectors), potential temperatures (contoured), and dew points (shaded) at 01 UTC, or 6pm LST at 37 degrees north for the NoahAG model.

are not too tall, the flow is not completely blocked and air from higher aloft (880 hPa) is able to reach the surface of the CV.

This is further demonstrated in Fig. 3.8 which shows the average (July 7-23) evening (01 UTC) pressures of the 307 K isentrope (shaded) along with winds on that surface (barbs). In this environment, the flow is adiabatic, so looking at a particular theta surface will reveal the origins of an air parcel. For example, the 307 K isentrope is located approximately 200 hPa above the ocean surface. However, the air mass is moving to the east towards a warmer environment at approximately 5 m/s or 432 km/day and it must descend. At this latitude (38° N), each degree longitude is separated by approximately 87 km which means the flow is moving approximately 5° longitude per day. During this journey, the air parcel descends from roughly 800 hPa to the surface of the CV valley. Because the coastal range is not too tall, and doesn't completely block the flow (as shown in Fig. 3.7) the air aloft can reach the surface.

In terms of identifying the CV dew point biases apparent in the NoahAG model during

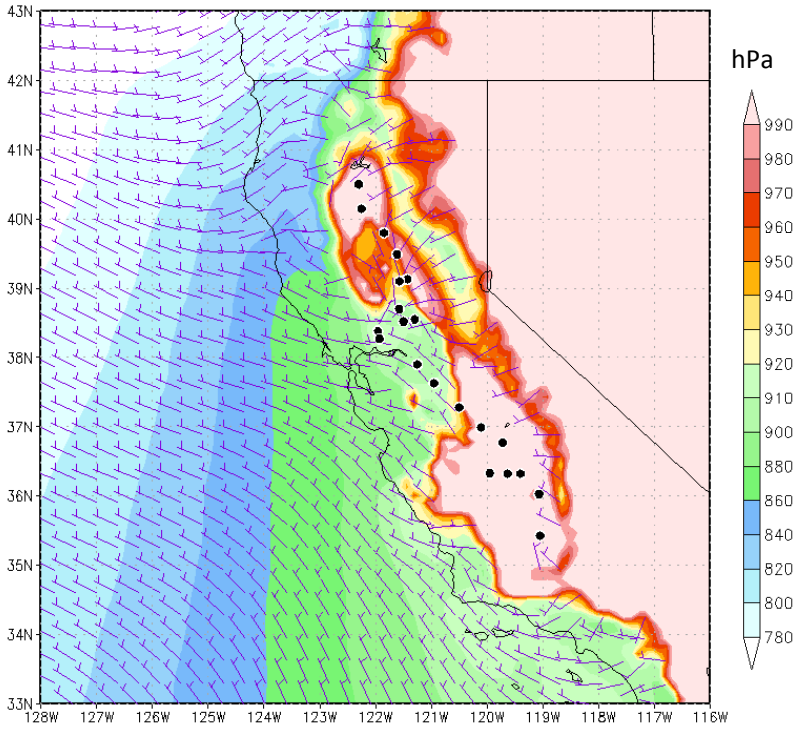

Figure 3.8: Average (July 7-23) pressures (shaded) and winds (barbs) on the 307 K isentrope surface at 01 UTC, or 6pm LST for the NoahAG model. CV stations are shown by the black dots.

certain periods, one should be looking aloft and upstream. Unfortunately, only the Oakland upper air station (Fig. 3.5) fits into these qualifications. When plotting the modeled bias aloft at Oakland – which is independent of the irrigation scheme – as a function of the forecast hour (Fig. 3.9), it becomes obvious that a substantial dry bias exists and grows with time[6].

Of course, this is only one location making it unreasonable to correlate it exactly to the CV bias. However, during the first 18 hours of the simulation when there is likely smaller biases upstream, CV dew points are modeled almost perfectly using the NoahAG model. It is not until after sunset do things begin to deviate from the observed. Currently, it is believed that before sunset, a dry bias upstream is mixed throughout the immense

[6]The appearance of forecast hours 0-24 are only included for demonstration purposes and are not used in any other figure/table.

summertime boundary layer having minimal effects; it is not until sunset (Fig.3.7) can the air from 925-850 hPa layer reach the surface in much higher concentrations. It should be noted that while Fig. 3.9 focuses on the 875-850 hPa layer, the bias persisted down to 925 hPa. Other layers, above and below these levels, had relatively little bias which may suggest that the marine PBL height is not accurately modeled.

In order to test that the surface bias is related to the upstream upper levels, runs were nudged to the analysis above the PBL or sigma level 5, whatever was higher (Fig. 3.9). This revealed that the slow drying trend throughout the forecast period could be alleviated, if not

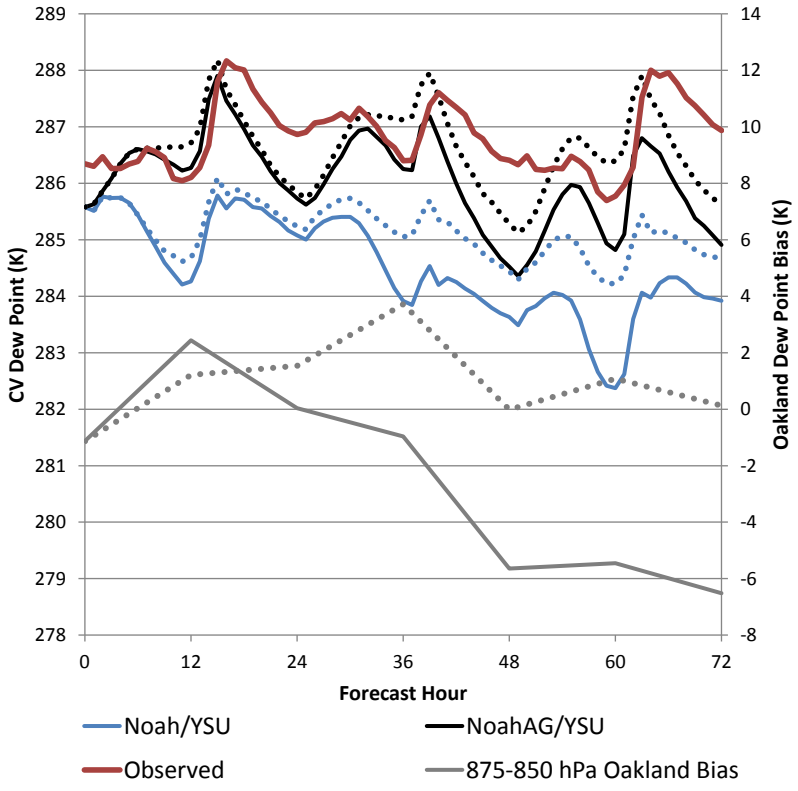

Figure 3.9: Dew points averaged by forecast hour over all 8 summertime simulations. The Observed, Noah/YSU, and NoahAG/YSU lines show dew points averaged over the CV subset. Upstream observations of dew points (gray line) are independent of the crop parameterization and averaged at Oakland. Dotted lines represent runs in which the dew point was nudged to the analysis above the PBL, or sigma level 5, whatever was higher.

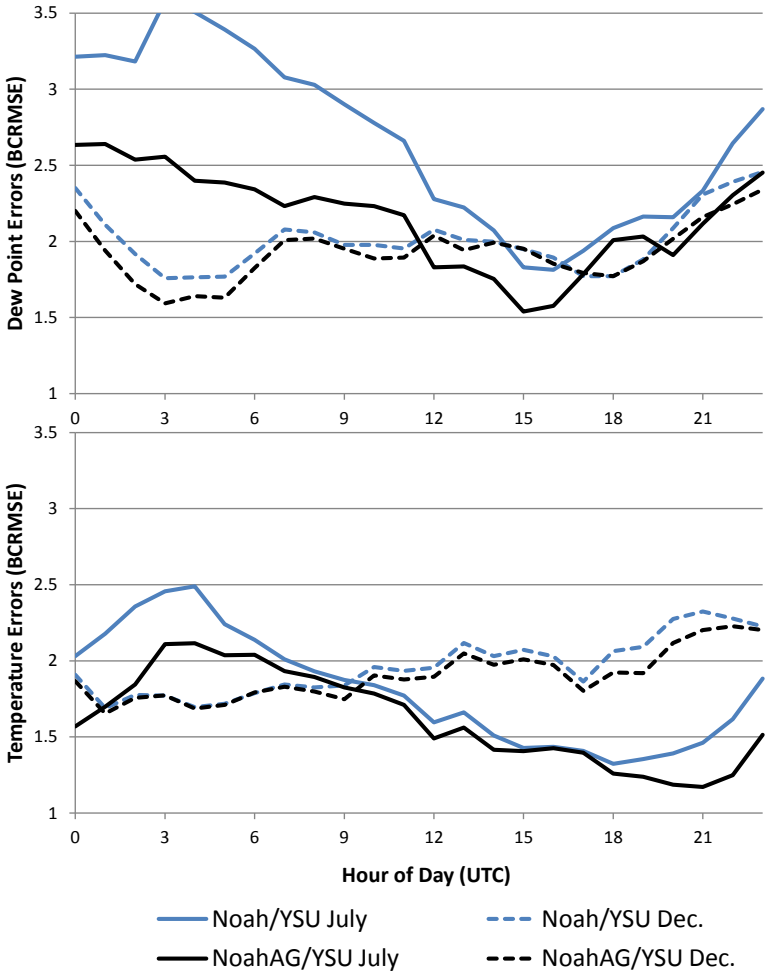

Figure 3.10: The diurnally averaged BCRMSEs for dew points (top) and temperatures (bottom) during both July and December for the CV subset.

entirely removed, in the NoahAG model. However, the drying that occurs at nighttime is still roughly 1 K too large. This 1 K bias is a result of the Southern San Joaquin and Northern Sacramento valleys being too dry, while the delta and surrounding regions are unbiased. It should be noted that even before nudging, the delta region was unbiased owing to the fact that surface marine air, which had no moisture bias, routinely infiltrated the region because of a lack of upstream blocking. It is only in places away from the delta that have the upstream flow blocked and thus sizable downsloping, does a bias persist. Unfortunately, there are no upstream upper air observations away from the delta, meaning there is no way of knowing that nudging to the analysis is right since the analysis may be systematically

biased in these regions. However, as of now, half of the dew point bias seen in the default WRF model appears to be related to the exclusion of local processes (i.e. irrigation) while the remaining half is likely non-local.

Because model biases can have so many different origins and distract the analysis from the truth, it sometimes can be more valuable to inspect the bias corrected errors (Fig. 3.10). Here, the Bias Corrected Root Mean Squared Errors (BCRMSE) are averaged over the diurnal cycle for both dew point (top) and temperature (bottom) for the July simulations (solid lines). For summer afternoons and evenings, the Noah model has substantially larger BCRMSEs than the NoahAG. In addition to the changes in dew point, the other side effect of increased evaporation is cooler temperatures. As seen at the bottom of Figure 3.10, irrigation acts to decrease the bias corrected temperatures during the same time dew points were improved. While these improvements in temperature are less than those of the dew points, a rather still significant change of 0.5 K is seen during the afternoon hours.

3.4.2 Winter

CV wintertime simulations have a persistent dry bias, evident by Fig. 3.6, though nowhere near the magnitude of summers. Here, the NoahAG shows only minor improvements to biases with the most noticeable improvement coming mid-month on the 11th. The differences seen here appear to be relatively unimportant, partially owing to the fact that stations relatively unaffected by irrigation are averaged in.

In terms of bias corrected errors, wintertime dew points and temperatures see only a modest improvement (Fig. 3.10). Just as with summer, the largest improvements occur during the daytime hours. It does not go without saying that in terms of bias corrected errors, the NoahAG can outperform Noah during both seasons and at any time of day.

On December 14, the changes in wintertime surface dew points (Fig. 3.6) are even smaller, perhaps unnoticeable. However, changes to other areas in the model are certainly non-negligible. This is demonstrated on the morning of December 14 when the entire San Joaquin Valley was enveloped in Tule fog (Fig. 3.11a), a common occurrence for this time of year.

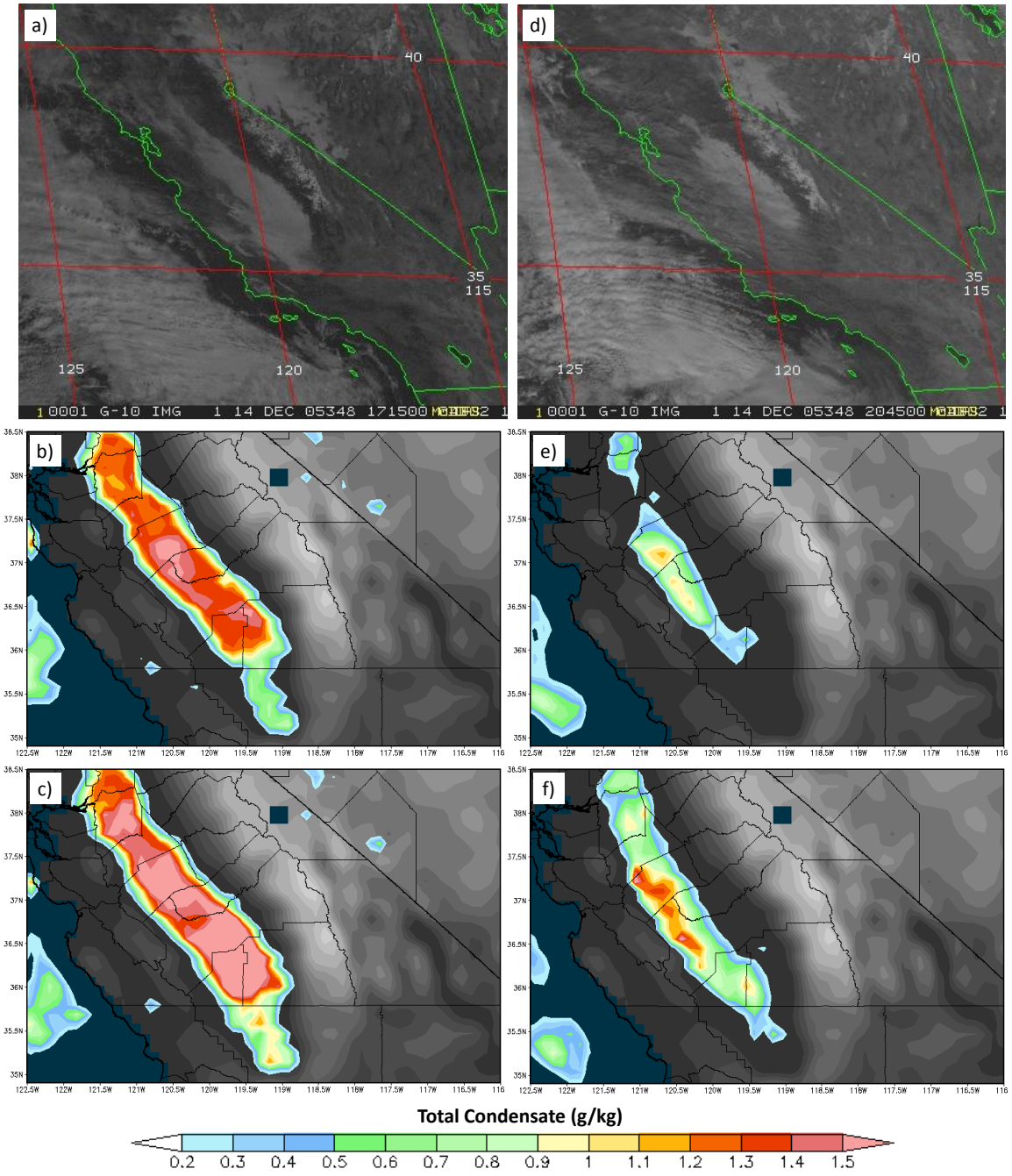

Figure 3.11: Visible satellite imagery (a,d) shown along with modeled total condensate (g/kg) for the Noah (b,e) and NoahAG (c,f) models on December 14. Images a-c are taken at 17 UTC (17:15 UTC for satellite), approximately the time of maximum fog extent while d-f are at 21 UTC (20:45 UTC for satellite).

At this same time period of maximum fog extent, 17 UTC, total condensate produced by Noah (Fig. 3.11b) and NoahAG (Fig. 3.11c) is shown. One can observed that irrigation has acted to increase the severity of the fog, albeit slightly, in almost all places. By 21 UTC, it appears[7] that some of the fog has eroded away from the northern and southern ends of the valley while the vast majority still persists. Here, the modeled total condensate from NoahAG (Fig. 3.11f) is not only thicker than Noah (Fig. 3.11e) but also more widespread.

The point of this illustration was not to demonstrate that one particular scheme is better than the other, but rather small differences seen in the averaged diagnostics (Fig. 3.6) can be misleading. An analysis over the San Joaquin Valley reveals that dew points on the first sigma level were on average 0.5 K higher than the Noah model the day before (and morning of) the fog event; still rather negligible. However, this highlights the sensitivity of Tule fog to surface moisture. One can not help but wonder that if the widespread fog event occurred two days earlier on the 12th, where the NoahAG had differences in dew points exceeding 2 K in places of the San Joaquin Valley, how much more of an impact would irrigation have?

Of course, this is only one example that happened to coincide with the wintertime simulations which certainly means there will be other cases where irrigation has more or less influence. Up until this point it was assumed that wintertime irrigation was relatively unimportant, however, it is clear by these high impact events that additional research may be needed.

3.4.3 Comparison with Other Schemes

It is useful to demonstrate the performance of the NoahAG irrigation model to others found in literature, specifically, to those schemes that rely on adjusting soil moisture to specific values. In order to do this, a modified version of the Noah LSM was created in which soil moisture was increased to field capacity (and half field capacity) every 24 hours, allowing the soils to dry out in-between. Just as with the NoahAG, irrigation was activated during both summer and winter to locations were the summertime 2012 CDL actively farmed areas exceeded 50%

[7]At this time, high clouds have moved into the south-east portions of the San Joaquin Valley and have obscured part of the satellite imagery.

(Fig. 3.1c). What differs here is that the actively farmed areas are not reevaluated using the shaded fraction. This was done because it is difficult to determine a soil moisture value for a particular grid cell that has a fractional percentage of farms, as previously discussed. So trying to find the best soil moisture for a particular grid cell – which all have different actively farmed fractions that vary by seasons – is a guessing game. This is why two different soil moisture values (field and half field capacity) were applied to crop locations, to tease out the best result by trial and error.

	July 2005					
	Temperature (K)			Dew Point (K)		
	Bias	BCRMSE	RMSE	Bias	BCRMSE	RMSE
Noah	-1.22	1.81	2.56	-2.74	2.68	3.98
NoahFC	-2.56	1.65	3.28	0.13	2.23	2.61
NoahAG	-2.08	1.62	2.90	-1.02	2.16	2.70
	December 2005					
	Temperature (K)			Dew Point (K)		
	Bias	BCRMSE	RMSE	Bias	BCRMSE	RMSE
Noah	0.25	1.96	2.33	-1.44	2.01	2.66
NoahFC	0.12	1.87	2.32	-0.26	1.94	2.15
NoahAG	0.06	1.90	2.28	-0.98	1.93	2.33

Table 3.2: Overall Statistics averaged over the CV subset for July and December 2005.

It was found that the Noah model with soil moisture values modified to field capacity, called NoahFC, produced better results than the half field capacity for both summer and winter. For this reason, only a summary of the NoahFC experiment is shown (Table 3.2). During the summertime, the temperature bias for both the NoahFC and NoahAG were larger than that of Noah. However, even the default Noah model had a moderate cold bias that could only be improved by switching initializations. It should be noted that while this alleviated, though did not remove the cool bias, it had no effect on the pronounced dry bias.

Since the cooler temperatures caused by irrigation are more realistic but are causing higher errors in this case, one should focus on the change in bias corrected errors. For dew points, the NoahAG model had the smallest bias corrected errors while the NoahFC has the smallest RMSEs due to a minimal bias. However, we have already discussed that the summertime dew point bias from the NoahAG model is likely correlated to the upstream flow, which means NoahFC is getting the right answers for the wrong reasons. Of course, either of these methods offer substantial improvements over the default Noah.

The overall statistics for wintertime have much less variability, although, we have already shown that even small changes can have large impacts on CV fog (Fig. 3.11). By a small margin, the NoahAG takes the top spot for bias corrected dew points while the NoahFC has the smallest bias and lowest RMSEs. However, one must remember that NoahFC actively irrigates (no idle crops) locations where the 2012 summertime CDL (Fig. 3.1c) exceeds 50%, regardless of season. This must certainly mean that the amount of watering is grossly overestimated for winter; but remember, replenishing the soils with half field capacity did not produce results as desirable. So again, NoahFC is getting the right answer for the wrong reasons which degrades the models ability to give physical and meaningful explanations to real world phenomena.

CHAPTER 4

Adiabatic Cold Pools

In Chapter 2, stable cold pools were discussed, exploited, and ultimately improved. However, on some occasions stable cold pools can become saturated and subsequently create fog. If thick enough, fog can efficiently cool the stable cold pool from the top-down and cut off the majority, if not all, of the surface cooling. This can quickly transform a stable profile into a weakly turbulent and unstable situation that eventually creates a moist adiabatic environment, hence the name, adiabatic cold pool. These events are utterly different and more complicated than their stable counterparts owing to the increased turbulence, entrainment, and introduction of cloud droplets. The following chapter will demonstrate our current challenges with forecasting adiabatic cold pools and will focus on understanding and providing solutions to the origins of error.

4.1 Methodology

Using WRF version 3.5.1, radiation fog in California's Central Valley will be modeled in both the idealized and real data setting. For our real data cases, different atmospheric initializations and initialization times were tested and their influence was deemed important. For example, the location and longevity of low clouds forecasted by the WRF model was better for one initialization than another. It is for this reason alone that the first event is initialized with the ERA-interim (December 29, 2008) while the final two are initialized with the NARR (January 4 & 13, 2011).

Several tests were performed concerning initialization lead time. It was found that initializing too close to fog formation (or even during) would inhibit or prevent the formation

of fog. This was largely traced to an inadequate initialization for such a detailed surface process. On the other end of the spectrum, initializing too far out would allow errors to accumulate and ultimately deteriorate simulations. It was concluded that initializing roughly 12-36 hours before fog formation provided an acceptable middle-ground.

The simulation periods are December 29, 2008 - January 2, 2009, January 4-7, 2011, and finally January 13-16, 2011. It is during these times we see the San Joaquin Valley and a large portion of the Sacramento Valley inundated by fog. Synoptic conditions across all events are dominated by a Great Basin surface high pressure which is ideal for cold pool formation.

The model setup includes a triply nested design with horizontal resolutions of 36, 12, and 4 km; however, not all simulations will employ domain 3. The area encompassed by the 36 km domain can be seen in Fig. 1.2 with the 12 and 4 km nests outlined by the white rectangles. Experiments will use 62 vertical levels which have a modified grid to include 19 model levels below 1 km. This differs from the default real.exe behavior which sets the first 8 full sigma levels (roughly the lowest kilometer) to constant values regardless of the number of vertical levels chosen. The standard model physics include the WRF double moment, 5-class scheme (WDM5) microphysics, new Goddard radiation, the YSU PBL, Kain-Fritsch cumulus parameterization in domains 1 and 2, and the Noah LSM. Additionally, the newly added gravitational settling option for cloud droplets is activated[1] since is has been shown to be of importance when modeling fog cloud water concentrations (Bergot et al., 2007).

Validations of the weather reconstructions have been performed principally with the MET software, maintained by the Developmental Testbed Center at NCAR. This package was used to compare observations to model reconstructions that were spatially interpolated to the observation point. Observational data were collected from MADIS and consists of surface ASOS and AWOS stations. The exact locations of these data used to verify the model are shown in Fig. 1.2 (red dots). However, since we are modeling cold pools in California's CV, results will focus on statistics computed from a subset of stations outlined

[1]It should be noted that the module controlling gravitational settling of fog droplets had several bugs in WRF version 3.5.1 but has since been fixed by the author for this thesis and future versions of the WRF model.

by the white polygon called the San Joaquin subset. 10-11 (event dependent) stations reside in this polygon which provide ample verification given the homogeneous nature of fog.

4.2 Results

Presented in Fig. 4.1a is the temperature (solid) and dew point (dotted) observations (red) from Dec. 29, 2008 - Jan. 2, 2009 averaged over the San Joaquin subset. At bottom, the number of stations with observed ceilings (red) less than 1000 m (dotted) in addition to the average ceiling heights (solid). One can observe that on the night of the 30th (12Z) and into the day of the 31st, about half (of 11 for this event) of the San Joaquin stations were reporting ceilings less than 1000 m. It wasn't until the night of the 31 (12Z) did the average ceilings of the San Joaquin subset drop close to zero and the number of reporting stations rose to a maximum of 11. Over the next 36 hours, the average observed ceilings slowly increased over the San Joaquin subset which is also reflected in a gradual increase in the dew point depression. It should be noted that ASOS stations often report a ceiling of 30 m (and rarely 0 m) when fog is observed.

4.2.1 Model Diffusion

As discussed and shown in Ch.2.2.1, default model diffusion can have an moderate impact on forecasting stable cold pools. In that chapter, the pooling of cold air was quite shallow and did not involve any condensate. Since this chapter deals with cold pools that are completely different in nature, it is again important to test the impact of model diffusion.

In order to demonstrate the magnitude at which horizontal diffusion errors can accumulate, we compare simulations using the default model diffusion (Fig. 4.2a) to one that uses no horizontal diffusion (Fig. 4.2c). Here, total model condensate (g/kg) is shaded for a quick comparison of cloud cover during 18 UTC Dec. 31, 2008. As one can see from this early morning picture, a period where fog should be most widespread, no low clouds exist in the Central Valley when using the default model diffusion (Fig. 4.2a).

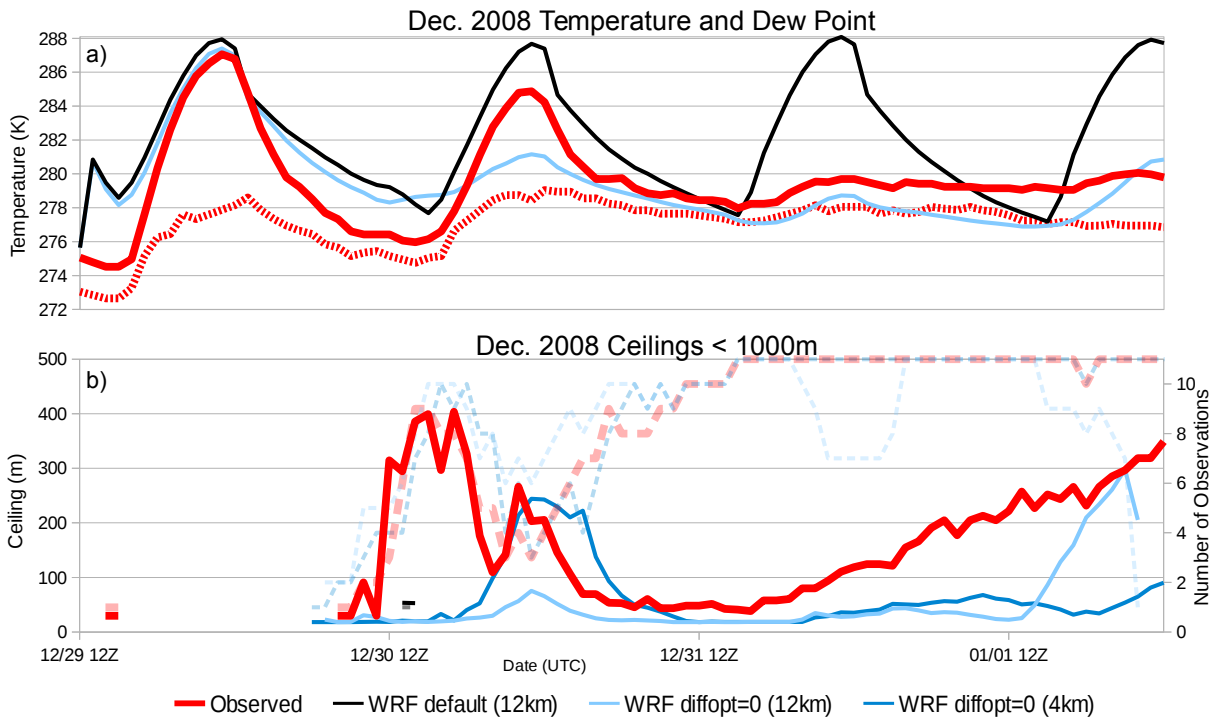

Figure 4.1: At top, observed (red) and simulated (blue) temperatures (solid line) and dew points (dotted line) for the San Joaquin subset from Dec. 29, 2008 - Jan. 2, 2009. Over the same area, the number of observed and forecasted stations with ceilings less than 1000 m (dotted line) is shown along with the subsequent ceiling heights (solid line). Forecasted dew points are not shown for simplicity

This is in stark contrast to the run that has no model diffusion (Fig. 4.2c) and shows a large swath of Tule fog encompassing most of the Central Valley. When comparing this with the visible satellite imagery (Fig. 4.2d) it is clear which run is more realistic, although, this is only one time period. However, this experiment was repeated for multiple events over multiple days which all produced the same result: using diffusion on model coordinates substantially degrades forecasts by eroding the cold pool via improper along-slope numerical diffusion. Lastly, the results over the ocean should be similar since the sigma coordinates are truly horizontal. However, the amount of low clouds south of Point Conception are dramatically different between Figs. 4.2a and c owing to the adjacent landmass.

It is important to note that simulations in Fig. 4.2 only use domains 1 and 2 (36 and 12

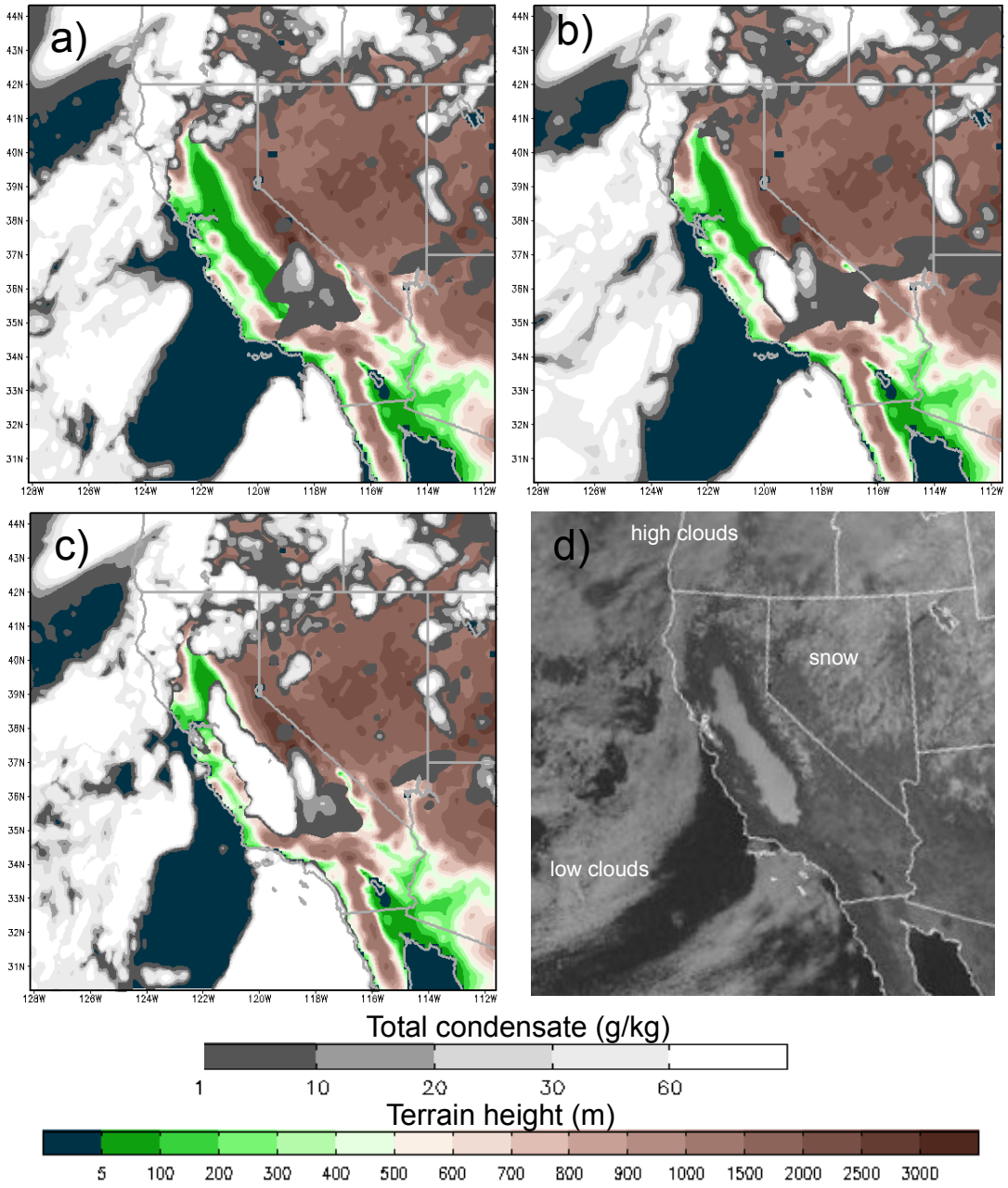

Figure 4.2: Modeled total column condensate is shown for 18 UTC, Dec. 31, 2008 (a 54 hour forecast) using default model diffusion and no 6th order filter (a), no diffusion but a 6th order filter which is both monotonic and positive-definite (b), and no diffusion and no 6th order filter (c). Image d shows the visible satellite imagery for the same time period. Simulations presented here do not make use of the 4 km domain.

km). Billings et al. (2006) noted that a run with lower resolution which calculated diffusion in physical space could produce results similar to a higher resolution run with diffusion operating on model levels. This is because at higher resolution the gradients between terrain following coordinates are weaker, which makes for a less erroneous calculation. Testing this in the Tule fog case revealed that a 4 km horizontal resolution run with sigma level diffusion had results similar – though still degraded with respect to valley fog coverage – to that of a 12 km simulation with no diffusion (not shown).

Increasing the horizontal resolution to account for the limitations of diffusion in the WRF model is not a practical solution. First, one must consider that as the horizontal resolution increases by a factor of 2, an 8 fold increase in the computational power is needed. Secondly, even if one did increase the horizontal resolution, there would still be features in other areas that are adversely affected by the diffusion calculation. For example, many parts of the Southern San Joaquin Valley approach or even exceed 100 km in width; meaning, at 12 km horizontal resolution 8 grid points resolve the valley. In order to alleviate diffusion errors, one must increase the resolution by a factor of 3, to 4 km, which makes for an excessive 24 points in the valley. Now, one would see that the problem is not fixed, but shifts to terrain features that are 1/3 in size. So it seems, increased resolution is not the solution, but a way to mask diffusion errors when calculated on sigma levels.

As an additional test, the monotonic and positive-definite 6th order short-wave numerical filter was activated without the use of diffusion (Fig. 4.2b). Most often, users use this option to increase the stability of the numerical model by eliminating sharp gradients. However, it too operates along model levels and can have serious impacts on simulations. As one can see, it does not quite eliminate all of the fog in the Central Valley, yet is a serious deviation from an identical simulation that uses no 6th order filtering (Fig. 4.2c).

Because of these results, we cannot recommend using diffusion on model surfaces or even a higher order numerical filter that operates in the same way. At this point it seems most desirable to get diffusion option 2 (which operates in physical space), working within the WRF model[2]. Because of this work, the subsequent release of WRF (version 3.6) improved

[2]In WRF version 3.5.1, diffusion option 2 is numerically unstable at any of the resolutions used in this

diffusion option 2 to run at all resolutions. This was done by implementing a non-dimensional slope parameter that effectively reduced diffusion near sloping terrain. This provided the numerical stability needed for the WRF model. We have backported this code to version 3.5.1 and have found it produces results nearly identical Fig. 4.2c. For these reasons, we have chosen to run the model without horizontal diffusion from this point forward. Additionally, 6th order horizontal diffusion is turned off since it too substantially degrades fog forecasts.

Turning back to Fig. 4.1a, a simulation using the default model diffusion (which operates on model levels) and uses no 6th order filtering is plotted in black. Here, one can observe that the problem is not unique to the particular day but evident throughout the extended period. While dew points are not shown for simplicity, they can be inferred by looking at the ceiling heights at the bottom of Fig. 4.1b. If one looks carefully, it can be seen that there was just one hour where one station was reporting a ceiling just below 100 m using the default diffusion package.

As indicated by Fig. 4.2c, turning off diffusion creates an entirely different simulation throughout the extended period (Fig. 4.1). What is notable here is that the number of stations reporting ceilings less than 1000 m (Fig. 4.1b dashed lines) match very closely to what was observed (excluding the end of the forecast period). This shows that the amount of area encompassed by fog agrees well with observations.

By the time we reach the end of the 84 hour period, even the no diffusion 12 km simulation rapidly deteriorates as all the fog burns off. This can be seen by a rapid rise in simulated ceiling heights and a subsequent drop in the number of stations reporting ceilings less than 1000 m. However, this early burn off was alleviated by creating an identical simulation utilizing all 3 domains (dark blue).

While this may have extended the longevity of the fog, there is still an extremely large low ceiling bias regardless of the resolution used. Unfortunately, this behavior is not unique to this particular case, in fact, the ceiling bias is evident across all events (shown later). Additionally, changing the initialization or initialization time shows no benefit. Because of

study.

this, we view this problem as a model deficiency. Modeling the evolution and life cycle of fog is extremely complicated and depends on a number of physics packages in the WRF model including, but not limited to: microphysics, radiation, PBL, and the LSM. As one can see, pin-pointing the exact physics responsible for the majority of the forecast degradation can be a daunting task.

Fortunately we are able to compare one particular physics option to what one would expect in reality, the PBL. This is attainable by creating idealized Large Eddy Simulations (LES) and comparing them to coarser grid simulations dependent on a PBL parameterization. Because we are able to do this comparison, the boundary layer will be the starting point – though perhaps not the complete solution – for the fog modeling problem and the focus throughout the rest of this chapter.

4.2.2 Large Eddy Simulations

Using the WRF model we have performed LES simulations using a typical CV wintertime fog profile. We then modified this profile to make it super-saturated in the lowest 150 m which would allow a cloud to be produced in the first time step. The domain has 30 grid points in each horizontal direction with periodic boundaries and 101 vertical levels. Approximately 38 of these levels are in the lowest kilometer creating a vertical resolution of roughly 16 m near the surface while the remaining are stretched vertically to the model top of 12 km. Finally, a horizontal resolution of 33 m was chosen, though even larger grid spacings produced similar results. It should be noted that additional experiments with various domain sizes and boundary conditions were performed with each having little to no effect on the results.

Since the growth of fog is dependent on cloud top cooling, a radiation and microphysics scheme is needed. Here, the same microphysics (WDM5) and radiation scheme (new Goddard) is used. Additionally, as the fog lifts, the surface flux becomes important and will be handled again by the Noah LSM. While it may not be typical to have a full physics LES simulation, it is certainly necessary with fog/stratus.

The results for the LES simulation can be seen in Fig. 4.3a. Here, clouds form after the

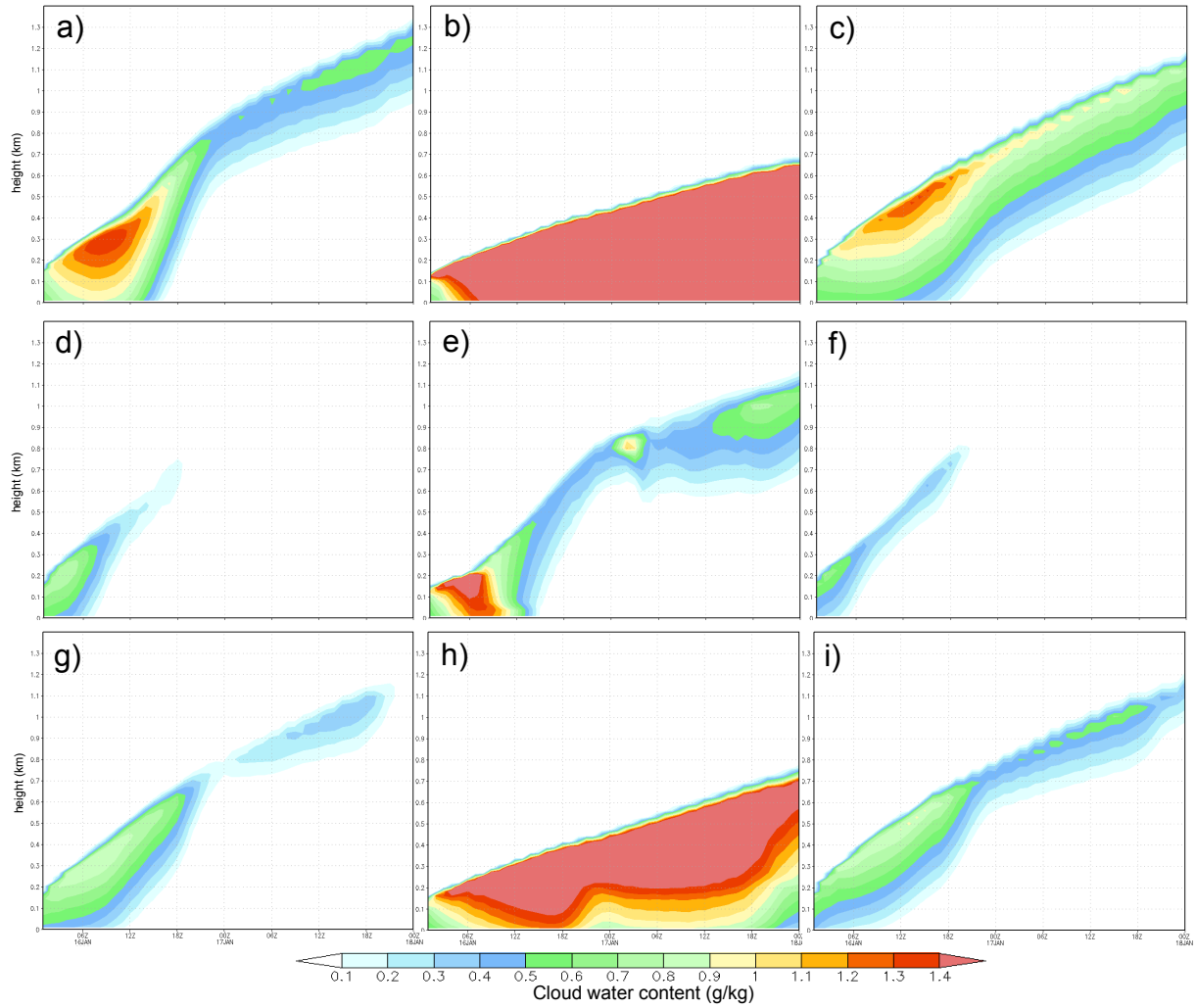

Figure 4.3: Domain average cloud water content (g/kg) for nine 48-hour idealized simulations is shown. LES simulations (dx=dy=33 m) with no PBL parameterization are shown in the left most column (a,d, and g). The coarse grid (dx=dy=12000 m) YSU simulations are shown in the center column (b,e, and h) while the modified YSU (dx=dy=12000 m) runs are in the right most column (c,f, and i). Simulations in row 1 and 3 use the default sounding while row 2 introduces shear (0-15 m/s from the surface to 900 m). Row 1 and 2 use the original physics setup while row 3 alters the microphysics, radiation, and LSM. All simulations use 101 points vertically, with 38 of them lying in the lowest kilometer. The radiation scheme used a typical CV latitude, longitude, and wintertime solar elevation (Jan. 16).

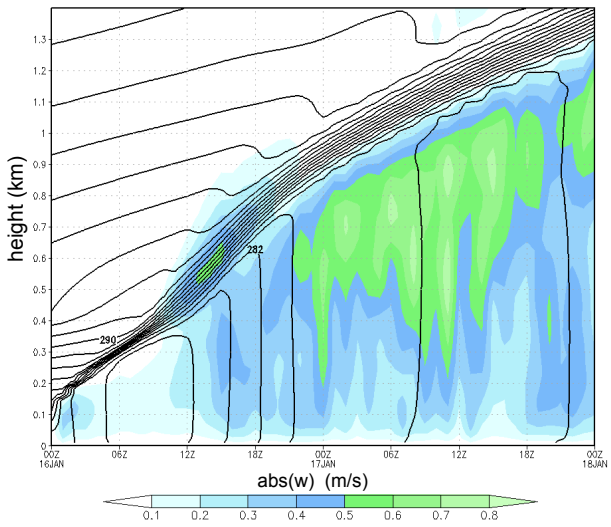

Figure 4.4: Domain average absolute vertical velocity (shaded) and ice-liquid-water potential temperature (contoured) for the LES simulation seen in Fig. 4.3a

first time step to produce fog; although, not long after initialization (roughly 16 hours) it lifts into stratus. Before radiation fog first forms, the profile is indeed stable, that is, the ice-liquid-water potential temperature increases with height. However, as the fog deepens, surface radiational cooling ceases to exist and the cloud top cooling begins to dominate. This continues until the layer becomes unstable[3] which subsequently drives turbulence and the entrainment of drier air.

The unstable fog is not only apparent in our LES simulation (Fig. 4.4) but in our case studies and real world observations (Fig. 4.5). Here, profiler data from two San Joaquin Valley stations, Chowchilla (CCLCA) and Lost Hills (LHSCA), is shown for 16 UTC, 1 Jan. 2009. Since these instruments measure virtual temperature with height coordinates, they are converted to pressure via the standard atmosphere. Next, assuming that the water vapor mixing ratio is equal to that of the saturated mixing ratio, one could calculate the (virtual) equivalent potential temperature. In the foggy boundary layer this is actually a good approximation since the air is already saturated or very nearly so (Fig. 4.1 shows that during this time the average San Joaquin saturation level is approximately 250 m AGL).

[3]Instability causes mixing, and the consequence of mixing is neutrality. Whether we call a layer unstable, neutral, or well mixed is a matter of semantics.

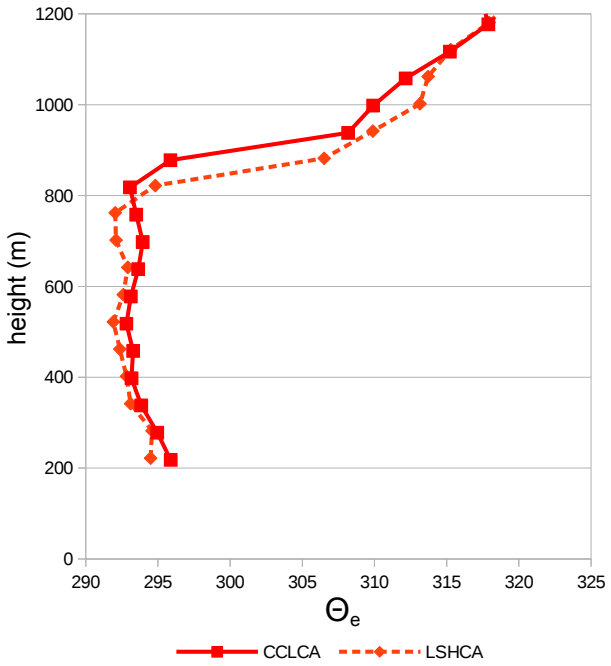

Figure 4.5: Approximate (virtual) equivalent potential temperature is shown for Chowchilla (CCLCA) and Lost Hills (LHSCA), California on 16 UTC, Jan. 1, 2009. Pressures were approximated using the standard atmosphere while the water vapor mixing ratio was assumed to be equal to that of the saturation mixing ratio.

However, above the clearly identified inversion this assumption breaks down.

Inspecting these early morning observations reveal that the foggy boundary layer is nearly moist adiabatic through a depth of 800 m. This is most certainly a reflection that the fog is unstable. It should be noted that below 400 m the profile appears to be super moist adiabatic, however, observations closer to the surface are likely subsaturated and hence inflated due to our saturated assumption. These profiles are by no means unique; in fact, the moist adiabatic profiles are seen day or night, in this event and many others. Not only does this suggest that radiation fog can be unstable, but also that instability during fog is actually quite common in the CV.

This is perplexing because cold pools are always viewed as stable conditions. Additionally, radiation fog will almost always start with a stable profile. It is not until the fog layer is deep enough to shut off the surface radiational cooling can it transition to a unstable, albeit

extremely weak, layer often capped by a stable layer. Because cold pools can exists in two entirely different regimes, that is stable and unstable capped by stable, differentiation between the two is important for discussions and modeling purposes. After all, the turbulence generated by the unstable fog layer produces entrainment and mixing not seen in the typical cold pool. For this reason, we will be referring to these unstable fog layers as *adiabatic cold pools*, reference to the temperature profile they subsequently create.

Besides a near moist neutral sounding, another byproduct of unstable conditions is vertical motions. This is seen in the LES simulation where the weakly unstable layer is able to drive domain averaged thermals on the order of 0.5 m/s (Fig. 4.4). As the fog lifts into stratus, clouds become less opaque allowing more shortwave radiation to reach the surface. Because of this and the continued cloud top cooling, domain averaged vertical motions are stronger towards the end of the simulation. It can be seen that vertical motions are largely confined to the upper portions of the PBL but can extend down near the surface especially when afternoon heating is active.

The fog and stratus simulated here are likely growing faster than what one would expect in nature for two specific reasons. First off, these idealized simulations have no large scale subsidence which is often present in nature during the formation of radiation fog/stratus. Secondly, we are running these cases with nothing to oppose the background radiational cooling. This will cause the simulations to continuously cool, allowing saturation to be reached more easily, and thus lifting the stratus faster than normal. However, since all our idealized simulations are missing subsidence and an opposing heat source to the background radiational cooling, one is still able to compare them directly.

In addition to the LES, a coarse grid simulation was made with the same number of vertical levels (101) but with a horizontal resolution of 12000 m. This required us to activate the YSU PBL scheme since almost all eddies will be unresolved at this scale. Our domain for the coarse grid simulation uses 10 points in each direction, though using a substantially larger (or smaller) domain has no impact on the results.

In Fig. 4.3b one can see the coarse grid, idealized, YSU simulation. Just as in the LES,

clouds form after the first timestep and grow throughout the period. However, one major difference is the growth rate, or another way of looking at the problem, the amount of air entrained. It is also worth noting that even after the two day idealized simulation, the fog has not lifted from the surface. This is in agreement with our real data case (Fig. 4.1), in which the YSU simulation unrealistically failed to lift the ceiling substantially throughout the entire simulation.

4.2.3 The Modified YSU

We believe we have uncovered an important bias in the WRF model concerning fog and stratus forecasts. While the model is able to accurately reproduce the location of fog, it has no skill in forecasting ceiling heights because it has a tendency to never lift it into stratus. Since the societal impact of fog is huge – especially for ground transportation – it is critical that numerical models are able to reasonably forecast the time at which it would lift. Beyond this, ceiling heights are significant to the aviation industry since they directly control the airport acceptance rate. Because of this, it is our goal to revise the boundary layer scheme so that it properly represents the evolution and life cycle of fog in both idealized and real data cases while not impacting performance in other areas and time.

The governing equation for the YSU PBL is as followed:

$$\frac{\partial C}{\partial t} = \frac{\partial}{\partial z}\left[K_c\left(\frac{\partial C}{\partial z} - \gamma_c\right) - \overline{(w'c')}_h\left(\frac{z}{h}\right)^3\right] \tag{4.1}$$

where $C = u, v, \theta, q, q_c, q_i$, the east-west wind component, north-south wind component, potential temperature, water vapor mixing ratio, cloud water mixing ratio, and cloud ice mixing ratio respectively (Hong et al., 2006). h represents the height of the PBL, K_c is the eddy diffusivity coefficient, γ_c is the correction to the local gradient from large scale eddies, and $\overline{(w'c')}_h$ is the flux at the PBL top. Our first revision will involve modifying the eddy diffusion coefficient (Eq. 4.2).

$$K_m = kw_s z\left(1 - \frac{z}{h}\right)^p \tag{4.2}$$

Here k is the von Kármán constant (=0.4), p is the profile shape constant (=2), and w_s is the mixed layer velocity scale, which among other things, is a function of the surface heat flux.

While this particular equation depicts the momentum diffusivity coefficient, it is related to that of heat of moisture via the Prandtl number.

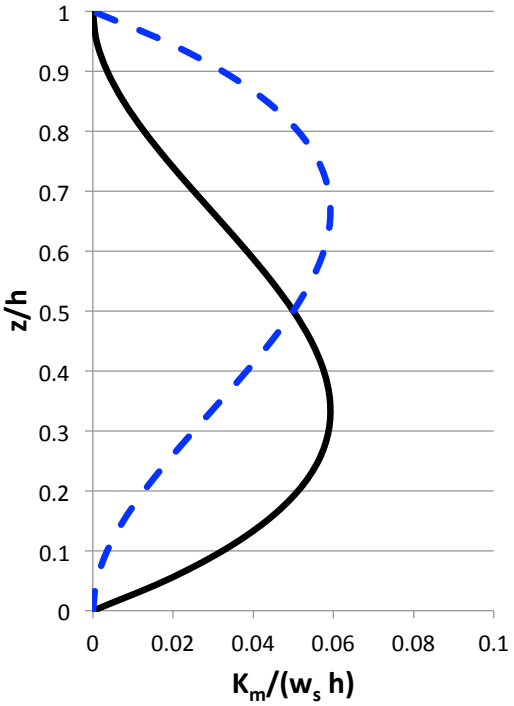

Figure 4.6: The prescribed eddy diffusivity profile (black) for the YSU planetary boundary layer scheme. Term two of the revised eddy diffusivity coefficient (Eq. 4.3) is shown by the dotted blue line.

Normalized by the mixed layer velocity scale (w_s) and the boundary layer height (h), Eq. 4.2 yields the prescribed K profile shown in Fig. 4.6 (black line). For the majority of conditions, thermals originate at the surface and rise throughout the boundary layer; because of this, the prescribed K profile is larger near the surface and substantially smaller near the PBL top. While this works well in a variety of conditions, one could see how it could be problematic for thermals originating near the PBL top: such is the case for the marine/foggy boundary layer where cloud top cooling dominates.

In this case, it may be appropriate to have an additional profile that is *completely reversed* (Fig. 4.6) in order to capture the mixing created by the thermals originating near the PBL top. Mathematically, we have accomplished this by adding in a second term to the eddy

diffusivity coefficient (Eq. 4.3).

$$K_m = kw_s z\left(1-\frac{z}{h}\right)^p + kw_{pbl}(h-z)\left(1-\frac{h-z}{h}\right)^p \tag{4.3}$$

Here, w_{pbl} is formulated the same way as w_s with the exception that it is now a function of the PBL top flux rather than the surface fluxes. While the reversed K profile has accomplished top-down mixing not seen in the original YSU, the exact profile shape may need further refinement (Wyngaard and Brost, 1984; Lock et al., 2000).

In addition, we have modified the boundary layer scheme to enhance the PBL by the ice-liquid-water potential temperature (θ_{il}). Currently, YSU computes the boundary layer height by finding the level where the bulk Richardson number (Rib) exceeds zero (Eq. 4.4).

$$Rib(z) = \frac{g\left[\theta_v(z)-\theta_s\right]z}{\theta_{va}U(z)^2} \tag{4.4}$$

Here, g is the gravitational acceleration due to the earth's mass, $\theta_v(z), \theta_s, \theta_{va}$ are the virtual potential temperatures at height z, the surface thermal, and sigma level one, respectively, and U is the wind speed. The problem here is that in fog or shallow cumulus, the profile goes from dry to moist adiabatic with respect to height. Using the old formulation, virtual potential temperature would classify a moist adiabatic profile as stable (since $[\theta_v(z)-\theta_s] > 0$ in these situations) and would not include it as part of the PBL. However, by enhancing the PBL by θ_{il}, it now recognizes moist adiabatic layers as being part of the boundary layer.

Properly identifying the PBL height is important for calculations like the prescribed K profile in Fig. 4.6. Additionally, the YSU's entrainment term operates using the local inversion at the diagnosed PBL top. Using the old way (θ_v) the PBL top would be located where the profile switched from dry to moist adiabatic. Of course, diagnosing entrainment here would create a meaningless result. However, now with a properly diagnosed PBL the entrainment term operates as designed.

In addition to this, the PBL top flux, $\overline{(w'\theta')}_p$, has been added to the countergradient term:

$$\gamma_c = \frac{b}{w_{so}h}\left(\overline{(w'\theta')}_o + \overline{(w'\theta')}_p\right) \tag{4.5}$$

where $\overline{(w'\theta')}_o$ is the surface thermal flux, b is a coefficient of proportionality, and w_{so} is the mixed layer velocity at $z = 0.5h$. This modification provides consistency for the boundary layer scheme, however, has relatively little impact on results.

Up to this point the YSU has been modified to include a revised diffusivity coefficient, an enhancement of the PBL by θ_{il}, and an additional term to the countergradient. Thus far, these revisions to the YSU PBL have not yet added the physics capable of lifting a fog layer in our Central Valley simulation. It is believed that boundary layer entrainment – at least the formulation used in the YSU (Eq. 4.6) – is the culprit.

$$\overline{(w'\theta'_v)}_h = -0.15 \left(\frac{\theta_v}{g}\right) \frac{w_m^3}{h} \tag{4.6}$$

Here, w_m^3 is the velocity scale based on surface fluxes. For this entrainment term to work correctly, it is critical that the inversion layer be properly identified (as previously discussed). However, the entrainment term is proportional to the velocity scale cubed, which is a function of the surface heat flux. This is a major problem because under fog, the surface heat flux is extremely small and yet is controlling entrainment. Additionally, it has been shown that entrainment can result from turbulence generated by cloud top radiational cooling and be enhanced by evaporative cooling (Nicholls and Turton, 1986; Shao et al., 1997).

For this reason, a revised entrainment term (Eq. 4.7) with a velocity scale based on the PBL top heat flux (w_l^3) was added.

$$\overline{(w'\theta'_v)}_h = -0.15 \left(\frac{\theta_v}{g}\right) \frac{w_m^3}{h} - A \left(\frac{\theta_v}{g}\right) \frac{w_l^3}{h}, \tag{4.7}$$

$$\text{where} \qquad A = 0.2(1 + a_2 E)$$

Here, A is the entrainment efficiency which can have a minimum value of 0.2 while term $a_2 E$ reflects the evaporative enhancement of entrainment (Nicholls and Turton, 1986). In the past, a_2 has been found to be as large as 60 (Nicholls and Turton, 1986) while more recent research suggests a value of 15 may be more appropriate (Bretherton et al., 2007; Stevens et al., 2005; Caldwell et al., 2005). As it will be shown momentarily, our chosen value of

8 seems to reasonably replicate entrainment found in LES simulations. Furthermore, this added entrainment term acts to decrease cloud density by allowing dryer/warmer air above the inversion to infiltrate the boundary layer. This is in contrast to the revised diffusivity profile which acts to increase clouds. Whether the combination of these two terms results in more or less clouds is very much dependent on the event.

It is important to understand that the changes in the modified YSU are active only under adiabatic conditions capped by clouds. This is because in the dry convective boundary layer, the original YSU has all the physics necessary to do bottom-up mixing and entrainment via surface thermals. Top-down mixing would not be appropriate in dry conditions since there is no heat sink at the top of the PBL. However, in the marine layer and under foggy conditions, we often get an adiabatic profile capped by a cloud (i.e. a heat sink). It is only under these conditions that our top-down mixing/entrainment becomes active, which works in conjunction with the original bottom-up mixing/entrainment.

Turning back to the LES simulation in Fig. 4.3a, we have added a coarse grid simulation using the modified YSU (Fig. 4.3c). Here, one can see that the parameterized PBL actually looks very similar to that of the LES simulation. When comparing to the original YSU we see that it no longer has fog throughout the entire simulation, but only the first 18 hours.

Using the same sounding, but in a higher shear environment (0 - 15 m/s wind from the surface to 900 m), the experiment was repeated (Fig. 4.3d-f). Here, the LES simulation (Fig. 4.3d) quickly lifts the fog into stratus and completely eliminates it by 18UTC. When comparing this to the modified YSU (Fig. 4.3f), results are nearly identical. This is not the case for the original YSU which is slower to lift the fog and maintains stratus throughout the extended period.

Figures 4.3g-i use the original sounding but vary the microphysics, radiation, and LSM, to assess sensitivity to these factors. Here one can observe that the LES simulation (Fig. 4.3g) is more or less the same with subtle differences. Additionally, the same is true for the modified YSU (Fig. 4.3i) except it appears to even closer replicate the LES simulation. Unsurprisingly, the original YSU (Fig. 4.3h) struggles to even lift the fog into stratus. The

purpose of repeating such experiments with different physics and environmental soundings was to show that the modified YSU is not perfect but can handle a variety of different environments more or less properly. We have since ran several more experiments with a variety of initial conditions and perturbations (not shown) all concluding that the modified YSU is able to successfully capture the evolution of these adiabatic cold pools.

Looking at the end of the original 48-hour simulation (Fig. 4.3a) one can observe that the PBL heights from the modified YSU and LES are just under 1.3 km while the original YSU is around 0.6 km. These particular simulations use 101 model levels, which translates into 38 levels below one kilometer. In order to understand how the entrainment rate changes with vertical resolution, many tests were performed with various model levels and plotted in Fig. 4.7 top.

Here, one can observe a relationship between the number of model levels below 1 km and the height of the PBL after 48 hours. Since all simulations were initialized with the same sounding, the PBL height is proportional to the entrainment rate. The overall increase in PBL heights for the modified YSU across all vertical resolution experiments is smaller (259 m or 29%) than the YSU (306 m or 78%) and does not necessarily increase for increasing model levels. Nonetheless, using more than 38 model levels below 1 km does not enhance the PBL substantially. It is for this reason we have chosen to create the LES with 38 model levels below 1 km which agrees fairly well with the modified YSU (Fig. 4.3 and 4.7). It should be noted that the leftmost point in Fig. 4.7 has only 8 levels below 1 km which matches the vertical grid structure provided by real.exe. As described earlier, we have chosen not to use the default grid in our real case studies, but a modified grid that includes 19 levels below one kilometer. While it may be desirable to include more levels (say 38), 19 provided a way to be numerically stable without being computationally intensive. The relationship between PBL height and model levels was also found in our real case studies (not shown).

Next it is important to understand how the entrainment rate changes with horizontal resolution as seen in bottom panel of Fig. 4.7. Here, the YSU trends slowly upwards (more entrainment) with increasing resolution. It is hypothesized that as the horizontal grid gets smaller, more turbulence originating near the fog top is resolved, and thus more entrainment

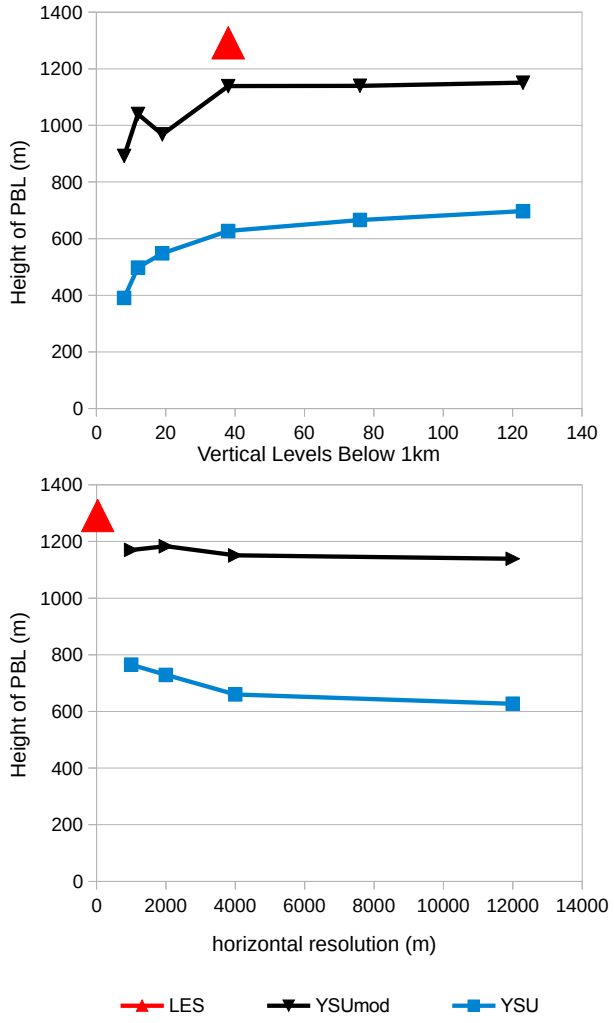

Figure 4.7: PBL heights (hour 48) from idealized vertical (top) and horizontal (bottom) resolution tests are plotted for the YSU (blue) and modified YSU (black). For reference, the LES simulation is plotted in red. Vertical resolution tests use a horizontal resolution of 12,000 m while horizontal resolution tests use a vertical resolution of 101 levels (38 levels below 1km).

occurs. One would expect (or at least hope) for a convergence between the YSU and LES as the grid scales approach unity, however, additional tests reveal this is not the case. In contrast, the modified YSU behaves entirely different. Since it has a term to parameterize entrainment from thermals/turbulences originating near the PBL top, it is nearly able to correctly forecast PBL heights with coarse horizontal resolution. As one moves to finer

resolution and approaches the LES, the PBL heights hardly change, meaning there is little dependence on horizontal resolution.

4.2.4 Case Studies

Seeing that the modified YSU performs exceptionally well in an idealized setting is encouraging, however, the author feels that it is as equally important to demonstrate improvements in real cases while not degrading performance in other areas and time. As previously stated, changes in the modified YSU take place only under an adiabatic profile capped by a cloud. Only if these conditions are satisfied can the revised scheme give an answer different from the original. For example, simulations of the dry convective boundary layer would produce results identical to the original code. While we do not demonstrate this directly, the initial hours of our simulations in this section will reveal that the modified YSU behaves exactly like the original, that is, until fog forms or changes from the marine layer advect their way into the domain.

Presented in Fig. 4.8 is the temperature and dew point (top) from Dec. 2008 in addition to the number of stations with ceilings less than 1000 m (bottom) and their respective heights. One can observe that for the first two days, temperatures and dew points from the modified YSU are nearly identical to its original formulation. It is not until the night of the 31st and into the day on the 1st do simulations begin to diverge. Following this period the original YSU has a colder and less accurate temperature while the modified YSU is very close to observations.

Looking at ceiling heights (bottom) one can observe that they are similar, at least up until the 1st. It is here where the modified YSU begins to entrain more air – which was reflected in warmer temperatures – and lift ceilings. This continues for the rest of the simulation which closely follows observations. As for the original YSU, ceiling heights beyond the 31st fluctuate between the first sigma level (18 m), the lowest possible value, and 90 m.

This behavior is by no means unique, but can be further demonstrated by looking at the Jan. 13, 2011 Tule fog event (Fig. 4.9a). Here, the YSU and modified YSU have diagnostics

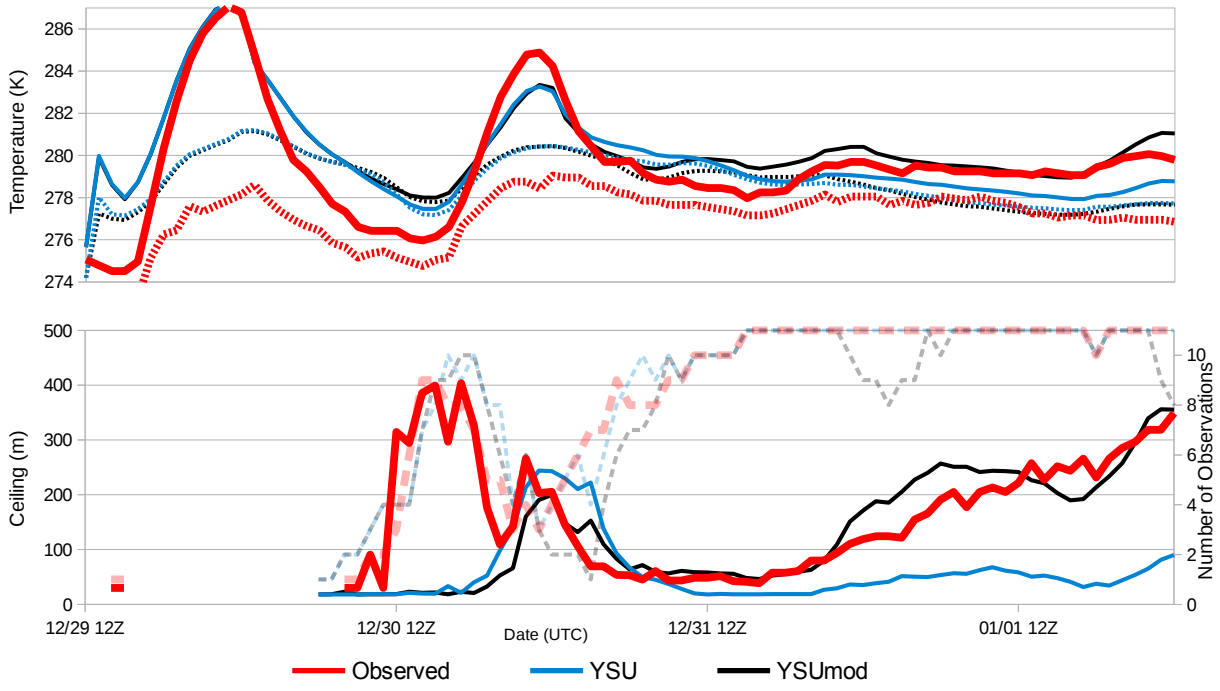

Figure 4.8: Same as Fig. 4.1 but with the modified YSU added.

that are identical until the cloud capped adiabatic layer develops on the 14th. At this point, things begin to deviate, but not substantially. As we integrate through the night of the 15th and into the day of the 16th, one will find that the YSU is unable to lift the forecasted temperature beyond the observed dew point. This is an artifact of its inability to entrain air due to cloud top turbulence, which is also reflected in its extremely low ceiling heights (Fig. 4.9b). In comparison, the modified YSU's temperatures and dew points accurately reproduce observations, albeit a degree too cold at times. Furthermore, the ceiling height, while not perfect, is substantially better and is able to capture the diurnal variation.

It is interesting to note that the number of forecasted observations with ceilings less than 1000 m dips dramatically during the afternoon hours on the 16th and 17th but does not occur in the observations; this is evidence that the modified YSU is burning off clouds too early. This is perplexing because the average temperature (from all 10 stations) does not exceed the observed, nor does the ceiling height ever get too high. This may indicate a boundary layer that is too shallow, but not necessarily caused by the PBL itself. Reasons why this

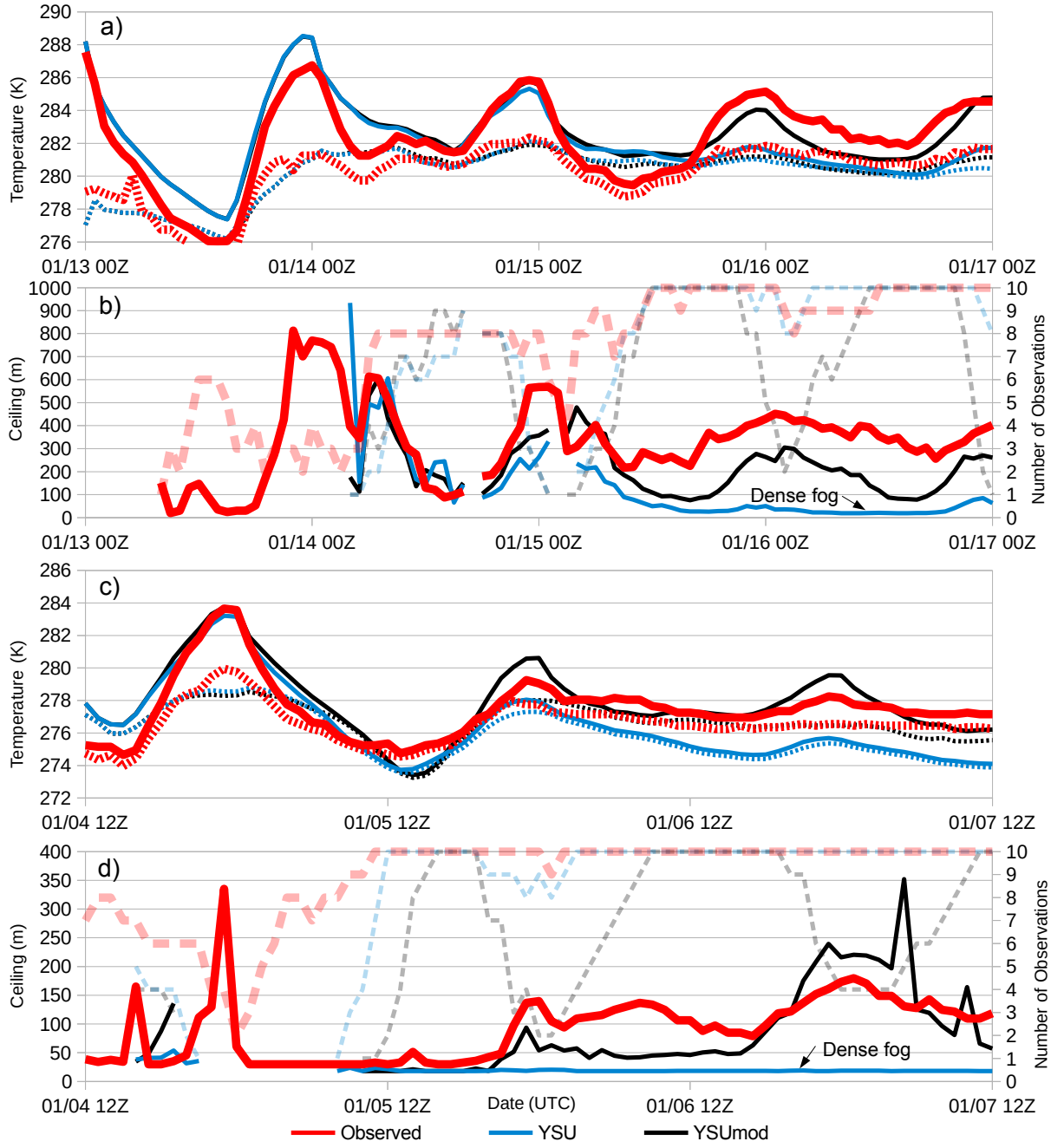

Figure 4.9: Same as Fig. 4.8 but for the Jan. 13, 2011 (a and b) and Jan. 4, 2011 (c and d) events.

might occur include, but are not limited to: the microphysics, radiation, land surface model, and initialization.

The Jan. 4, 2011 event tells the same story for the original YSU scheme Fig. 4.9c,d.

Beyond the formation of the fog, temperatures are too cold due to a lack of entrainment, and ceilings are too low. Here, the original YSU is actually producing fog (as opposed to stratus) throughout the extended period as it is unable to lift it beyond the first model level. Observations and the modified YSU lift the fog roughly 36 hours before the end of the simulation.

Unfortunately, the modified YSU again burns off too much fog during the day of the 6th, however, there may be a good reason for this. If one inspects the night of the 5th, the number of observed stations reporting fog quickly ramps up after sunset. It is not until roughly 12 hours later that the modified YSU begins to develop fog for the entire San Joaquin Valley. Since the fog formed too late, perhaps for a number of reasons, one could argue that it would be susceptible of burning off too early, as it does on the 6th. After all, the more time fog has to form the deeper and less susceptible (to an extent) it is to burning off via short wave radiation. This is in contrast to the original YSU which does not mix out the fog despite a late onset. Because this scheme can only entrain air from the surface fluxes, it will entrain little, if any, under foggy conditions. Of course, if you are entraining little to no air one would expect it to be substantially more difficult to burn off the protected fog. Thus, it appears to be getting the right answer (in terms of fog coverage) for the wrong reasons.

CHAPTER 5

Conclusions

California's Central Valley is home to many urbanized and agricultural areas which are often plagued by diurnal and persistent cold pools. Forecasting these events has been challenging due to our lack of understanding in the governing principals which drive the evolution and life cycle of cold pools. Presented in this thesis are ideas and results that not only refine our knowledge of distinct atmospheric processes, but improvements to numerical modeling to forecast such events.

First and foremost, it was shown that diffusion operating on model levels must be reconsidered. Once thought of as a valuable numerical method to perform subgrid scale mixing, diffusion is now clearly identified as a scheme that substantially degrades, if not completely eliminates, the model's ability to forecast topographically confined cold pools. It is now understood that even the marine layer, when butting up against the terrain of California's coast, can be blunderingly modified by the scheme's unphysical calculations.

It is important to understand that these errors can extend beyond model diffusion and into the 6th order numerical filter if it also operates on model levels (such is the case in the WRF model). Surprisingly, the negative impact of the numerical filter on simulations was found to be almost equally severe as model diffusion. Furthermore, the recommended (by the WRF team) monotonic and positive definite filter eroded more fog than the alternative (not positive definite nor monotonic) in our particular case. However, there could very will be situations where the reverse is true. These problems demonstrate the lack of understanding of important processes, or at least their sensitivity, and our rush to implement solutions that are extremely likely doing more harm than good. Attempting to model cold pools or any phenomena with terrain, especially in stagnant conditions, with schemes operating on model

levels is ill advised and can ultimately lead to highly erroneous and dramatically different conclusions.

Motivated by this work, other options are currently being explored. Since diffusion operating in physical space is numerically unstable, one such workaround was to deactivate or decrease its magnitude along sharply sloping terrain. This solution was implemented in WRF version 3.6 and appears to be an acceptable way to circumvent the problem. However, diffusion near the sidewall, a potentially important process, cannot be experimented with thus making it impossible to be completely confident in this fix. However, it is much better than the alternative. As of now, the 6th order filter still operates on model levels and is susceptible to such problems; consequently, it is recommended to avoid, if possible, all 6th order numerical filters.

When modeling cold pools involving fog one needs to consider a number of other processes, some of which are parameterized in today's numerical models. These include processes such as vertical diffusion and entrainment done by the planetary boundary layer. However, a widely used scheme such as the YSU PBL only considers the effects of surface fluxes on boundary layer physics. Here, we are specifically referring to surface fluxes and their use in the parameterization of every important process including, but not limited to: the prescribed K profile, the countergradient, and entrainment.

Our work demonstrated that processes far above the earth's surface can contribute, often much more substantially, to the evolution of and ultimate demise of the foggy boundary layer. It was found that cooling at the fog top quickly establishes a moist adiabatic profile which subsequently drives turbulence and negatively buoyant thermals. Under these conditions the original YSU PBL becomes stagnant since these processes are not governed by surface fluxes but rather by the unconsidered cloud top cooling. Additionally, there is little to no entrainment in the original YSU which ultimately results in the model unable to lift fog into stratus.

In order to remedy this a reversed K profile, as a function of the cloud top flux, was added in addition to a modified countergradient term to account for the mixing done by

negatively buoyant thermals. While these two modifications did not change the persistent fog forecast, it allowed for a properly mixed PBL which can have important consequences. Specifically, more mixing, most notably over the marine boundary layer, can create more or less clouds. While this was not demonstrated directly, cases in which this was apparent were found.

Furthermore, to tackle the persistence issue, two other modifications were found to be absolutely critical. First, the PBL needed to be enhanced by the ice-liquid-water potential temperature – rather than just the virtual potential temperature – to accurately diagnose its height under conditions that deviate from dry adiabatic. Without this, the PBL would consistently identify moist adiabatic profiles as stable and define this layer as the inversion for the entrainment calculation. Of course, this would severely underestimate entrainment not only because this was not the inversion, but also because the calculation only considered surface fluxes.

This led to the last modification which included the addition of PBL top fluxes in the entrainment calculation. This was done because turbulence generated by the fog top cooling often produces more entrainment than thermals originating near the earth's surface. Through the inclusion of this term, all problems associated with the persistent fog were alleviated if not completely eliminated. This has allowed the numerical model to create a more meaningful fog to stratus forecast that will be of use to both ground and air transportation.

Unfortunately, there are still difficulties pertaining to fog and stratus longevity. In the longer simulations, both the regular and modified YSU have a tendency to burn it off too quickly. While this could be related to a number of variables, certain aspects should be investigated in future work including: aerosols, microphysics, and radiation to name a few. These three in particular can substantially modify clouds and their optical properties which may ultimately be causing problems with the early burn off.

However, in the absence of clouds, cold pools in the Central Valley were found to have a dry bias that grew with time. This suggests that the early burn off may have nothing to do with aerosols, microphysics, or radiation, but with fundamental deficiencies found elsewhere

in the model. It was shown that deactivating diffusion alleviated, though did not completely remove, the dry bias in cloud-free cold pools. Additional modifications such as adjusting the lowest model level closer to the surface, in addition to activating IZ0TLND, further improved the dry bias by increasing the latent heat flux in the surrounding terrain.

Additional research is needed to verify that the larger fluxes observed in the online/offline simulations are in fact, realistic. At this point, it does appear that daytime evaporation rates are too large while nighttime values are debatable. With that being said, more consistent evaporation rates between online/offline simulations are needed since it was found that the online model under-evaporates in forested regions. Certainly, the underlying goal of spinning models offline is to be consistent, yet consistency was never achieved. Understanding the exact reasons why is desirable and ongoing.

Nonetheless, it was through these modifications one was able to understand the importance of drainage flows and their influence on CV dew points. Most specifically, nighttime evaporation in the surrounding terrain was important since the majority of the air flows downslope and out over the valley. This means if drainage flows were drier than observations in the foothills, the bias would translate to stations in the CV. In contrast, daytime evaporation in the surrounding terrain was of much less importance owing to the fact that any additional moisture added to the larger, convective boundary layer would be diluted and in cases, too far aloft to influence the CV.

Adjusting the height of the lowest model level had a dramatic impact on nighttime evaporation despite having little effect during the day. It was later shown in idealized simulations that making the first sigma level thinner would make it more responsive to surface fluxes. Consequently, the layer could become colder and drive stronger drainage flows that ultimately produce larger evaporation rates. Now, whether or not the stronger flows produced by a thinner model level is correct, it does point out current resolution constraints by using the coarse (default) vertical grid.

In addition to this, idealized simulations assisted in demonstrating that drainage flows directly cool air above the valley center while indirectly cooling it near the surface. It

was found that in a valley, compared to flat terrain, the air aloft becomes substantially cooler than it would be otherwise due to drainage flows detaching from the sidewalls upon reaching the stable layer. This means that the air above the center of the valley was cooled (directly) by the sidewalls. Since the air above the surface is cooler due to direct cooling, this reduced the downward longwave radiation which subsequently lowered (indirectly) the surface temperatures. However, in our cases the indirect cooling effects were much smaller in magnitude.

Another important side effect of drainage flows is their ability to undercut and lift large volumes of air. While this may seem trivial, it was shown that this helps moisten the atmosphere above the surface which could potentially lead to an elevated cloud deck. Below this, in the portions of the valley where the drainage flows are directly observed, the dew points are often lower (assuming dew points decrease with height) since the air originated higher up on the sidewalls.

Soil moisture was shown to have important consequences not only in the idealized simulations, but also in real data cases. Idealized simulations showed that an increase in soil moisture could increase absolute humidity in drainage flows while simultaneously lowering the temperature (due to a cooler surface). In real data cases, CV soil initializations from different sources had a wide variety of values which directly related to the overall dew point bias. However, even with the wettest soils, the previously mentioned CV dry bias was still apparent across all model simulations.

This led to the hypothesis that the widespread irrigated croplands in California's Central Valley may play at least some role in low level moisture. Upon building an irrigation model from the ground up, it was discovered that there was little influence from crops on CV dew points, that is, at least for winter. However, summertime dew points, in addition to temperatures and boundary layer heights, were substantially altered by the introduction of this anthropogenic moisture.

Just as with the early burn off with fog and the dew point bias in cloud free cold pools, summertime dew points had a dry bias that amplified itself with time. It was shown that

implementing an irrigation model could only remedy (at least for summer) about half the bias. While the remaining bias may seem correlated to those seen in other seasons, they are likely unrelated.

It was shown that in the summer, the cool marine air near the surface was blocked by the coastal range for the majority of the valley. This allowed air from upstream and higher aloft – whose potential temperature is lower than the CV – to routinely crash down to the surface of the valley on its westward journey. This particular flow pattern is unique to this time of year since a large temperature gradient is required. Consequently, the remaining half of the summertime CV moisture bias is likely related to the conditions upstream and further aloft while biases seen in winter are influenced by drainage flows and perhaps other local effects (i.e. underestimating the surface moisture).

Furthermore, it is clear that using schemes which adjust soil moisture to account for irrigation (NoahFC) within a grid cell, can produce desirable results. However, determining how much water should be applied to each grid cell is a daunting task. This is because irrigation depends not only on crop type but also how much irrigated land occupies a given grid cell. For these reasons, using a scheme which can perform sub-tiling, in order to account for all types of landuse within a grid cell, is important. The irrigation scheme developed in this thesis could only account for two types of landuse within a grid cell (irrigated and idle cropland), although, modifying it to account for three is desirable.

While this thesis has focused specifically on fog events occurring in California's Central Valley, positive changes to the marine boundary layer have also been noticed with the modified YSU though not extensively verified. This is an area of future work that shares many similarities with the foggy boundary layer which in and of itself has been substantially improved.

It is through these modifications that we have been able to dramatically enhance the forecasting ability of the WRF model. More specifically, the YSU PBL is now able to successfully model the evolution and life cycle of fog while not degrading the performance in other areas and time. This has accomplished a model of more general use and applicability

which will benefit not only the modeling community but society at large. However, it was only through our understanding that such improvements could be made thus our pursuit of knowledge should not go overlooked. It is with great pleasure I am able to give a more enriched and refined, however small, understanding of our atmosphere and the fascinating processes which govern it.

Appendix A List of Acronyms

ASOS	Automated Surface Observing System
AWOS	Automated Weather Observing System
BCRMSE	Bias Corrected Root Mean Squared Errors
CASES	Cooperative Atmospheric Surface Exchange Study
CDFA	California Department of Food and Agriculture
CDL	Cropland Data Layer
CIMIS	California Irrigation Management Information System
CV	Central Valley
ENIAC	Electronic Numerical Integrator and Computer
EPA	Environmental Protection Agency
ERA-Interim	European Reanalysis Interim
FAO	Food and Agriculture Organization
HRLDAS	High Resolution Land Data Assimilation System
KF	Kain-Fritsch
LES	Large Eddy Simulation
LSM	Land Surface Model
MADIS	Meteorological Assimilation Data Ingest System
MET	Model Evaluation Tools
MM5	Fifth-Generation Penn State/NCAR Mesoscale Model
MODIS	Moderate Resolution Imaging Spectroradiometer
NAAQS	National Ambient Air Quality Standard
NAM	North American Mesoscale Model
NARR	North American Regional Reanalysis
NASA	National Aeronautics and Space Administration
NASS	National Agriculture Statistics Service
NCAR	National Center for Atmospheric Research

NLDAS	North American Land Data Assimilation System
PBL	Planetary Boundary Layer
PM2.5	Particulate Matter with diameter <2.5 μm
RAWS	Remote Automatic Weather Stations
RDA	Research Data Archive
RH	Relative Humidity
RRTM	Rapid Radiative Transfer Model
TD	5-layer Thermal Diffusion
USDA	United States Department of Agriculture
USGS	United States Geological Survey
WDM5	WRF Double Moment, 5-class scheme
WRF	Weather Research and Forecasting
YSU	Yonsei University

Appendix B Model Physics

Model Physics	Option	Chapter Used	Source
PBL	YSU	Ch. 2,3,4	Hong et al. (2006)
	Modified YSU	Ch. 4	our addition
LSM	Noah	Ch. 2,3,4	Chen et al. (1996)
	NoahAG	Ch. 3	our addition
	NoahFC	Ch. 3	our addition
	TD	Ch. 2.3	Dudhia (1996)
Surface Layer	Monin-Obukhov	Ch. 2,3,4	Obukhov (1946), Monin and Obukhov (1954)
Microphysics	WDM5	Ch. 4	Lim and Hong (2010)
	Lin	Ch. 2,3	Lin et al. (1983)
Shortwave Radiation	Dudhia	Ch. 2,3	Dudhia (1989)
	New Goddard	Ch. 4	Chou and Suarez (1999)
Longwave Radiation	RRTM	Ch. 2,3	Mlawer et al. (1997)
	New Goddard	Ch. 4	Chou and Suarez (1999)
Cumulus Scheme	KF (domains 1,2 only)	Ch. 2,3,4	Kain (2004)
Thermal Roughness	IZOTLND	Ch. 2	Chen and Zhang (2009)

Bibliography

Abbe, C., 1901: The physical basis of long-range weather forecasts. 551–61 pp.

Adegoke, J. O., R. A. Pielke, J. Eastman, R. Mahmood, and K. G. Hubbard, 2003: Impact of irrigation on midsummer surface fluxes and temperature under dry synoptic conditions: A regional atmospheric model study of the u.s. high plains. **131**, 556–564.

Avery, L., 2011: Challenges of meteorological and photochemical modeling of utahs wintertime cold pools. Western Meteorological, Emissions, and Air Quality Modeling Workshop, Boulder, CO.

Baker, K. R., H. Simon, and J. T. Kelly, 2011: Challenges to modeling "cold pool" meteorology associated with high pollution episodes. *Environmental Science and Technology*, **45(17)**, 7118–9.

Bergot, T., E. Terradellas, J. Cuxart, A. Mira, O. Liechti, M. Mueller, and N. W. Nielsen, 2007: Intercomparison of single-column numerical models for the prediction of radiation fog. *Journal of Applied Meteorology and Climatology*, **46**, 504–521.

Billings, B. J., V. Grubišić, and R. D. Borys, 2006: Maintenance of a mountain valley cold pool: A numerical study. *Monthly Weather Review*, **134**, 2266–2278.

Bjerknes, V., 1904: Das problem der wettervorhersage, betrachtet vom standpunkte der mechanik und der physik, translation by y. mintz: The problem of weather forecasting as a problem in mechanics and physics. los angeles, 1954. *Meteor. Zeit.*, **21**, 1–7.

Bodine, D., P. M. Klein, S. C. Arms, and A. Shapiro, 2009: Variability of surface air temperature over gently sloped terrain. *Journal of Applied Meteorology and Climatology*, **48**, 1117–1141.

Bretherton, C. S., P. N. Blossey, and J. Uchida, 2007: Cloud droplet sedimentation, entrainment efficiency, and subtropical stratocumulus albedo. *Geophysical Research Letters*, **34**.

Caldwell, P., C. Bretherton, and R. Wood, 2005: Mixed-layer budget analysis of the diurnal cycle of entrainment in se pacific stratocumulus. *J. Atmos. Sci*, **62**, 3775–3791.

CDFA, 2013: Agricultural statistical overview. URL `http://www.cdfa.ca.gov/statistics/pdfs/2013/AgStatsOverview.pdf`.

Chen, F. and R. Avissar, 1994: Impact of land-surface moisture variability on local shallow convective cumulus and precipitation in large-scale models. *J. Appl. Meteor.*, **33**, 1382–1401.

Chen, F. and Y. Zhang, 2009: On the coupling strength between the land surface and the atmosphere: From viewpoint of surface exchange coefficients. *Geophys. Res. Lett.*, **36**, L10 404, doi:10.1029/2009GL037 980.

Chen, F., et al., 1996: Modeling of land-surface evaporation by fourschemes and comparison with fife observations. *J. Geophys. Res*, **101**, 7251–7268.

Chou, M.-D. and M. J. Suarez, 1999: A solar radiation parameterization (clir-ad-sw) developed at goddard climate and radiation branch for atmo-spheric studies, goddard space flight center, greenbelt. *NASA Tech.Memo.*, TM–1999–104 606.

Clements, C. B., C. D. Whiteman, and J. D. Horel, 2003: Cold-air-pool structure and evolution in a mountain basin: Peter sinks, utah. *Journal of Applied Meteorology*, **42**, 752–768.

Coleman, R. F., J. F. Drake, M. D. McAtee, and L. O. Belsma, 2010: Anthropogenic moisture effects on wrf summertime surface temperature and mixing ratio forecast skill in southern california. **25**, 1522–1535.

Daly, C., D. Conklin, and M. Unsworth, 2009: Local atmospheric decoupling in complex topography alters climate change impacts. *International Journal of Climatology*, **30**, 1857–1864.

Dudhia, J., 1989: Numerical study of convection observed during the winter monsoon experiment using a mesoscale two-dimensional model. *J. Atmos. Sci.*, **46**, 3077–3107.

Dudhia, J., 1996: A multi-layer soil temperature model for mm5. Preprints, Sixth PSU/NCAR Mesoscale Model Users Workshop, Boulder, CO, PSU/NCAR, 4950.

FAO, 1998: *Crop evapotranspiration - Guidelines for computing crop water requirements - FAO Irrigation and drainage paper 56*. Food and Agriculture Organization of the United Nations Rome.

Fovell, R. G., K. L. Corbosiero, A. Seifert, and K. Liou, 2010: Impact of cloudradiative processes on hurricane track. *GEOPHYSICAL RESEARCH LETTERS*, **37**, L07 808, doi:10.1029/2010GL042 691.

Fovell, R. G. and H. Su, 2007: Impact of cloud microphysics on hurricane track forecasts. *GEOPHYSICAL RESEARCH LETTERS*, **34**, L24 810, doi:10.1029/2007GL031 723.

Gillies, R. R., S. Wang, and M. R. Booth, 2010: Atmospheric scale interaction on wintertime intermountain west low-level inversions. *Weather and Forecasting*, **25**, 1196–1210.

Gudiksen, P. H., J. M. L. Jr., C. W. King, D. Ruffieux, and W. D. Neff, 1992: Measurements and modeling of the effects of ambient meteorology on nocturnal drainage flows. *Journal of Applied Meteorology*, **31**, 1023–1032.

Gustavsson, T., M. Karlsson, J. Bogren, and S. Lindqvist, 1998: Development of temperature patterns during clear nights. *Journal of Applied Meteorology*, **37**, 559–571.

Haddeland, I., D. P. Lettenmaier, and T. Skaugen, 2006: Effects of irrigation on the water and energy balances of the colorado and mekong river basins. *Journal of Hydrology*, **324**, 210–223.

Harding, K. J. and P. K. Snyder, 2012: Modeling the atmospheric response to irrigation in the great plains. part i: General impacts on precipitation and the energy budget. *Journal of Hydrometeorology*, **13**, 1667–1686.

Holets, S. and R. N. Swanson, 1981: High-inversion fog episodes in central california. *Journal of Applied Meteorology*, **20**, 890–899.

Hong, S.-Y., Y. Noh, and J. Dudhia, 2006: A new vertical diffusion package with an explicit treatment of entrainment processes. *Monthly Weather Review*, **134**, 2318–2341.

Hootman, B. W. and W. Blumen, 1983: Analysis of nighttime drainage winds in boulder, colorado during 1980. *Monthly Weather Review*, **111**, 1052–1061.

Hunt, E. D., J. B. Basara, and C. R. Morgan, 2007: Significant inversions and rapid in situ cooling at a well-sited oklahoma mesonet station. **46**, 353–367.

Kain, J. S., 2004: The kainfritsch convective parameterization: An update. *J. Appl. Meteor.*, **43**, 170–181.

Kanamaru, H. and M. Kanamitsu, 2008: Model diagnosis of nighttime minimum temperature warming during summer due to irrigation in the california central valley. *Journal of Hydrometeorology*, **9**, 1061–1072.

Katurji, M. and S. Zhong, 2012: The influence of topography and ambient stability on the characteristics of cold-air pools: a numerical investigation. *Journal of Applied Meteorology and Climatology*, **51**, 1740–1749.

Kueppers, L. M., M. A. Snyder, and L. C. Sloan, 2007: Irrigation cooling effect: Regional climate forcing by land-use change. *Geophysical Research Letters*, **34**.

Lazo, J. K., M. Lawson, P. H. Larsen, and D. M. Waldman, 2011: U.S. economic sensitivity to weather variability. *Bulletin of the American Meteorological Society*, **92 (6)**, 709–720.

LeMone, M. A., K. Ikeda, R. L. Grossman, and M. W. Rotach, 2003: Horizontal variability of 2-m temperature at night during cases-97. *Journal of the Atmospheric Sciences*, **60**, 2431–2449.

Lim, K.-S. S. and S.-Y. Hong, 2010: Development of an effective double-moment cloud microphysics scheme with prognostic cloud condensation nuclei (ccn) for weather and climate models. *Monthly Weather Review*, **138**, 1587–1612.

Lin, Y.-L., R. D. Farley, and H. D. Orville, 1983: Bulk parameterization of the snow field in a cloud model. *Journal of Climate and Applied Meteorology*, **22**, 1065–1092.

Lock, A. P., A. R. Brown, M. R. Bush, G. M. Martin, and R. N. B. Smith, 2000: A new boundary layer mixing scheme. part i: Scheme description and single-column model tests. *Monthly Weather Review*, **128**, 3187–3199.

Lui, M. and J. J. Carroll, 1996: A high-resolution air pollution model suitable for dispersion studies in complex terrain. *Mon. Wea. Rev.*, **124**, 2396–2409.

Lynch, P., 2006: *The Emergence of Numerical Weather Prediction: Richardsons Dream*. Cambridge University Press, 279pp pp.

Lynch, P., 2008: The origins of computer weather prediction and climate modeling. *Journal of Computational Physics*, **227**, 3431–3444.

Lyons, R., H. A. Panofsky, and S. Wollaston, 1964: The critical richardson number and its implications for forecast problems. *Journal of Applied Meteorology*, **3**, 136–142.

Mahrt, D. Vickers, R. Nakamura, M. R. Soler, J. L. Sun, S. Burns, and D. H. Lenschow, 2001: Shallow drainage flows. *Boundary Layer Meteorology*, **101**, 243–260.

Marcella, M. P. and E. A. Eltahir, expeced 2013: Introducing an irrigation scheme to a regional climate model: A case study over west africa. *Journal of Climate*, **27**, 5708–5723.

Mlawer, E. J., S. J. Taubman, P. D. Brown, M. J. Iacono, and S. A. Clough, 1997: Radiative transfer for inhomogeneous atmospheres: Rrtm, a validated correlated-k model for the longwave. *Journal of Geophysical Research*, **102**, 16 663–16 682.

Monin, A. S. and A. M. Obukhov, 1954: Basic laws of turulent mixing in the atmosphere near the ground. *Tr. Inst. Teor. Geofiz. Akad. Nauk SSSR*, **24**, 1963–1987.

Neff, W. D. and C. W. King, 1989: The accumulation and pooling of drainage flows in a large basin. *Journal of Applied Meteorology*, **28**, 518–529.

Nicholls, S. and J. Turton, 1986: Observational study of the structure of stratiform cloud layers. part II: Entrainment. *Quart. J. Roy. Meteor. Soc*, **112**, 461–480.

Obukhov, A. M., 1946: Turbulence in thermally non-homogeneous atmosphere. *Tr. Inst. Teor. Geofiz. Akad. Nauk SSSR*, **1**, 95–115.

Ozdogan, M. and G. Gutman, 2008: A new methodology to map irrigated areas using multi-temporal modis and ancillary data: An application example in the continental. *US. Remote Sens. Environ*, **112**, 3520–3537.

Ozdogan, M., M. Rodell, H. K. Beaudoing, and D. L. Toll, 2010: Simulating the effects of irrigation over the united states in a land surface model based on satellite-derived agricultural data. *Journal of Hydrometeorology*, **11**, 171–184.

Pleim, J. E. and A. Xiu, 1995: Development and testing of a surface flux and planetary boundary layer model for application in mesoscale models. *J. Appl. Meteor.*, **34**, 16–32.

Pleim, J. E. and A. Xiu, 2003: Development of a land surface model. part ii: Data assimilation. *J. Appl. Meteor.*, **42**, 1811–1822.

Rajeevan, M., A. Kesarkar, S. B. Thampi, T. N. Rao, B. Radhakrishna, and M. Rajasekhar, 2010: Sensitivity of wrf cloud microphysics to simulations of a severe thunderstorm event over southeast india. *Annales Geophysicae*, **28**, 603–619.

Reilly, T. E., K. F. Dennehy, W. M. Alley, and W. L. Cunningham, 2008: Ground-water availability in the united states. U.S. Geological Survey Circular 1323, 70 p., URL `http://pubs.usgs.gov/circ/1323/`.

Richardson, L. F., 1922: *Weather Prediction by Numerical Process*. Cambridge University Press Cambridge, 187 pp.

Ryerson, W. R., 2012: Toward improving short-range fog prediction in data-denied areas using the air force weather agency mesoscale ensemble. Ph.D. thesis, Naval Postgraduate School, Monterey, California.

Shao, Q., D. A. Randall, C. H. Moeng, and R. E. Dickinson, 1997: A method to determine the amounts of cloud-top radiative and evaporative cooling in a stratocumulus-topped boundary layer. *Quart. J. Roy. Meteor. Soc.*, **123**, 2187–2213.

Shin, H. H., S.-Y. Hong, and J. Dudhia, 2012: Impacts of the lowest model level height on the performance of planetary boundary layer parameterizations. *Monthly Weather Review*, **140**, 664–682.

Skamarock, W. C., J. B. Klemp, and J. Dudhia, 2001: Prototypes for the WRF (Weather Research and Forecasting) model., Fort Lauderdale, FL, Amer. Meteor. Soc. Preprints, Ninth Conf. on Mesoscale Processes.

Stevens, B., et al., 2005: Evaluation of large-eddy simulations via observations of nocturnal marine stratocumulus. *Monthly Weather Review*, **133**, 1443–1462.

Thompson, B. W., 1986: Small-scale katabatics and cold hollows. *Weather*, **41**, 146–153.

USDA, 2012: Usda, national agricultural statistics service, 2012 california cropland data layer. URL `http://www.nass.usda.gov/research/Cropland/metadata/metadata_ca12.htm`.

Wetzel, P. J., S. Argentini, and A. Boone, 1996: Role of land surface in controlling daytime cloud amount: Two case studies in the gcip-sw area. *J. of Geophysical Research*, **101**, 7359–7370.

Whiteman, C. D., 2000: *Mountain Meteorology*. Oxford University Press, 355 pp.

Whiteman, C. D., T. Haiden, B. Pospichal, S. Eisenbach, and R. Steinacker, 2004: Minimum temperatures, diurnal temperature ranges, and temperature inversions in limestone sinkholes of different sizes and shapes. *Journal of Applied Meteorology*, **43**, 1224–1236.

Whiteman, C. D., T. B. McKee, and J. C. Doran, 1996: Boundary layer evolution within a canyonland basin. part i: Mass, heat, and moisture budgets from observations. *Journal of Applied Meteorology*, **35**, 2145–2161.

Whiteman, C. D., S. Zhong, W. J. Shaw, J. M. Hubbe, X. Bian, and J. Mittelstadt, 2001: Cold pools in the columbia basin. *Weather and Forecasting*, **16**, 432–447.

Wyngaard, J. C. and R. A. Brost, 1984: Top-down and bottom-up diffusion of a scalar in the convective boundary layer. *Journal of the Atmospheric Sciences*, **41**, 102–112.

Zängl, G., 2005: Formation of extreme cold-air pools in elevated sinkholes: An idealized numerical process study. *Monthly Weather Review*, **133**, 925–941.

Zhong, S. C., D. Whiteman, X. Bian, W. J. Shaw, and J. M. Hubbe, 2001: Meteorological processes affecting the evolution of a wintertime cold air pool in the columbia basin. *Monthly Weather Review*, **129**, 2600–2613.